

**RAFAEL RICARDO AVILA NARANJO**

**ALTERNATIVES TO THE USE OF THE CROWBAR CIRCUIT IN DFIG BASED  
WIND TURBINES DURING BALANCED VOLTAGE DIPS**

**São Paulo**

**2014**

**RAFAEL RICARDO AVILA NARANJO**

**ALTERNATIVES TO THE USE OF THE CROWBAR CIRCUIT IN DFIG BASED  
WIND TURBINES DURING BALANCED VOLTAGE DIPS**

**Dissertação apresentada à Escola  
Politécnica da Universidade de São  
Paulo para obtenção do título de  
Mestre em Engenharia Elétrica**

**São Paulo  
2014**

**RAFAEL RICARDO AVILA NARANJO**

**ALTERNATIVES TO THE USE OF THE CROWBAR CIRCUIT IN DFIG BASED  
WIND TURBINES DURING BALANCED VOLTAGE DIPS**

**Dissertação apresentada à Escola  
Politécnica da Universidade de São  
Paulo para obtenção do título de  
Mestre em Engenharia Elétrica**

**Área de Concentração:  
Sistemas de potência**

**Orientador: Prof. Doutor  
Maurício Barbosa de Camargo  
Salles**

**São Paulo  
2014**

**Este exemplar foi revisado e corrigido em relação à versão original, sob responsabilidade única do autor e com a anuência de seu orientador.**

**São Paulo, de julho de 2014.**

**Assinatura do autor** \_\_\_\_\_

**Assinatura do orientador** \_\_\_\_\_

### **Catálogo-na-publicação**

**Avila Naranjo, Rafael Ricardo**

**Alternatives to the use of the crowbar circuit in DFIG based wind turbines during balanced voltage dips / R.R. Avila Naranjo. -- versão corr. -- São Paulo, 2014.**

**117 p.**

**Dissertação (Mestrado) - Escola Politécnica da Universidade de São Paulo. Departamento de Engenharia de Energia e Automação Elétricas.**

**1.Energia eólica 2.Turbinas 3.Circuitos elétricos I.Universidade de São Paulo. Escola Politécnica. Departamento de Engenharia de Energia e Automação Elétricas II.t.**

## **ACKNOWLEDGEMENTS**

To my advisor, Professor Mauricio Salles, by its constant support and friendship during all these years.

To the Coordenação de Aperfeiçoamento de Pessoal de Nivel Superior (CAPES), by its economic support during my masters.

To my family, since without their sacrifice this endeavor would not have been possible.

To Cristiana, for walking with me this way.

## **ABSTRACT**

Most of the modern wind turbines are based on doubly fed induction generators (DFIG), with a back to back power converter connecting the rotor to the network. It is known that voltage dips at the stator terminals can cause overcurrents in the rotor windings, which could threaten the converter integrity. In order to protect the converter, several strategies have been proposed in technical literature, requiring in some cases the converter deactivation, which disables the control that the converter has over the power transference between the generator and the system. This last is not a desirable behavior since it can put on risk the voltage stability of the electric system.

It is the aim of this dissertation to introduce and compare five of those protection strategies, through the computational simulation of their performance in case of balanced voltage dips. In order to achieve this, the electromagnetic dynamic model of the DFIG was theoretically developed, as well as the models of the strategies of interest. Subsequently, the computational model of the system was assembled in the software Matlab's Simulink to finally perform the desired simulations and its corresponding analysis.

**Keywords:** Wind power. Doubly Fed Induction Generator. Voltage dip.

## RESUMO

A maioria das turbinas eólicas modernas é baseada em geradores de indução duplamente alimentados (GIDE), com um back to back conversor de energia que liga o rotor para a rede. Sabe-se que as quedas de tensão nos terminais do estator podem causar sobrecorrentes nos enrolamentos do rotor, que podem ameaçar a integridade do conversor. A fim de proteger o conversor, várias estratégias têm sido propostas na literatura técnica, exigindo, em alguns casos, a desativação do conversor, o qual desativa o controlo do conversor, que possui ao longo da transferência de energia entre o gerador e o sistema. Este último não é um comportamento desejável, uma vez que pode colocar em risco a estabilidade de tensão do sistema elétrico. É o objetivo desta dissertação apresentar e comparar cinco dessas estratégias de proteção, através da simulação computacional de seu desempenho em caso de quedas de tensão equilibrada. A fim de alcançar este objetivo, o modelo dinâmico eletromagnética do DFIG teoricamente foi desenvolvido, bem como os modelos das estratégias de interesse. Subsequentemente, o modelo computacional do sistema foi montado no software Simulink do Matlab para finalmente executar as simulações desejadas e sua análise correspondente.

Palavras-chave: Energia eólica. Turbinas. Circuitos elétricos.

## LIST OF FIGURES

Figure 2.1 - One-phase DFIM steady-state equivalent circuit.....	15
Figure 2.2 - One-phase DFIM steady-state equivalent circuit with rotor parameters referred to the stator .....	17
Figure 2.3 - One phase steady-state equivalent circuit referred to the stator .....	18
Figure 2.4: Equivalent circuit arranged for the power relations identification.....	19
Figure 2.5 – Operation modes of the DFIM .....	22
Figure 2.6 – simplified schematic diagram of the DFIM.....	23
Figure 2.7 – Equivalent circuit in terms of the voltages, fluxes and currents .....	24
Figure 2.8 – Rotating vector representation in the plane .....	25
Figure 2.9 – Rotating vector $\alpha\beta$ components .....	25
Figure 2.10 – Rotating reference frame representation.....	27
Figure 2.11 - DFIM $\alpha\beta$ equivalent circuit .....	29
Figure 2.12 - DFIM dynamic model block representation .....	31
Figure 2.13 - Stator flux space vector trajectory .....	35
Figure 2.14 - $emf$ induced in the DFIM rotor in case of a full voltage dip.....	37
Figure 2.15 - Stator flux behavior during a partial voltage dip .....	39
Figure 2.16 - Stator flux space vector trajectory for a 50% voltage dip in time.....	41
Figure 2.17 - Stator flux space vector trajectory for a 50% voltage dip .....	41
Figure 2.18 - $emf$ induced in the rotor in case of a 50% voltage dip.....	42
Figure 3.1 - DFIG schematic diagram .....	43
Figure 3.2 - Two level voltage source converter.....	45
Figure 3.3 - Converter output circuit model .....	46
Figure 3.4 - 2L-VSC simulation model.....	47
Figure 3.5 - Converter output voltage harmonic content .....	49
Figure 3.6 - Control signal generation scheme.....	50
Figure 3.7 - Grid side converter equivalent circuit .....	51
Figure 3.8 - Grid side converter and filter simulation models.....	52
Figure 3.9 - DC-link equivalent circuit.....	53
Figure 3.10 - DC-link simulation model .....	54
Figure 3.11 - Complete DFIG simulation model .....	55
Figure 3.12 -Grid side converter equivalent circuit $dq$ model .....	56
Figure 3.13 - Rotating space vectors diagram.....	56

Figure 3.14 - Grid side converter control system.....	59
Figure 3.15 - PLL block diagram .....	60
Figure 3.16 -DFIG equivalent circuit model in the synchronous reference frame .....	62
Figure 3.17 - Rotor current reference calculation .....	63
Figure 3.18 - DFIG $dq$ equivalent circuit using the stator flux orientation .....	64
Figure 3.19 - Grid side converter control system.....	65
Figure 3.20 - Stator flux calculation principle.....	66
Figure 3.21 - PLL configuration for the stator flux angle calculation .....	66
Figure 3.22 - Grid voltage-orientation principle.....	67
Figure 3.23 - rotor position measurement .....	67
Figure 4.1 - Transient phenomena time scale .....	70
Figure 5.1 - DFIG equipped with crowbar.....	73
Figure 5.2 - Rotor equivalent circuit including the Crowbar system.....	73
Figure 5.3 - 90% three phase voltage dip for three crowbar resistances.....	74
Figure 5.4 - 90% three phase voltage dip for the optimum CB resistance value.....	76
Figure 5.5 - 90% three phase voltage dip for two crowbar resistances .....	77
Figure 5.6 - Layout of the SCI strategy.....	79
Figure 5.7 - 90% voltage dip with SCI strategy activated during 100ms.....	79
Figure 5.8 - Rotor voltage maximum value.....	81
Figure 5.9 - Rotor current references using DC strategy .....	84
Figure 5.10 - 90% three-phase voltage dip for three values of $Kd$ . .....	87
Figure 5.11 - DC+CB activation procedure in case of a 90% voltage dip:.....	89
Figure 5.12 - DC+Isr strategy layout.....	91
Figure 5.13 - Behavior of the DC+Isr and CB strategies in case of a 90% three-phase voltage dip:.....	92
Figure 6.1 - Stator natural flux behavior in case of a 50% voltage dip.....	94
Figure 6.2 - Rotor current behavior in case of a 50% three-phase voltage dip.....	95
Figure 6.3 - Stator reactive current contribution in case of a 50% voltage dip:.....	97
Figure 6.4 - Stator active current contribution in case of a 50% voltage dip.....	100
Figure 6.5 - Rotor voltage behavior in case of a 50% three-phase voltage dip .....	101
Figure 6.6 - RSC current behavior in case of a 50% three-phase voltage dip using a standard rated converter.....	103

Figure 6.7 - Stator reactive current contribution in case of a 50% three-phase voltage dip, using a standard rated converter.....	103
Figure 6.8 - - Stator natural flux behavior in case of a 90% three-phase voltage dip, using a standard rated converter.....	104
Figure 6.9 - Rotor current behavior in case of a 90% three-phase voltage dip, using a standard rated converter.....	105
Figure 6.10 - Stator reactive current contribution in case of a 90% three-phase voltage dip, using a standard rated converter.....	105

## CONTENTS

ACKNOWLEDGEMENTS.....	2
ABSTRACT .....	3
LIST OF FIGURES.....	4
CONTENTS.....	7
1. INTRODUCTION.....	10
2. DOUBLY FED INDUCTION GENERATOR.....	13
2.1. STEADY STATE OF THE DOUBLY FED INDUCTION MACHINE .....	13
2.1.1. Steady state equivalent circuit .....	15
2.1.2. Power definitions for the DFIM.....	19
2.1.3. Simplified Relations between the torque and active powers .....	21
2.1.4. Modes of operation of the DFIM .....	21
2.2. DYNAMIC MODEL OF THE DFIM .....	22
2.2.1. Space vector representation.....	24
2.2.2. $\alpha\beta$ model .....	27
2.3. BEHAVIOR OF THE DFIM IN CASE OF THREE-PHASE VOLTAGE DIPS	
32	
2.3.1. <i>emf</i> Induced in the rotor .....	32
2.3.2. Three-phase voltage dips .....	34
2.3.3. Total voltage dip with open-circuited rotor .....	34
2.3.4. Partial voltage dip with open-circuited rotor .....	37
3. BACK TO BACK POWER ELECTRONIC CONVERTER CONTROL .....	43
3.1. TWO LEVEL VOLTAGE SOURCE CONVERTER TOPOLOGY .....	44
3.2. 2L-VSC CONTROL SIGNALS GENERATION .....	48
3.2.1. Sinusoidal Pulse Width Modulation (PWM) .....	48
3.3. GRID AND ROTOR SIDE FILTERS.....	50
3.3.1. Grid side inductive filter .....	50

3.3.2.	Rotor side inductive <i>dvd</i> t filter .....	52
3.4.	DC-LINK.....	53
3.5.	BACK TO BACK CONVERTER COMPLETE MODEL.....	54
3.6.	GSC CONTROL SYSTEM .....	55
3.6.1.	Grid side system <i>dq</i> model.....	55
3.6.2.	Grid voltage orientated vector control.....	57
3.7.	RSC CONTROL SYSTEM .....	60
3.7.1.	DFIM dynamic <i>dq</i> model .....	61
3.7.2.	Alignment of the rotating reference frame.....	61
3.7.3.	Stator flux orientated vector control .....	63
4.	METHODOLOGY AND ASSUMPTIONS .....	68
4.1.	SIMPOWERSYSTEMS SOLUTION METHODOLOGY.....	68
4.2.	SIMPOWERSYSTEMS SOLUTION METHODS .....	69
4.3.	ASSUMPTIONS .....	70
5.	RSC PROTECTION STRATEGIES .....	72
5.1.	CROWBAR CIRCUIT (CB).....	72
5.2.	FEEDBACK OF THE STATOR CURRENTS AS RSC REFERENCES (SCI) 77	
5.3.	DEMAGNETIZING CURRENT INJECTION (DC) .....	82
5.4.	DEMAGNETIZING CURRENT VARIANTS .....	86
5.4.1.	Crowbar & demagnetizing current injection (DC+CB).....	86
5.4.2.	Increase of the stator resistance & demagnetizing current injection (DC+I <sub>sr</sub> ) .....	90
6.	STRATEGIES COMPARISON .....	94
6.1.	INTERMEDIATE BALANCED VOLTAGE DIP .....	94
6.1.1.	Grid-codes compliance .....	97
6.1.2.	Active power behavior .....	99
6.1.3.	Rotor voltage behavior.....	101

6.1.4. Influence of using standard ratings for the converter .....	102
6.2. DEEP BALANCED VOLTAGE DIP .....	104
7. CONCLUSIONS AND FURTHER WORK .....	107
7.1 FURTHER WORK.....	108
BIBLIOGRAPHY.....	110
APENDIX A - 2MW DFIG technical data .....	112
APENDIX B - Publications.....	113

## 1. INTRODUCTION

In the last decades, a substantial increment of the wind power penetration in the electric power systems has occurred. By the end of 2013, the global cumulative wind power capacity was approximately 319.6GW, expecting it to achieve a total of 678GW by 2020(GLOBALDATA, 2014). In Brazil, the wind power installed capacity by the time that this document was written was approximately 4,5GW, expecting it to rise up to 11.5GW by 2020(MINISTÉRIO DE MINAS E ENERGIA; EMPRESA DE PESQUISA ENERGÉTICA, 2011).

Among the energy conversion technologies available for wind turbines, the doubly fed induction generator (DFIG) stands out for its ability to work at different wind speeds with reduced power electronics costs, becoming in the last few years one of the most commonly used solutions by wind turbines manufacturers (GAUTAM et al., 2009);(BLAABJERG; CHEN, 2006).

The DFIG consists of a wound rotor induction machine with its stator directly connected to the grid, and its rotor connected to the same grid through a back to back converter. This converter is in charge of, among other things, the control of the stator voltage amplitude and frequency (when connected to a system with small short circuit level) and the control of the active and reactive power transference with the grid (when connected to a “strong” system). This last is what allows the generator to work at different wind speeds.[(NASAR; BOLDEA, 1992)](CHEN, 2008).

Electric grid disturbances can cause voltage dips in several nodes of a power system. Due to the high sensitivity to variations in the network voltage of the DFIG, the introduction of protection strategies against the injurious effects of this phenomenon is mandatory(ABAD et al., 2011).

Several protection strategies have been suggested in technical literature (XIANG et al., 2006)(LIMA et al., 2010)(ESANDI et al., 2009)(LÓPEZ et al., 2009). Among them, the crowbar circuit strategy stands out by its high efficacy protecting the converter in case of abrupt voltage variations, what justifies its extensive use in DFIG based generators. The activation of this protection strategy forces the disconnection of the converter for a short period of time, losing in that way the control over the amount of active and reactive power delivered to the system, and leaving the rotor speed control to be determined by the pitch angle control system.

While the aforementioned control loss was not concerning when the wind power penetration was incipient, with the increasing participation of wind-based generation systems in the worldwide energy matrices such uncontrolled behavior is considered to be highly undesirable. This last is justified by the injurious consequences that the non-injection of reactive power has over the voltage stability of the grid during voltage dips. In order to regulate the maximum amount of time that the generator can remain without contributing to the voltage recovery, gridcodes establishing the amount of reactive current that the generator must inject depending on the voltage dip depth have been introduced in some European countries(SOURKOUNIS; TOUROU, 2013). By the time this document was finished, it was not found by the author any official report addressing this subject for the Brazilian context.

Thus, it is of our interest in this research project the study of alternatives to the use of the crowbar strategy, assessing their potential for the reduction of the non-contribution time while ensuring the safety of the converter.

In this dissertation is presented a comparative study of the performance of five protection strategies for the doubly fed induction generator, in case of balanced voltage dips. Initially, a general presentation of the generator was done in chapter 2, including its topology, operation modes and its steady-state and dynamic models.

In chapter 3, the control systems commanding the operation of the generator were introduced, as well as the electronic devices necessary for its implementation in a real generation system. In this chapter were also introduced dynamic models of the aforementioned systems and devices, which were projected to be compatible with the dynamic model of the DFIG, having in this way all the tools necessary for assembling the complete electromagnetic model of the generation system, which is appropriate for the study of transient phenomena as the already mentioned balanced voltage dips.

The computational tool selected for the implementation of the model is presented in chapter 4, jointly with several simplifying assumptions applied during the modeling process that allowed us to decouple the electromechanic behavior of the machine (in charge of the rotor speed variation during the voltage dip) from the potentially injurious electromagnetic phenomena that appears during voltage dips.

A complete introduction of each one of the selected protection strategies is performed in chapter 5, making use of the implemented model to simulate diverse voltage dips, in order to illustrate their operation in detail. In chapter 6 the strategies

are exposed to voltage dips with different magnitudes, evaluating not only its effectiveness protecting the converter, but also the compliance of the current gridcodes requirements.

## 2. DOUBLY FED INDUCTION GENERATOR

As mentioned in the introduction chapter, the majority of the currently installed wind turbines are equipped with Doubly Fed Induction Generators (DFIGs) for the electric energy generation process. For this reason, and having in mind that one of the main goals of this research is the development of a computational model for this energy conversion system, the study of the DFIG mathematical model is indispensable. This electrical machine can be addressed as a doubly fed induction machine (DFIM) operating as a generator, with the purpose of delivering energy to the network. In section 2.1 will be introduced the steady state model of the DFIM, as a first approach to the dynamic model of the machine. The later will be presented in section 2.2, providing the necessary tools for the implementation in the chosen simulation software. Finally, in section 2.3 the electromagnetic behavior of the DFIM in case of three-phase voltage dips is addressed.

### 2.1. STEADY STATE OF THE DOUBLY FED INDUCTION MACHINE

As in other electrical machines, the two main components of the DFIM are the stator and the rotor. A set of three-phase windings is attached to each one of them, being independently supplied and allowing a bidirectional flux of energy. The rotor windings are displaced from each other by 120 electrical degrees in space around the surface of the rotor, being supplied through the brushed and the slip ring. The stator windings are also displaced from each other by 120 electrical degrees in space, being for this case distributed around the inner circumference of the stator. When the stator windings are supplied by a three-phase balanced voltage a rotating sinusoidal stator flux appears. The rotation speed of this flux depends on the frequency of the applied voltage  $f_s$  and the number of pair poles of the stator  $p$  as shown in eq.(2.1):

$$n_s = \frac{60f_s}{p} \text{ (rpm)} \quad (2.1)$$

This rotational flux induces in the rotor windings conductors an  $emf$  established by faraday's law:

$$e_{ind} = (v \times B) \cdot L \quad (2.2)$$

Where,

$e_{ind}$  = emf induced in one of the rotor conductors

$v$  = relative speed between the rotor and the rotating flux

$B$  = stator flux density vector

$L$  = length of the conductor

If the rotor windings are connected to a closed circuit, the joint action between this induced *emf* and the voltage imposed at the windings terminals will cause the circulation of electric currents. According to the Laplace's law, the circulation of an electric current in the presence of a magnetic field generates an induced force on the current conductors:

$$F = i \cdot (L \times B) \quad (2.3)$$

Where,

$F$  = induced force

$i$  = current circulating through the rotor conductor

$B$  = stator flux density vector

$L$  = length of the conductor

In the technical literature, it is defined as slip  $s$  the relation between the stator flux rotation speed (known also as synchronous speed)  $n_s$  and the rotor rotation speed  $n_m$ :

$$s = \frac{n_s - n_m}{n_s} \quad (2.4)$$

As presented in (FRAILE MORA, 2006), the frequency of the induced voltages and currents in the rotor are defined by the next relation:

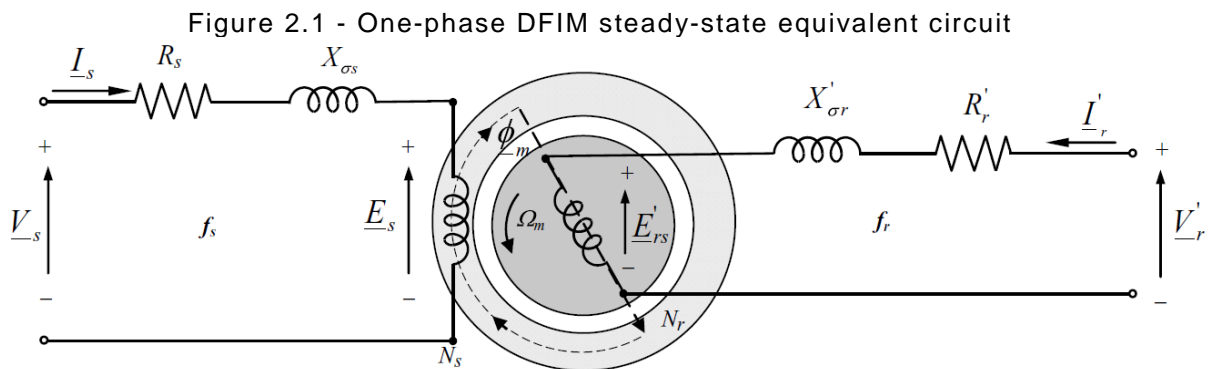
$$f_r = s f_s \quad (2.5)$$

In the case of non rotation of the rotor, that is  $n_m = 0$  and consequently  $s = 1$ , we have that the frequencies of the stator and rotor currents and voltages have the same value.

$$f_r = f_s \quad (2.6)$$

### 2.1.1. Steady state equivalent circuit

Assuming that both the stator and the rotor are supplied by constant and balanced three-phase voltage sources, and that both of them are connected in the star configuration, the steady state of the complete system can be represented by a one-phase equivalent phasorial circuit as the one presented in Figure 2.1. As can be observed, this circuit only differs from the widely known transformer equivalent circuit due to the difference between rotor and stator frequencies introduced by the rotor movement (see eq.(2.5)).



Source: (ABAD et al., 2011)

Where:

$\underline{V}_s$  = supplied stator voltage

$\underline{V}'_r$  = supplied rotor voltage

$\underline{I}_s$  = induced stator current

$\underline{I}'_r$  = induced rotor current

$\underline{E}_s$  = induced emf in the stator

$\underline{E}'_{rs}$  = induced emf in the rotor

$R_s$  = stator resistance

$R'_r$  = rotor resistance

$X_{\sigma s} = j\omega_s L_{\sigma s}$  = stator leakage impedance

$X'_{\sigma r} = j\omega_s L_{\sigma s}$  = rotor leakage impedance

$N_s$  = stator winding's number of turns per phase

$N_r$  = rotor winding's number of turns per phase

Applying Thevenin's theorem to the rotor and stator independently we have:

$$\underline{V}_s - \underline{E}_s = (R_s + X_{\sigma s}) \underline{I}_s \quad \text{at } f_s \quad (2.7)$$

$$\underline{V}_r' - \underline{E}_{rs}' = (R_r' + X_{\sigma r}') \underline{I}_r' \quad \text{at } f_r \quad (2.8)$$

The induced *emf* is associated to the stator and rotor can be defined as (LÓPEZ et al., 2009) as:

$$\underline{E}_s = \sqrt{2}\pi K_s N_s f_s \Phi_m \quad (2.9)$$

$$\underline{E}_{rs}' = \sqrt{2}\pi K_r N_r f_r \Phi_m \quad (2.10)$$

Where:

$K_s$  = Stator winding factor. Slightly smaller than 1

$K_r$  = Rotor winding factor. Slightly smaller than 1

$\Phi_m$  = Magnetic flux

Due to the existing relation between stator and rotor frequencies (eq.(2.6)), the relation between the stator and rotor induced *emfs* can be presented as:

$$\frac{\underline{E}_{rs}'}{\underline{E}_s} = s \frac{K_r N_r}{K_s N_s} \quad (2.11)$$

According to (ABAD et al., 2011), for wind generation applications, the machines are designed make both  $K_r$  and  $K_s$  very proximate to 1. Thus, we have that the relation only depends on the machine turns ratio  $u = \frac{N_s}{N_r}$  and the slip:

$$\frac{\underline{E}_{rs}'}{\underline{E}_s} = \frac{s}{u} \quad (2.12)$$

In order to obtain a useful version of the equivalent circuit, it is necessary to go from a circuit with two voltage levels and two frequencies, to an equivalent model with only one voltage level and a unique frequency. The first step to achieve this is to refer the impedances, voltages and currents of the rotor to the stator, as done when modeling the electric transformer:

$$R_r = R_r' u^2 \quad (2.13)$$

$$L_{\sigma r} = L_{\sigma r}' u^2 \quad (2.14)$$

$$\underline{I}_r = \frac{\underline{I}_r'}{u} \quad (2.15)$$

$$\underline{V}_r = \underline{V}_r' u \quad (2.16)$$

$$\underline{E}_{rs} = \underline{E}_{rs}' u \quad (2.17)$$

Where,

$R_r$  = Rotor resistance referred to the stator

$L_{\sigma r}$  = Rotor leakage inductance referred to the stator

$\underline{I}_r$  = Rotor current referred to the stator

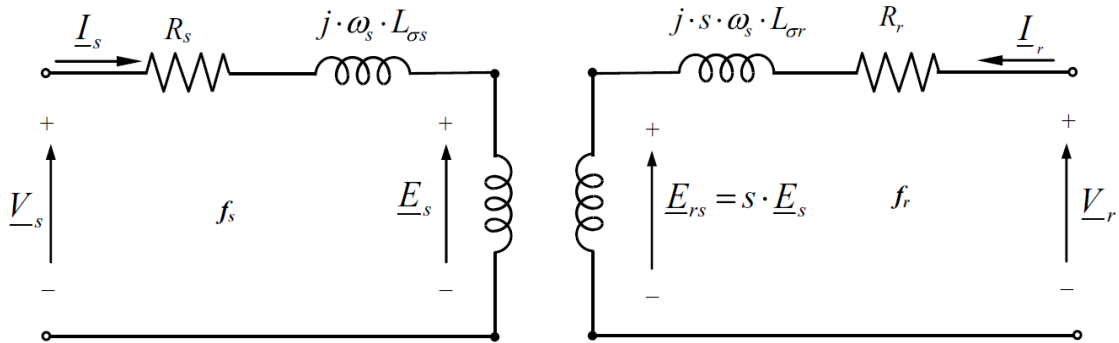
$\underline{V}_r$  = Rotor voltage referred to the stator

$\underline{E}_{rs}$  = *emf* induced in the rotor referred to stator

This procedure results in the circuit presented in Figure 2.2. The new rotor voltage equation is:

$$\underline{V}_r - \underline{E}_{rs} = (R_r + j\omega_s L_{\sigma r}) \underline{I}_r \text{ at } f_r \quad (2.18)$$

Figure 2.2 - One-phase DFIM steady-state equivalent circuit with rotor parameters referred to the stator



Source: (ABAD et al., 2011)

By substituting equations.(2.12) in (2.18) we obtain:

$$\underline{V}_r - s\underline{E}_s = (R_r + j\omega_s L_{\sigma r}) \underline{I}_r \text{ at } f_r \quad (2.19)$$

As explained in (FRAILE MORA, 2006), dividing eq.(2.19) by  $s$  is mathematically equivalent to change the rotor circuit frequency from  $f_r$  to  $f_s$ .

$$\frac{\underline{V}_r}{s} - \underline{E}_s = \left(\frac{R_r}{s} + j\omega_s L_{\sigma r}\right) \underline{I}_r \text{ at } f_s \quad (2.20)$$

From this equation is possible to see that the rotor induced *emf* has the same value than the stator induced *emf*, which represent an unique voltage level for both the stator and rotor. In addition, the stator frequency is imposed in the rotor, achieving in this way the requirements for the construction of an equivalent circuit totally referred to the stator. Such circuit is described by the combination of equations (2.17) and (2.20).

$$\underline{V}_s - \frac{\underline{V}_r}{s} - (R_s + j\omega_s L_{\sigma s})\underline{I}_s + \left(\frac{R_r}{s} + j\omega_s L_{\sigma r}\right)\underline{I}_r = 0 \text{ at } f_s \quad (2.21)$$

Where,

$L_{\sigma s}$  = stator leakage inductance

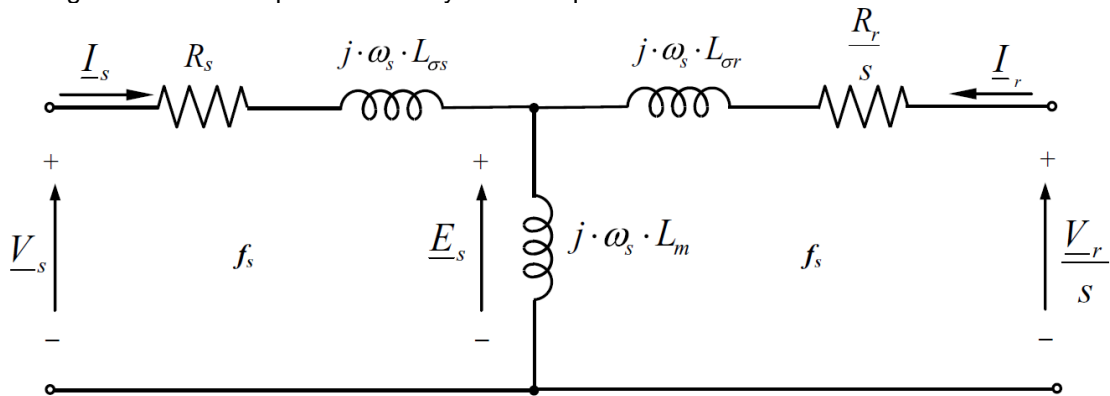
In Figure 2.3 is present the final form of the DFIM equivalent circuit governed by eq.(2.21), where the stator induced *emf* is equal to:

$$\underline{E}_s = j\omega_s L_m (\underline{I}_s + \underline{I}_r) \text{ at } f_s \quad (2.22)$$

Where,

$L_m$  = magnetizing inductance of the machine.

Figure 2.3 - One phase steady-state equivalent circuit referred to the stator



Source: (ABAD et al., 2011)

This simplified circuit makes evident that the stator and rotor fluxes can be defined from the stator and rotor currents as:

$$\underline{\Psi}_s = L_m (\underline{I}_s + \underline{I}_r) + L_{\sigma s} \underline{I}_s = L_s \underline{I}_s + L_m \underline{I}_r \quad (2.23)$$

$$\underline{\Psi}_r = L_m (\underline{I}_s + \underline{I}_r) + L_{\sigma r} \underline{I}_r = L_s \underline{I}_s + L_m \underline{I}_r \quad (2.24)$$

Where,

$L_s = L_m + L_{\sigma s}$  = stator inductance

$L_r = L_m + L_{\sigma r}$  = rotor inductance

Finally, the combination of equations (2.17) and (2.20) with equations (2.23) and (2.24) results in equations relating the stator and rotor voltages with the corresponding fluxes:

$$\underline{V}_s - R_s \underline{I}_s = j\omega_s \underline{\Psi}_s \quad (2.25)$$

$$\underline{V}_r - R_r \underline{I}_r = js\omega_s \underline{\Psi}_r \quad (2.26)$$

### 2.1.2. Power definitions for the DFIM

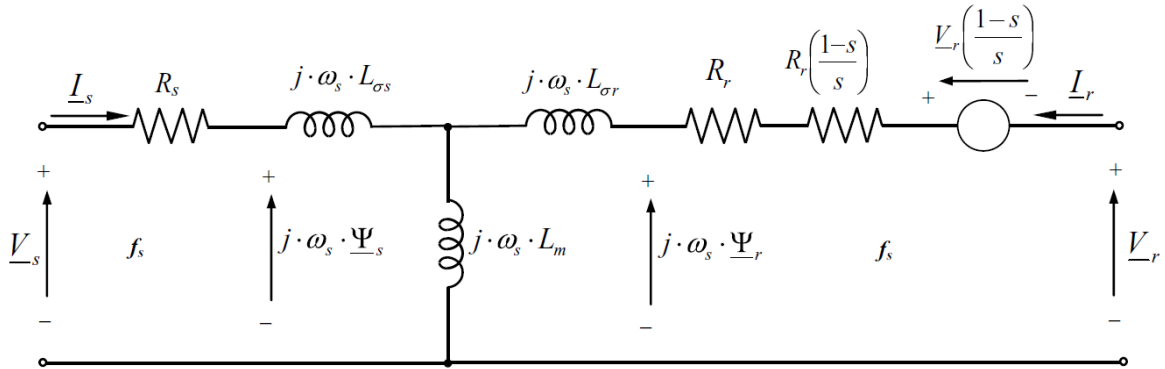
In order to simplify the deduction of the torque, active power and reactive power definitions for the machine, the equivalent circuit presented in Figure 2.3 has to be slightly modified, decomposing the terms  $\frac{R_r}{s}$  and  $\frac{V_r}{s}$  as:

$$\frac{R_r}{s} \rightarrow R_r + R_r \left( \frac{1-s}{s} \right) \quad (2.27)$$

$$\frac{V_r}{s} \rightarrow \underline{V}_r + \underline{V}_r \left( \frac{1-s}{s} \right) \quad (2.28)$$

Which leads to the equivalent circuit presented in Figure 2.4.

Figure 2.4: Equivalent circuit arranged for the power relations identification



Source: (ABAD et al., 2011)

This new structure allows a fast identification of the circuit elements related with the active power losses and the ones are related with the generation of mechanic power. Thus, it is possible to define the power losses in the stator and rotor as:

$$P_{cu-s} = 3R_s |I_s|^2 \quad (2.29)$$

$$P_{cu-r} = 3R_r |I_r|^2 \quad (2.30)$$

Having defined these quantities, it is possible now to formulate the power balance of the machine:

$$P_s + P_r = P_{cu-s} + P_{cu-r} + P_{mec} \quad (2.31)$$

Where:

$P_s$  = stator active power (W)

$P_r$  = rotor active power (W)

$P_{mec}$  = mechanical power (W)

And:

$$P_s = 3\text{Re}\{\underline{V}_s \cdot \underline{I}_s^*\} = P_{cu-s} + 3\text{Re}\{j\omega_s L_m \underline{I}_r \cdot \underline{I}_s^*\} \quad (2.32)$$

$$P_r = 3\text{Re}\{\underline{V}_r \cdot \underline{I}_r^*\} = P_{cu-r} + 3\text{Re}\{js\omega_s L_m \underline{I}_s \cdot \underline{I}_r^*\} \quad (2.33)$$

According to equations (2.29) and (2.30), the electric power losses always have a positive value. Consequently, it is established that the stator and rotor powers only have a positive value when the machine is receiving power through the stator and rotor respectively. In addition, for the mechanical power is assumed the motor convention, which indicates that the mechanical power assumes a positive value only when power is being delivered through the shaft of the machine, that is in the motor mode of operation.

Equation (2.31) allows the calculation of the mechanical power delivered or consumed by the DFIM for any point of operation, provided that the value of the stator and rotor voltages and currents is known as well as the stator and rotor resistance value. After a minor mathematical manipulation of eq.(2.31), (ABAD et al., 2011) delivers a simplified expression to calculate the mechanical power that is independent of the stator and rotor voltages and resistances:

$$P_{mec} = 3\omega_m L_m \cdot \text{Im}\{\underline{I}_r^* \cdot \underline{I}_s\} \quad (2.34)$$

In (CHAPMAN, 2005) is demonstrated the relation between the mechanical power and the electromagnetic torque in the shaft of the machine:

$$P_{mec} = T_{em} \Omega_{em} = T_{em} \frac{\omega_m}{p} \quad (2.35)$$

Where,

$T_{em}$  = electromagnetic torque in the shaft of the machine

$\Omega_{em}$  = mechanical rotational speed at the rotor (rad/s)

The combination of equations (2.34) and (2.35) results in:

$$T_{em} = 3pL_m \cdot \text{Im}\{\underline{I}_r^* \cdot \underline{I}_s\} \quad (2.36)$$

If the stator and rotor fluxes are used for the torque calculation, the following expression is obtained:

$$T_{em} = \frac{3L_m}{\sigma L_r L_s} p \cdot \text{Im}\{\underline{\Psi}_r^* \cdot \underline{\Psi}_s\} \quad (2.37)$$

### 2.1.3. Simplified Relations between the torque and active powers

A straightforward relation between the stator and rotor active powers can be obtained if the stator and rotor power losses are neglected from equations (2.32) and (2.33):

$$P_r \approx -sP_s \quad (2.38)$$

Introducing this relation in eq.(2.31) we have:

$$P_{mec} \approx P_s - sP_s = (1 - s)P_s = \frac{\omega_m}{\omega_s} P_s \quad (2.39)$$

The combination of equations (2.39) and (2.25) leads to:

$$P_s \approx T_{em} \frac{\omega_s}{p} \quad (2.40)$$

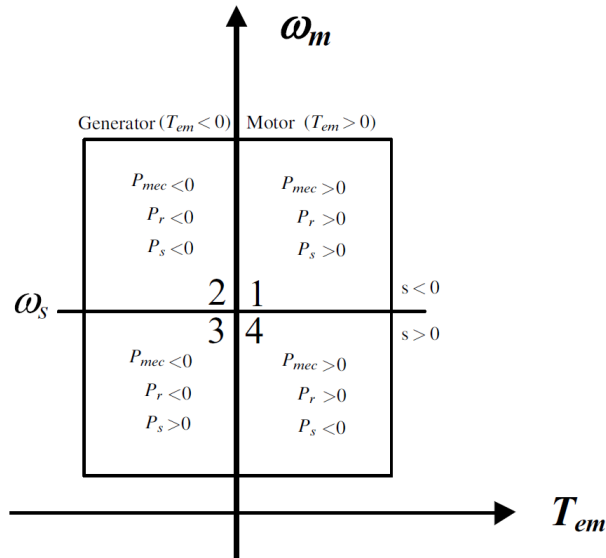
Consequently, the relation between the rotor active power and the torque is:

$$P_r \approx T_{em} \frac{\omega_r}{p} \quad (2.41)$$

### 2.1.4. Modes of operation of the DFIM

It is possible to evince from equations (2.38) - (2.41) the outstanding flexibility of the DFIM in terms of its operation conditions. For a considerable range of rotor rotation speed ( $-0.3 \leq s \leq 0.3$ ), this machine is able to operate in hypersynchronism and subsynchronism both as a generator and as a motor, something far from possible for the more rigid induction generator. Figure 2.5 presents graphically the active power direction requirements for the four modes of operation of the machine. It is worth it to mention that the movement among these operation modes is only possible due to the strict control over the rotor current, performed by RSC control structure, which is presented in Chapter 3.

Figure 2.5 – Operation modes of the DFIM



## 2.2. DYNAMIC MODEL OF THE DFIM

As its name suggests, DFIM's steady state model is restricted to steady state conditions, requiring the development of a more general model of the machine, in order to study its behavior during transitory states. In light of this, it is presented the dynamic model of the DFIM, a powerful tool that gives theoretical support to the computational model of the machine assembled in the simulation tool SimPowerSystems.

As established in (BOLDEA, 2005) and reaffirmed in Section 2.1, the DFIM can be modeled in a simplified way as being composed by two sets of three concentrated windings, located in the stator and rotor of the machine as depicted in Figure 2.6. Assuming that the three windings located in the stator are identical, and that there is a resistance  $R_s$  associated to each one of them, the voltage at its terminals can be defined as:

$$v_{as}(t) = R_s i_{as}(t) + \frac{d\Psi_{as}(t)}{dt} \quad (2.42)$$

$$v_{bs}(t) = R_s i_{bs}(t) + \frac{d\Psi_{bs}(t)}{dt} \quad (2.43)$$

$$v_{cs}(t) = R_s i_{cs}(t) + \frac{d\Psi_{cs}(t)}{dt} \quad (2.44)$$

Where  $v_{as}(t)$ ,  $v_{bs}(t)$  and  $v_{cs}(t)$  are the stator phase voltage for phases a, b and c respectively,  $i_{as}(t)$ ,  $i_{bs}(t)$  and  $i_{cs}(t)$  are the stator phase currents and  $\Psi_{as}(t)$ ,  $\Psi_{bs}(t)$  and  $\Psi_{cs}(t)$  are the stator fluxes.

A similar set of equations is obtained for the rotor:

$$v_{ar}(t) = R_r i_{ar}(t) + \frac{d\Psi_{ar}(t)}{dt} \quad (2.45)$$

$$v_{br}(t) = R_r i_{br}(t) + \frac{d\Psi_{br}(t)}{dt} \quad (2.46)$$

$$v_{cr}(t) = R_r i_{cr}(t) + \frac{d\Psi_{cr}(t)}{dt} \quad (2.47)$$

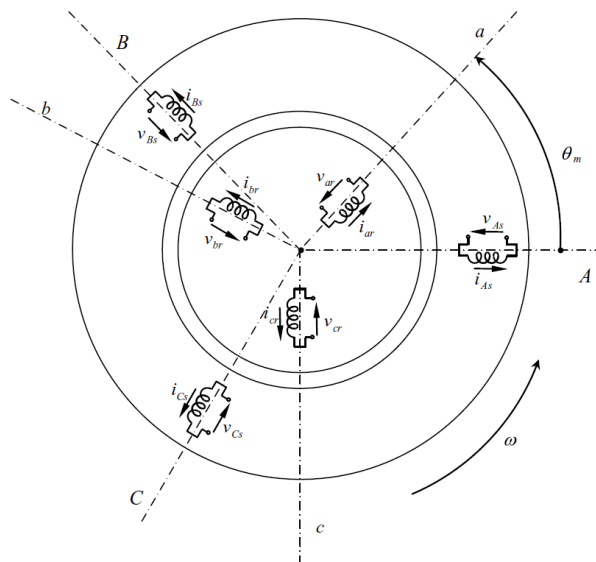
Where  $v_{ar}(t)$ ,  $v_{br}(t)$  and  $v_{cr}(t)$  are the rotor phase voltage for phases a, b and c respectively,  $i_{ar}(t)$ ,  $i_{br}(t)$  and  $i_{cr}(t)$  are the rotor phase currents and  $\Psi_{ar}(t)$ ,  $\Psi_{br}(t)$  and  $\Psi_{cr}(t)$  are the rotor fluxes.

The relation between the stator and rotor frequencies, presented in eq.(2.5), remains valid for this model. From the combination of equations (2.4) and (2.5), it is obtained the relation between the stator angular frequency and the rotor angular frequency:

$$\omega_r + \omega_m = \omega_s \quad (2.48)$$

Where  $\omega_m$  is the electrical angular frequency of the machine.

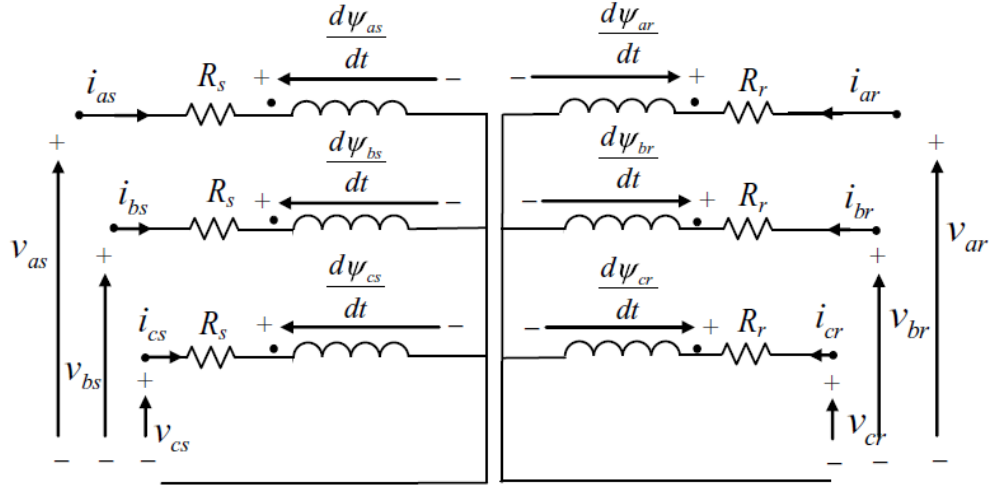
Figure 2.6 – simplified schematic diagram of the DFIM



Source: (ABAD et al., 2011)

Assuming a star connection of the stator and rotor windings, an equivalent circuit can be derived from equations (2.42) - (2.47), which is presented in Figure 2.7.

Figure 2.7 – Equivalent circuit in terms of the voltages, fluxes and currents



Source: (ABAD et al., 2011)

### 2.2.1. Space vector representation

It is convenient at this point the introduction of the space vector representation, a tool that significantly simplifies the modeling process of the machine, allowing the transition from a three-phase representation of the DFIM (2.43) - (2.47), to a two-phase model of the machine.

A three-phase sinusoidal set of signals is mathematically described by the equations:

$$x_a = \hat{X} \cos(\omega t + \phi) \quad (2.49)$$

$$x_b = \hat{X} \cos(\omega t + \phi - 2\pi/3) \quad (2.50)$$

$$x_c = \hat{X} \cos(\omega t + \phi + 2\pi/3) \quad (2.51)$$

With a constant angular frequency  $\omega$ , amplitude  $\hat{X}$  and phase shift  $\phi$ . This set of equations can be represented in a Cartesian plane as a rotating vector  $\vec{x}$ , with amplitude  $\hat{X}$  and a rotation speed  $\omega t$  as shown in Figure 2.8. It can be easily proven that the projection of  $\vec{x}$  on each one of the  $120^\circ$  spatially shifted axis  $\vec{a}$ ,  $\vec{b}$  and  $\vec{c}$ , returns the instantaneous magnitudes  $x_a$ ,  $x_b$  and  $x_c$  respectively.

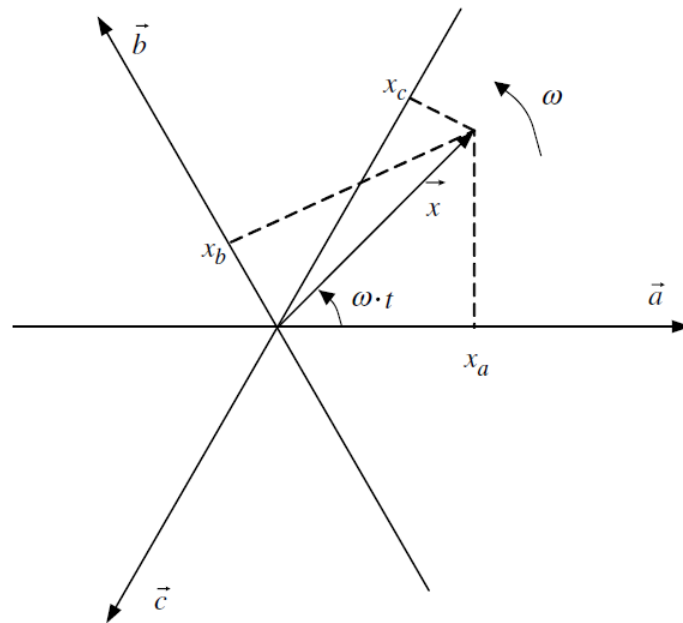
In this way, the mathematical expression that describes vector  $\vec{x}$  is:

$$\vec{x} = \hat{X} e^{j(\omega t + \phi)} = \frac{2}{3} (x_a + ax_b + a^2 x_c) \quad (2.52)$$

Where,

$$a = e^{j(2\pi/3)} \quad (2.53)$$

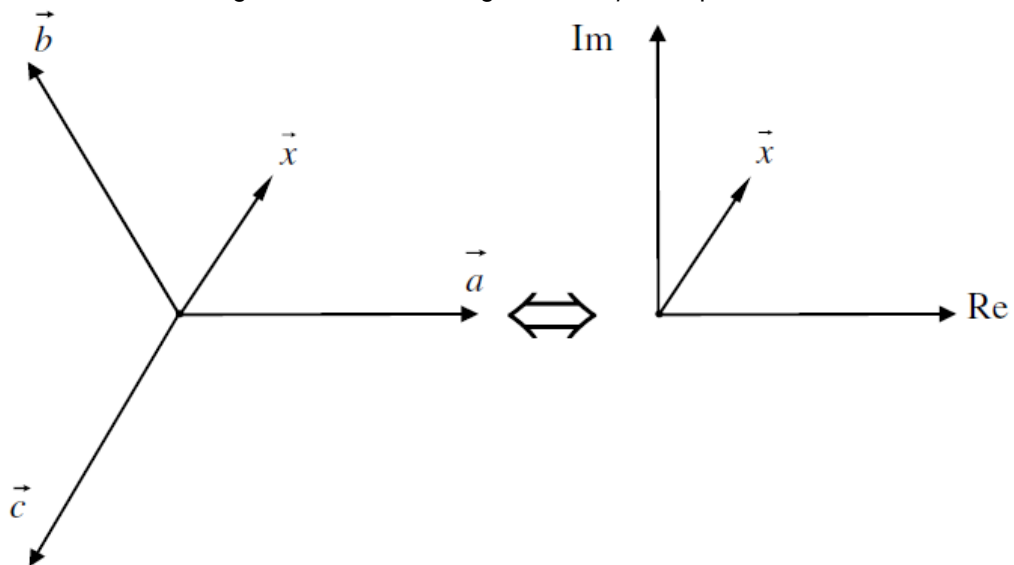
Figure 2.8 – Rotating vector representation in the plane



Source: (ABAD et al., 2011)

As shown in Figure 2.9, this rotating vector  $\vec{x}$  can be completely described by its projection on the real and imaginary axis of a complex plane. This evidently reduces the amount of components necessary to represent a balanced three-phase system, going from three to two. Associating the real axis with letter  $\alpha$ , and the imaginary axis with letter  $\beta$ , vector  $\vec{x}$  becomes:

$$\vec{x} = x_\alpha + jx_\beta \quad (2.54)$$

Figure 2.9 – Rotating vector  $\alpha\beta$  components

The relation between the  $\alpha\beta$  components ( $x_\alpha$  and  $x_\beta$ ) and the  $abc$  components ( $x_a$ ,  $x_b$  and  $x_c$ ) was first introduced by (SCHULZ; CLARKE, 1951):

$$\begin{bmatrix} x_\alpha \\ x_\beta \end{bmatrix} = \frac{2}{3} \begin{bmatrix} 1 & -\frac{1}{2} & -\frac{1}{2} \\ 0 & \frac{\sqrt{3}}{2} & -\frac{\sqrt{3}}{2} \end{bmatrix} \cdot \begin{bmatrix} x_a \\ x_b \\ x_c \end{bmatrix} \quad (2.55)$$

Resulting in the matrix  $T$  known as the Clarke direct transformation:

$$T = \frac{2}{3} \begin{bmatrix} 1 & -\frac{1}{2} & -\frac{1}{2} \\ 0 & \frac{\sqrt{3}}{2} & -\frac{\sqrt{3}}{2} \end{bmatrix} \quad (2.56)$$

Thus, for a balance three-phase system, the final form of eq.(2.54) is:

$$\vec{x} = x_\alpha + jx_\beta = \hat{X} \cos(\omega t + \phi) + j\hat{X} \sin(\omega t + \phi) \quad (2.57)$$

It was assumed up to this point that reference frame remains stationary during the rotation of vector  $\vec{x}$ . As will be seen in Chapter 3, establishing a rotating reference frame considerably simplifies the rotor side converter control system. Thus, it is necessary to find the relation between the  $\alpha\beta$  components of  $\vec{x}$  and the projection of  $\vec{x}$  on the axis of the rotating reference frame. In Figure 2.10 is represented a reference frame rotating at synchronous speed  $\omega_s$ , known as the synchronous reference frame  $dq$ . It can be noticed that, as in the case of the  $\alpha\beta$  reference frame, the axis of the synchronous reference frame are 90 phase shifted. These axis are commonly known as direct and quadrature axis. The relation between the projection of  $\vec{x}$  on the  $\alpha\beta$  axis and its projection on the  $dq$  axis can be addressed through the next operation:

$$\vec{x}^a = \begin{bmatrix} x_d \\ x_q \end{bmatrix} = \begin{bmatrix} \cos \theta_s & -\sin \theta_s \\ \sin \theta_s & \cos \theta_s \end{bmatrix} \cdot \begin{bmatrix} x_\alpha \\ x_\beta \end{bmatrix} \quad (2.58)$$

Where,

$\theta_s$ = electric angular position of direct axis with respect to  $\alpha$  axis.

$$\theta_s = \int \omega_s dt = \omega_s \cdot t \quad (2.59)$$

It is important to notice from eq.(2.58) the introduction of superscripts to signalize the reference frame to which the rotating vector is referred, establishing the superscript  $a$  for the synchronous reference frame and the superscript  $s$  for the stationary reference frame.

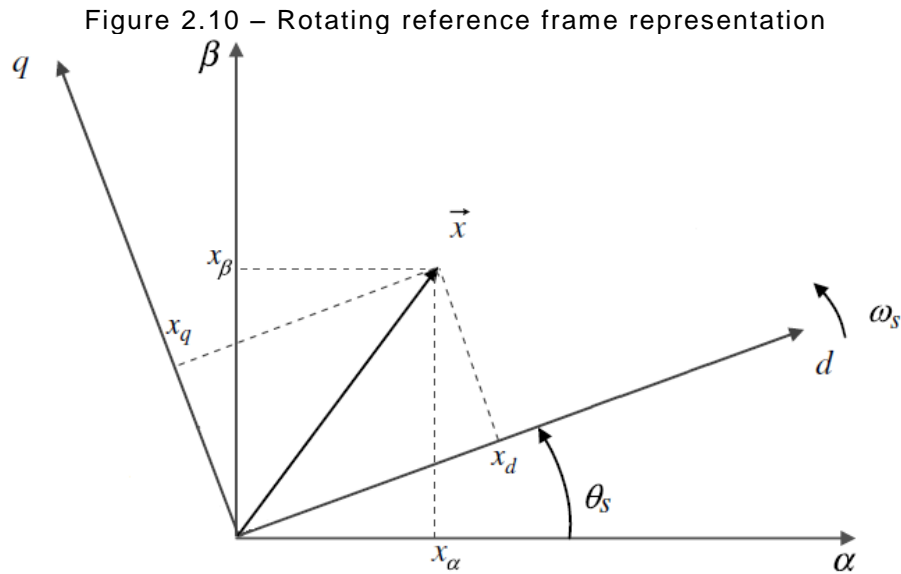
Finally, eq.(2.58) can be rewritten in terms of Euler's formula as:

$$\vec{x}^a = e^{-j\theta_s} \vec{x}^s \quad (2.60)$$

With its inverse form:

$$\vec{x}^s = e^{j\theta_s} \vec{x}^a \quad (2.61)$$

The results obtained in this section can be applied to any three-phase quantity related with the DFIM. This, as will be seen in the next sections, simplifies considerably the modeling procedure of the machine as well as the control of the back to back converter.



Source: (ABAD et al., 2011)

### 2.2.2. $\alpha\beta$ model

Equations (2.42) - (2.47) describe the behavior of the stator and rotor voltages, in terms of the stator and rotor currents and fluxes. Making use of the space vector representation, they will be condensed in two vectors, obtaining from them the model of the machine in the stationary reference frame ( $\alpha\beta$  model).

Applying eq. (2.52) to equations (2.42) - (2.44) and to equations (2.45) - (2.47), the stator voltage and rotor voltage vector equations are obtained:

$$\vec{v}_s^s = R_s \vec{i}_s^s + \frac{d\vec{\Psi}_s^s}{dt} \quad (2.62)$$

$$\vec{v}_r^r = R_r \vec{i}_r^r + \frac{d\vec{\Psi}_r^r}{dt} \quad (2.63)$$

where  $\vec{v}_s^s$  is the stator voltage space vector,  $\vec{i}_s^s$  is the stator current space vector and  $\vec{\Psi}_s^s$  is the stator flux space vector. These three vectors rotate at synchronous speed ( $\omega_s$ ) with respect to a stationary reference frame located in the stator, justifying in

this way the use of  $s$  as superscript for eq.(2.62).  $\vec{v}_r^r$ ,  $\vec{i}_r^r$  and  $\vec{\Psi}_r^r$  are the rotor voltage space vector, the rotor current space vector and the rotor flux space vector respectively. Since equations (2.45) - (2.47) are referred to the rotor, the rotation speed of these three vectors ( $\omega_r$ ) is measured with respect to a reference frame fixed with the rotor. Thus, the corresponding superscript for eq.(2.63) is  $r$ . Similarly to the case of the steady state model, the relation between the fluxes and currents of the machine can be described as:

$$\vec{\Psi}_s^s = L_s \vec{i}_s^s + L_m \vec{i}_r^s \quad (2.64)$$

$$\vec{\Psi}_r^r = L_m \vec{i}_s^r + L_r \vec{i}_r^r \quad (2.65)$$

In order to assemble equations (2.62) - (2.65) into a unified model, it is necessary to establish a common reference frame for all of them. Since the objective of this section is the development of the machine model in the stationary reference frame, eq.(2.63) and eq.(2.65) must be referred to it. Making use of eq.(2.61) it is obtained:

$$\begin{aligned} \vec{v}_r^s &= e^{j\theta_m} \vec{v}_r^r \\ \vec{v}_r^s &= R_r e^{j\theta_m} \vec{i}_r^r + e^{j\theta_m} \frac{d\vec{\Psi}_r^r}{dt} \\ \vec{v}_r^s &= R_r \vec{i}_r^s + \frac{d\vec{\Psi}_r^s}{dt} - j\omega_m \vec{\Psi}_r^s \end{aligned} \quad (2.66)$$

And,

$$\begin{aligned} \vec{\Psi}_r^s &= e^{j\theta_m} \vec{\Psi}_r^r \\ \vec{\Psi}_r^s &= L_m e^{j\theta_m} \vec{i}_s^r + L_r e^{j\theta_m} \vec{i}_r^r \\ \vec{\Psi}_r^s &= L_m \vec{i}_s^s + L_r \vec{i}_r^s \end{aligned} \quad (2.67)$$

Thus, the  $\alpha\beta$  model of the DFIM is fully described by the next set of equations:

$$\vec{v}_s^s = R_s \vec{i}_s^s + \frac{d\vec{\Psi}_s^s}{dt} \quad (2.68)$$

$$\vec{v}_r^s = R_r \vec{i}_r^s + \frac{d\vec{\Psi}_r^s}{dt} - j\omega_m \vec{\Psi}_r^s \quad (2.69)$$

$$\vec{\Psi}_s^s = L_s \vec{i}_s^s + L_m \vec{i}_r^s \quad (2.70)$$

$$\vec{\Psi}_r^s = L_m \vec{i}_s^s + L_r \vec{i}_r^s \quad (2.71)$$

The  $\alpha\beta$  components of these vectors are graphically represented by the equivalent circuits of Figure 2.11.

The power relations for the static reference frame are defined as:

$$P_s = \frac{3}{2} \operatorname{Re}\{\vec{v}_s \cdot \vec{i}_s^*\} = \frac{3}{2} (v_{\alpha s} i_{\alpha s} + v_{\beta s} i_{\beta s}) \quad (2.72)$$

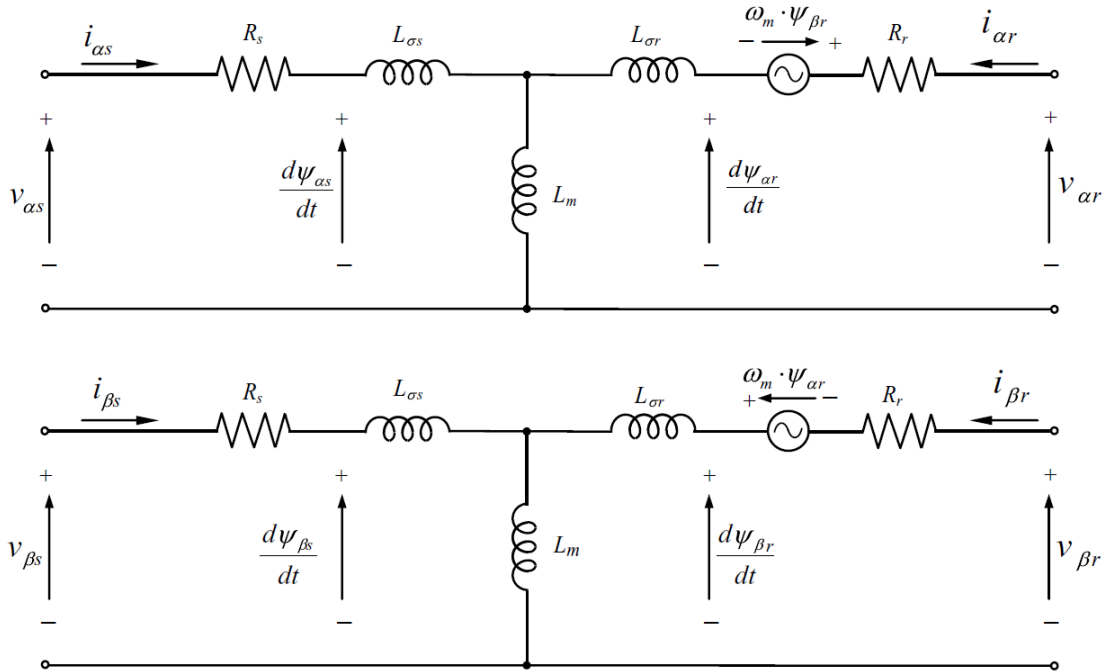
$$P_r = \frac{3}{2} \operatorname{Re}\{\vec{v}_r \cdot \vec{i}_r^*\} = \frac{3}{2} (v_{\alpha r} i_{\alpha r} + v_{\beta r} i_{\beta r}) \quad (2.73)$$

$$Q_s = \frac{3}{2} \operatorname{Im}\{\vec{v}_s \cdot \vec{i}_s^*\} = \frac{3}{2} (v_{\beta s} i_{\alpha s} - v_{\alpha s} i_{\beta s}) \quad (2.74)$$

$$Q_r = \frac{3}{2} \operatorname{Im}\{\vec{v}_r \cdot \vec{i}_r^*\} = \frac{3}{2} (v_{\beta r} i_{\alpha r} - v_{\alpha r} i_{\beta r}) \quad (2.75)$$

The term  $\frac{3}{2}$  is necessary in the power expression to maintain the correspondence with the powers obtained in the  $abc$  coordinate system (ABAD et al., 2011).

Figure 2.11 - DFIM  $\alpha\beta$  equivalent circuit



Source: (ABAD et al., 2011)

In order to facilitate the implementation of the  $\alpha\beta$  model in the simulation software, its steady state representation will be introduced next. Selecting the fluxes as space states variables, eq.(2.68) - eq.(2.71) are rearranged to form:

$$\frac{d}{dt} \begin{bmatrix} \vec{\Psi}_s^s \\ \vec{\Psi}_r^s \end{bmatrix} = \begin{bmatrix} \frac{-R_s}{\sigma L_s} & \frac{R_s L_m}{\sigma L_s L_r} \\ \frac{R_r L_m}{\sigma L_s L_r} & \frac{-R_s}{\sigma L_s} + j\omega_m \end{bmatrix} \cdot \begin{bmatrix} \vec{\Psi}_s^s \\ \vec{\Psi}_r^s \end{bmatrix} + \begin{bmatrix} \vec{v}_s^s \\ \vec{v}_r^s \end{bmatrix} \quad (2.76)$$

Expanding eq.(2.76) in the  $\alpha\beta$  components we have:

$$\frac{d}{dt} \begin{bmatrix} \Psi_{\alpha s} \\ \Psi_{\beta s} \\ \Psi_{\alpha r} \\ \Psi_{\beta r} \end{bmatrix} = \begin{bmatrix} \frac{-R_s}{\sigma L_s} & 0 & \frac{R_s L_m}{\sigma L_s L_r} & 0 \\ 0 & \frac{-R_s}{\sigma L_s} & 0 & \frac{R_s L_m}{\sigma L_s L_r} \\ \frac{R_r L_m}{\sigma L_s L_r} & 0 & \frac{-R_r}{\sigma L_r} & -\omega_m \\ 0 & \frac{R_r L_m}{\sigma L_s L_r} & \omega_m & \frac{-R_r}{\sigma L_r} \end{bmatrix} \cdot \begin{bmatrix} \Psi_{\alpha s} \\ \Psi_{\beta s} \\ \Psi_{\alpha r} \\ \Psi_{\beta r} \end{bmatrix} + \begin{bmatrix} v_{\alpha s} \\ v_{\beta s} \\ v_{\alpha r} \\ v_{\beta r} \end{bmatrix} \quad (2.77)$$

For our particular case, the selection of the currents as space state variables simplifies the interconnection of the machine model and the control system model. Under this new condition, eq.(2.76) becomes:

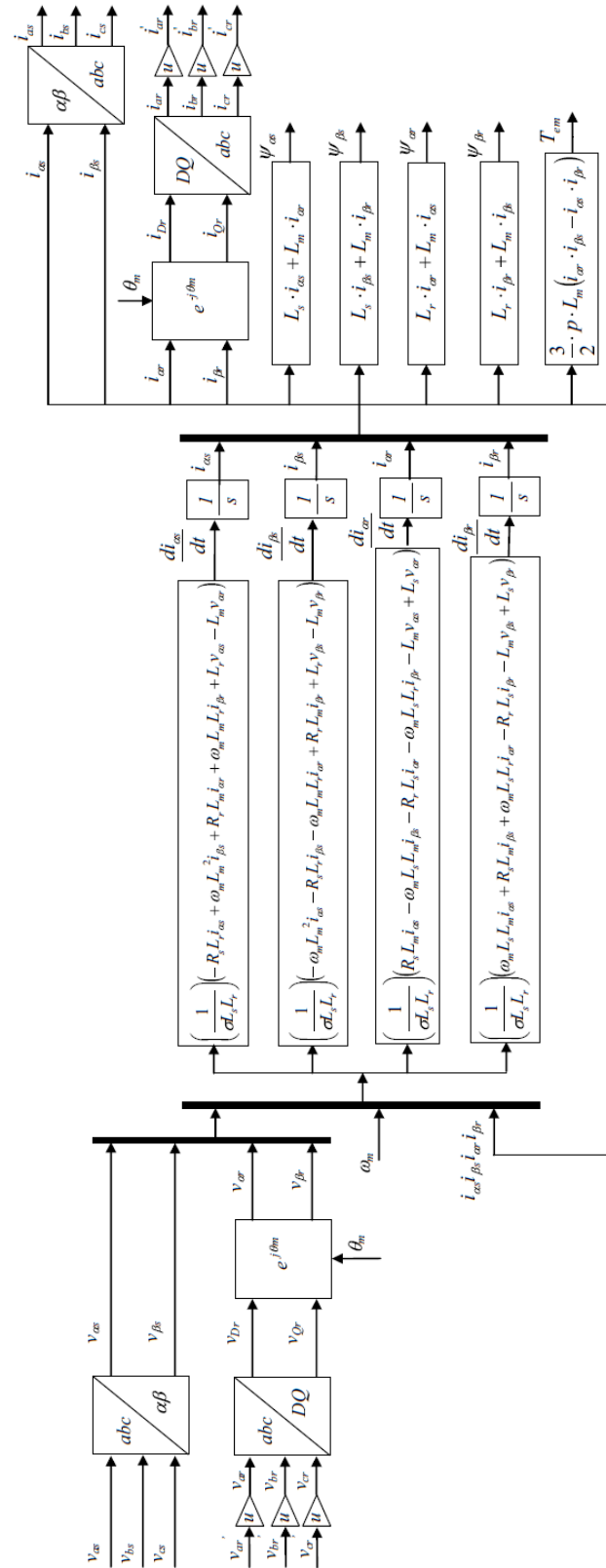
$$\frac{d}{dt} \begin{bmatrix} \vec{i}_s^s \\ \vec{i}_r^s \end{bmatrix} = \left( \frac{1}{\sigma L_s L_r} \right) \begin{bmatrix} -R_s L_r - j\omega_m L_m^2 & -R_r L_m - j\omega_m L_m L_r \\ -R_s L_m - j\omega_m L_m L_s & -R_r L_s + j\omega_m L_r L_s \end{bmatrix} \cdot \begin{bmatrix} \vec{i}_s^s \\ \vec{i}_r^s \end{bmatrix} + \left( \frac{1}{\sigma L_s L_r} \right) \begin{bmatrix} L_r & -L_m \\ -L_m & L_s \end{bmatrix} \cdot \begin{bmatrix} \vec{v}_s^s \\ \vec{v}_r^s \end{bmatrix} \quad (2.78)$$

Expanding eq.(2.78) in the  $\alpha\beta$  components we have:

$$\frac{d}{dt} \begin{bmatrix} i_{\alpha s} \\ i_{\beta s} \\ i_{\alpha r} \\ i_{\beta r} \end{bmatrix} = \left( \frac{1}{\sigma L_s L_r} \right) \begin{bmatrix} -R_s L_r & \omega_m L_m^2 & R_r L_m & \omega_m L_m L_r \\ -\omega_m L_m^2 & -R_s L_r & -\omega_m L_m L_r & R_r L_m \\ R_s L_m & -\omega_m L_m L_s & -R_r L_s & -\omega_m L_r L_s \\ \omega_m L_m L_s & R_s L_m & \omega_m L_r L_s & -R_r L_s \end{bmatrix} \cdot \begin{bmatrix} i_{\alpha s} \\ i_{\beta s} \\ i_{\alpha r} \\ i_{\beta r} \end{bmatrix} + \left( \frac{1}{\sigma L_s L_r} \right) \begin{bmatrix} L_r & 0 & -L_m & 0 \\ 0 & L_r & 0 & -L_m \\ -L_m & 0 & L_s & 0 \\ 0 & -L_m & 0 & L_s \end{bmatrix} \begin{bmatrix} v_{\alpha s} \\ v_{\beta s} \\ v_{\alpha r} \\ v_{\beta r} \end{bmatrix} \quad (2.79)$$

Before proceeding to the implementation of eq.(2.79) in the simulation software, it is necessary to clearly identify its inputs, outputs and entrance parameters. This model has as inputs the stator and rotor voltages referred to the stationary reference frame, as well as the angular frequency of the rotor. As entrance parameters we have the same electric quantities used for the steady state model: stator and rotor resistances and inductances, turns ratio and the number of poles. The outputs of the model are the stator and rotor currents and fluxes referred to the stationary reference frame and the electromagnetic torque. A detailed block diagram of the model is presented in Figure 2.12. It can be seen from it that the stator and rotor voltages in the  $abc$  coordinate system are referred to the stationary reference frame. Subsequently, eq.(2.79) is evaluated and the stator and rotor currents referred to the stationary reference frame are obtained as a result. From these currents, the stator and rotor fluxes as well as the electromagnetic torque are calculated. Finally, the currents are transformed back to the  $abc$  coordinate system, being ready to be used by the rotor side converter control system as will be seen ahead.

Figure 2.12 - DFIM dynamic model block representation



Source: (ABAD et al., 2011)

### 2.3. BEHAVIOR OF THE DFIM IN CASE OF THREE-PHASE VOLTAGE DIPS

One of the main advantages of using the DFIM for the wind power conversion process is its ability to work under a variable rotor speed. The variation range is limited to have an slip between -0.3 and 0.3 approximately. According to eq.(2.38), the active power flowing through the rotor is defined as the product between the stator power and the slip, which means that for this application the rotor active power is limited to maximum 30% of the rated stator power. A reduced amount of active power flowing through the rotor substantially diminishes the construction costs associated with this system when compared with full converter solutions. In contrast, the reduced size of the DFIM converter makes it vulnerable to overcurrents induced in the rotor in case of case of stator voltage dips. This phenomenon has been extensively studied in the technical literature and, as will be seen in Chapter 5, several protection strategies for the RSC have been proposed. In this section, a theoretical analysis of the DFIM reaction to full and partial balanced three-phase voltage dips will be presented.

#### 2.3.1. *emf* Induced in the rotor

According to Faraday's law of induction, when a conductor is in the presence of a time varying magnetic flux, and electromagnetic force is induced in it, which, in case of finding a conductive closed path, forces the circulation of electric currents. This is the case of the DFIM rotor when exposed to the circulating stator magnetic flux  $\vec{\Psi}_s$ . eq.(2.63) introduced the rotor voltage as:

$$\vec{v}_r^r = R_r \vec{i}_r^r + \frac{d}{dt} \vec{\Psi}_r^r \quad (2.80)$$

From eq.(2.64) and eq.(2.65) we have that the relation between the stator and rotor fluxes is:

$$\vec{\Psi}_r^r = \frac{L_m}{L_s} \vec{\Psi}_s^r + \sigma L_r \vec{i}_r^r \quad (2.81)$$

Combining eq.(2.80) and eq.(2.81) we obtain:

$$\vec{v}_r^r = \frac{L_m}{L_s} \frac{d}{dt} \vec{\Psi}_s^r + \left( R_r + \sigma L_r \frac{d}{dt} \right) \vec{i}_r^r \quad (2.82)$$

The first term of eq.(2.82) represents the *emf* induced in the rotor by the stator flux. The second term represents the voltage drops in the rotor resistance  $R_r$  and in the

transient inductance  $\sigma L_r$ . It is possible to isolate the first term by assuming that the rotor circuit is opened ( $I_r = 0$ ):

$$\vec{e}_r^r = \frac{L_m}{L_s} \frac{d}{dt} \vec{\Psi}_s^r \quad (2.83)$$

Referring this *emf* to the stator reference frame we have:

$$\vec{e}_r^s = \frac{L_m}{L_s} \left( \frac{d}{dt} \vec{\Psi}_s^s - j\omega_m \vec{\Psi}_s^s \right) \quad (2.84)$$

When the machine is in steady state, the stator is feed by a symmetric three-phase voltage source, whose phase voltages are describes by the equations:

$$v_a = \widehat{V}_g \cos(\omega_s t + \phi) \quad (2.85)$$

$$v_b = \widehat{V}_g \cos(\omega_s t + \phi - 2\pi/3) \quad (2.86)$$

$$v_c = \widehat{V}_g \cos(\omega_s t + \phi + 2\pi/3) \quad (2.87)$$

According to eq.(2.52), the space vector that represents the stator voltage is described by:

$$\vec{v}_s^s = \widehat{V}_g e^{j\phi} e^{j\omega_s t} \quad (2.88)$$

If in eq.(2.62) the voltage drop is neglected (due to the small value of the stator resistance), the stator flux vector can be expressed as:

$$\vec{\Psi}_s^s = \frac{\widehat{V}_g e^{j\phi}}{j\omega_s} e^{j\omega_s t} \quad (2.89)$$

Referring eq.(2.89) to the rotor reference frame we have:

$$\vec{\Psi}_s^r = \vec{\Psi}_s^s e^{-j\omega_m t} = \frac{\widehat{V}_g e^{j\phi}}{j\omega_s} e^{j(\omega_s - \omega_m)t} = \frac{\widehat{V}_g e^{j\phi}}{j\omega_s} e^{j\omega_r t} \quad (2.90)$$

Replacing this flux in eq.(2.83) the induced *emf* in the rotor is obtained:

$$\vec{e}_r^r = \frac{L_m}{L_s} \frac{d}{dt} \vec{\Psi}_s^r = j\omega_r \frac{L_m}{L_s} \vec{\Psi}_s^r = \omega_r \frac{L_m \widehat{V}_g e^{j\phi}}{L_s \omega_s} e^{j\omega_r t} \quad (2.91)$$

Where,

$$|\hat{E}_r| = \omega_r \frac{L_m \widehat{V}_g}{L_s \omega_s} = \widehat{V}_g \frac{L_m}{L_s} s \quad (2.92)$$

It can be seen from eq.(2.92) that the *emf* amplitude is directly related to the stator voltage amplitude and to the slip value. Since the slip magnitude is generally smaller than 0.3, the induced *emf* will have a maximum value of approximately 30% of the stator voltage for normal operation conditions.

### 2.3.2. Three-phase voltage dips

A three-phase voltage dip is defined as a sudden and symmetrical reduction of the voltage amplitude, for each one of the system phases. Such reduction can be caused by symmetric short circuits or by the start up of a motor near the point of measurements.

It is studied in this document the DFIM behavior in case of an abrupt voltage dip, that is an immediate variation of the amplitude value as represented by eq.(2.93).

$$\begin{aligned}\vec{v}_s^s(t < 0) &= \hat{V}_{pre} e^{j\omega_s t} \\ \vec{v}_s^s(t \geq 0) &= \hat{V}_{fault} e^{j\omega_s t}\end{aligned}\quad (2.93)$$

In order to approach to this phenomenon in a simpler way, it will be studied first the consequences on the machine of a total voltage dip and then the more common case of a partial voltage dip will be introduced.

### 2.3.3. Total voltage dip with open-circuited rotor

During a total three phase voltage dip, the voltage amplitude at the connection point of the DFIM with the grid is zero ( $V_s = 0$ ). According to the steady state theory presented in Section 2.1, a machine with its rotor open circuited ( $i_r = 0$ ) and no stator voltage is undoubtedly demagnetized, so no *emf* is induced in the rotor windings. However, this steady state is only achieved some time after the beginning of the dip (approximately 1s after the dip start for multimegawatt machines). In order to evaluate the machine's behavior during the transition between the pre-dip steady state and this no voltage steady state, the dynamic model of the machine presented in Section 2.2 has to be used. eq.(2.62) describes the voltage behavior of the machine's stator:

$$\frac{d}{dt} \vec{\psi}_s^s = \vec{v}_s^s - \frac{R_s}{L_s} \vec{\psi}_s^s \quad (2.94)$$

If the total dip condition is introduced, and the resultant differential equation is solved we obtain:

$$\frac{d}{dt} \vec{\psi}_s^s = -\frac{R_s}{L_s} \vec{\psi}_s^s \quad (2.95)$$

$$\vec{\psi}_s^s = \vec{\psi}_0 e^{-t/\tau_s} \quad (2.96)$$

Where  $\vec{\psi}_0$  is the initial amplitude of the flux and  $\tau_{s=L_s/R_s}$  is the stator time constant.

It is possible to see from eq.(2.96) that, after the dip beginning, the stator flux has a decaying exponential behavior, leading the machine to the expected demagnetized steady state. Considering that the magnetic flux is continuous by definition, since it is a state variable, the value of  $\vec{\psi}_0$  can be found by comparing the magnetic flux before and after the dip occurrence (eq.(2.97) and eq.(2.98) respectively).

$$\vec{\psi}_s^s(t < 0) = \frac{\hat{V}_{pre}}{j\omega_s} e^{j\omega_s t} \quad (2.97)$$

$$\vec{\psi}_s^s(t \geq 0) = \vec{\psi}_0 e^{-t/\tau_s} \quad (2.98)$$

These equations must have the same value at  $t = 0$ , which results in:

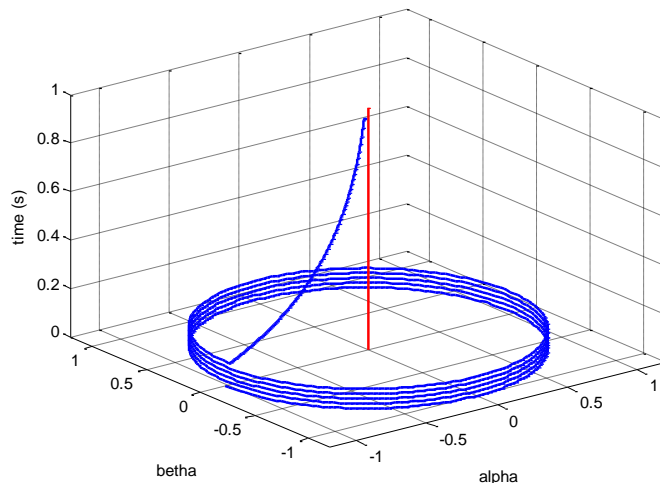
$$\vec{\psi}_0 = \frac{\hat{V}_{pre}}{j\omega_s} \quad (2.99)$$

$$\vec{\psi}_s^s(t \geq 0) = \frac{\hat{V}_{pre}}{j\omega_s} e^{-t/\tau_s} \quad (2.100)$$

From eq.(2.97) and eq.(2.100) it is possible to see that the rotating stator magnetic flux present before the dip, becomes a static decaying magnetic flux at the dip start. As will be seen in further sections, this fact is what generates the risk for the machine converter.

In Figure 2.13 is presented the trajectory of the stator flux space vector in time, in case of a full voltage dip. Before the voltage dip ( $t < 0.1$ ), the vector rotates at an angular speed  $\omega_s$ , maintaining a constant amplitude. From the beginning of the dip, until a time greater than 1s, the vector remains static, aligned with the  $\alpha$  axis and with a decaying amplitude described by eq.(2.100).

Figure 2.13 - Stator flux space vector trajectory



Remaining that the rotor current was assumed to be null, from eq.(2.64), eq.(2.97) and eq.(2.98) the stator current can be obtained:

$$\vec{i}_s^s(t < 0) = \frac{\vec{\Psi}_s^s(t < 0)}{L_s} \frac{\hat{V}_{pre}}{j\omega_s L_s} e^{j\omega_s t} \quad (2.101)$$

$$\vec{i}_s^s(t \geq 0) = \frac{\vec{\Psi}_s^s(t \geq 0)}{L_s} = \frac{\vec{\psi}_0 e^{-t/\tau_s}}{L_s} \quad (2.102)$$

For this situation, the stator current vector has the same behavior than the stator flux vector. Thus, before the dip the stator currents can be described by three sinusoidal signals, shifted in time  $120^\circ$  and oscillating with  $f_s$ . After the voltage dip beginning, the currents become decaying exponential signals tending to zero in a time defined by the stator time constant  $\tau_s$ .

As was seen in Section 2.3.1, the steady state rotating stator flux induces in the rotor winding an *emf* proportional to the product of the stator flux amplitude and the slip. This is no longer true in case of a full voltage dip. Due to the static characteristic of the stator flux in this condition, the relative rotation speed between the rotor windings and the stator flux is significantly greater, resulting in a substantial increment of the induced *emf* in the rotor windings. This can be proven by referring eq.(2.98) to the rotor reference frame:

$$\vec{\Psi}_s^r = \vec{\psi}_0 e^{-t/\tau_s} e^{-j\omega_m t} \quad (2.103)$$

Replacing it in eq.(2.91) we obtain the induced *emf*:

$$\vec{e}_r^r = -\frac{L_m}{L_s} \left( \frac{1}{\tau_s} + j\omega_m \right) \vec{\Psi}_s^r = -\frac{L_m}{L_s} \left( \frac{1}{\tau_s} + j\omega_m \right) \vec{\psi}_0 e^{-t/\tau_s} e^{-j\omega_m t} \quad (2.104)$$

The maximum amplitude of the induced *emf* can be found by replacing eq.(2.99) in eq.(2.104), considering the term  $\frac{1}{\tau_s}$  dispersive.

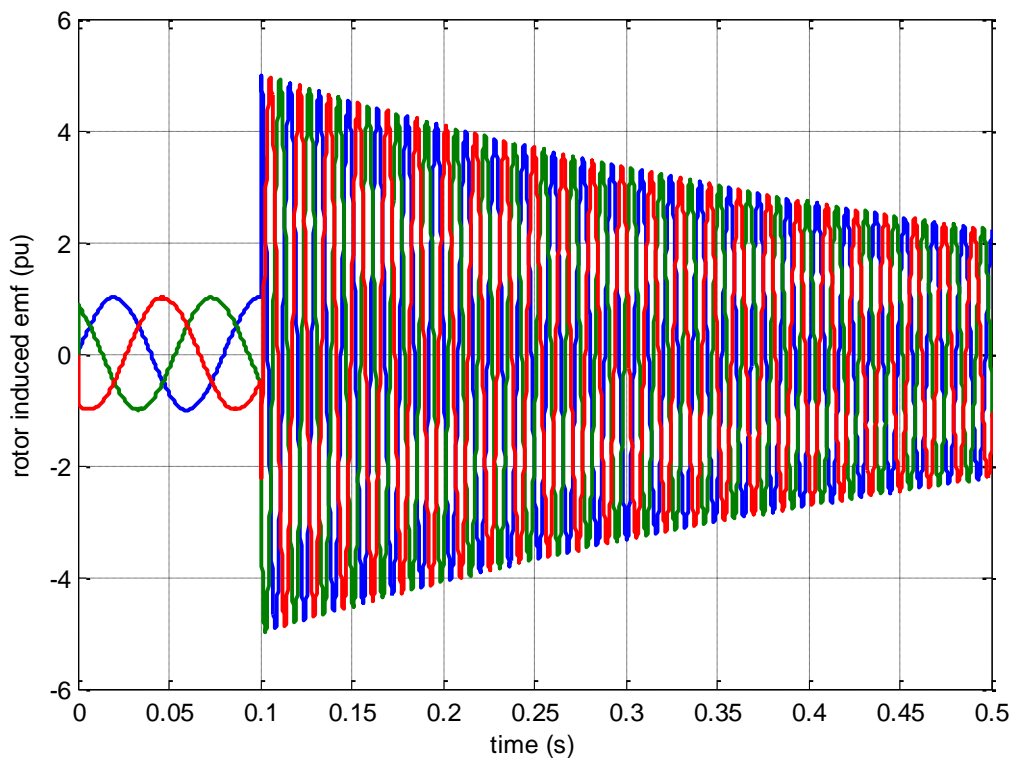
$$|\hat{E}_{r,max}| \approx \omega_r \frac{L_m}{L_s} \frac{\omega_m}{\omega_s} \hat{V}_{pre} = \hat{V}_{pre} \frac{L_m}{L_s} (1 - s) \quad (2.105)$$

Comparing eq.(2.92) and eq.(2.95) is possible to see that when a full voltage dip occurs, the induced *emf* amplitude rises  $\left(\frac{1}{s} - 1\right)$  times, to decrease exponentially at the same rate of the stator flux. Due to the already mentioned low rating of the converter, this increased *emf* threatens to saturate it. In this condition, the converter would not be able to control the rotor currents circulation, which would be only limited by the small rotor resistance.

From eq.(2.104) and eq.(2.105) is possible to evince that not only the *emf* amplitude varies due to the voltage dip, its frequency is also increased, reaching the

angular frequency of the rotor  $\omega_m$ . In Figure 2.14 is presented the *emf* induced in the rotor of a DFIM working at a slip  $s = -0.25$ , in the case of a full voltage dip. Before the dip, the frequency of the the *emf* signals is defined by the relation  $\omega_r = s\omega_s$ , that is a frequency of  $12.5\text{Hz}$ . When the dip starts, there is an increment in the maximum amplitude of  $\left(\frac{1}{-0.25} - 1\right)$  times, reaching an instantaneous value of  $5\text{pu}$ . The frequency for this new state has the same value of the rotor angular frequency, defined as  $\omega_r = \omega_m = (1 - s)\omega_s$ . This is a new frequency of  $62.5\text{Hz}$ . Finally, the decay time defined as five times the time constant, has a value of  $5 * \tau_s = 5 * \frac{L_s}{R_s} = 2.48\text{s}$ .

Figure 2.14 - *emf* induced in the DFIM rotor in case of a full voltage dip



#### 2.3.4. Partial voltage dip with open-circuited rotor

A partial voltage dip is defined as a reduction of the grid voltage amplitude between 0% and 100%. Thus, it is evident that a total voltage dip (100% of reduction), introduced in the last section, is a particular case of partial voltage dip. If a partial voltage dip occurs in  $t = 0$ , the stator voltage of the DFIM is defined as:

$$\begin{aligned}\vec{v}_s^s(t < 0) &= \hat{V}_{pre} e^{j\omega_s t} \\ \vec{v}_s^s(t \geq 0) &= (1 - d)\hat{V}_{pre} e^{j\omega_s t}\end{aligned}\quad (2.106)$$

Where,

$d$  = the depth of the dip, ranging between 0 and 1.

As stated by eq.(2.89), in steady state the stator flux is proportional to the stator voltage. In this way, it is possible to define the steady state stator flux before and after the voltage dip as:

$$\begin{aligned}\bar{\psi}_s^s(t < 0, \text{ at steady state}) &= \frac{\hat{V}_{pre}}{j\omega_s} e^{j\omega_s t} \\ \bar{\psi}_s^s(t \geq 0, \text{ at steady state}) &= \frac{(1 - d)\hat{V}_{pre}}{j\omega_s} e^{j\omega_s t}\end{aligned}\quad (2.107)$$

As in the case of the total voltage dip, it is not possible to have an abrupt change of the stator flux value due to its continuous nature. Thus, it is necessary to find the expression that describes its behavior during the transition between steady states. Using again eq.(2.62), the general behavior of the stator flux is:

$$\frac{d}{dt} \bar{\psi}_s^s = \vec{v}_s^s - \frac{R_s}{L_s} \bar{\psi}_s^s \quad (2.108)$$

The solution of any ordinary differential equation (e.g. eq.(2.108)) can be expressed as the addition of two parts: the particular and the homogeneous solution. The particular solution of eq.(2.108), also known as forced flux, corresponds to the steady state flux produces for the remaining stator voltage after the beginning of the dip. That is:

$$\bar{\psi}_{sf}^s = \frac{\hat{V}_{fault}}{j\omega_s} e^{j\omega_s t} = \frac{(1 - d)\hat{V}_{pre}}{j\omega_s} e^{j\omega_s t} \quad (2.109)$$

The homogeneous solution is a transitory flux generated by the sudden voltage change, which ensures the continuity of the stator flux. It is defined as:

$$\bar{\psi}_{sn}^s = \vec{\psi}_{n0} e^{-t/\tau_s} \quad (2.110)$$

Thus, the total stator flux in case is a partial voltage dip is:

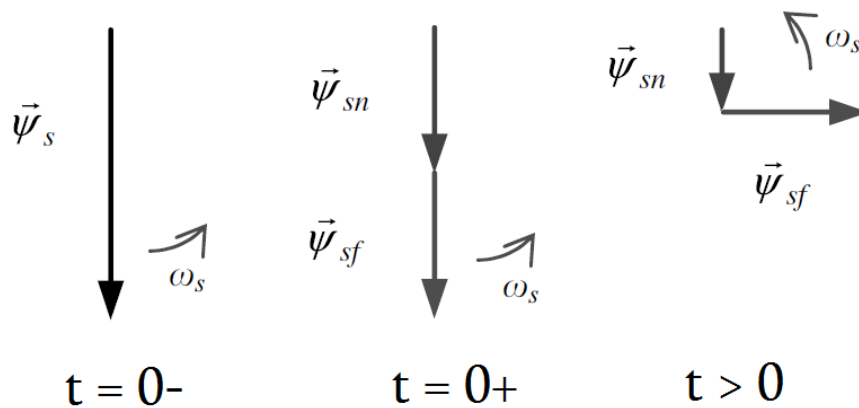
$$\bar{\psi}_s^s = \bar{\psi}_{sf}^s + \bar{\psi}_{sn}^s = \frac{\hat{V}_{fault}}{j\omega_s} e^{j\omega_s t} + \vec{\psi}_{n0} e^{-t/\tau_s} \quad (2.111)$$

In order to find the value of  $\vec{\psi}_{n0}$ , we make use of the fact that the stator flux must be identical immediately before and after the dip beginning. Comparing eq.(2.107) and eq.(2.111) for  $t = 0$  we obtain:

$$\vec{\psi}_{n0} = \frac{\hat{V}_{pre}}{j\omega_s} - \frac{\hat{V}_{fault}}{j\omega_s} = \frac{d\hat{V}_{pre}}{j\omega_s} \quad (2.112)$$

According to eq.(2.107), before the voltage dip the stator flux rotates at the synchronous speed  $\omega_s$ , with constant amplitude proportional to the stator voltage. When the dip starts, this flux is decomposed into a rotating component, with constant amplitude proportional to the new stator voltage ( $\vec{\psi}_{sf}^s$ ), and a static component with exponential decaying amplitude ( $\vec{\psi}_{sn}^s$ ). This is graphically presented in Figure 2.15. At the left side of this figure is shown the stator flux vector an instant before the voltage dip beginning, rotating with a speed  $\omega_s$ . Due to the continuous characteristic of the stator flux, an instant after the voltage dip beginning (as shown in the center of Figure 2.15), the stator flux maintains the same amplitude and orientation. However, it already can be decomposed in the static natural and the rotating forced components, maintaining this last the same rotation speed  $\omega_s$ . Finally, in the right side of the figure, are shown the natural and forced components some time after the voltage dip beginning. It is evident from this graph the reduction of the natural component amplitude, while the forced component amplitude remains constant and proportional to the new stator voltage.

Figure 2.15 - Stator flux behavior during a partial voltage dip



The trajectory of the stator flux vector in time, for a 50% voltage dip, is presented in Figure 2.16 and Figure 2.17. Before the voltage dip, the vector traces a circle with a 1pu radius, rotating at synchronous speed. After the dip beginning ( $t > 0.1s$ ), the circle radius is reduced proportionally to the stator voltage reduction, resulting in a 0.5pu radius circle. In order to maintain the continuity of the flux, the center of this new circle is shifted during a short period of time defined by the stator time constant

$\tau_s$ . This movement of the steady state circle represents the natural flux component described by equation 2.100, which at  $t = 0$  has an amplitude equal to 0.5pu.

Similarly with the total voltage dip case, the stator current can be found from the flux using eq.(2.64):

$$\vec{i}_s^s(t \geq 0) = \frac{\hat{V}_{fault}}{jL_s\omega_s} e^{j\omega_s t} + \frac{\vec{\psi}_{n0} e^{-t/\tau_s}}{L_s} \quad (2.113)$$

This current is seen at the stator terminals as the addition of a three phase sinusoidal component and a decaying exponential DC component.

Each one of the stator flux components ( $\vec{\Psi}_{sf}^s$  and  $\vec{\Psi}_{sn}^s$ ) induces in the rotor an *emf* component. They can be obtained combining eq.(2.109) and eq.(2.110) (referred to the rotor) with eq.(2.83).

$$\vec{e}_{rf}^r = \frac{L_m}{L_s} \frac{d}{dt} \vec{\Psi}_{sf}^r = \frac{L_m}{L_s} \hat{V}_{fault} e^{j\omega_r t} \quad (2.114)$$

$$\vec{e}_{rn}^r = \frac{L_m}{L_s} \frac{d}{dt} \vec{\Psi}_{sn}^r = -\frac{L_m}{L_s} j\omega_m \vec{\psi}_{n0} e^{-t/\tau_s} e^{-j\omega_m t} \quad (2.115)$$

As expected, the *emf* component induced by the forced flux is an AC voltage proportional to the stator voltage and to the slip. This result is identical to the one obtained for the steady state *emf* (eq.(2.95)). The *emf* induced by the natural component of the flux has the same structure than that induced in the case of a full voltage dip (eq.(2.104)), differing only in the value that the natural flux initial amplitude  $\vec{\psi}_{n0}$  assumes in each case in order to assure the continuity of the flux.

The addition of these components results in the induced *emf* vector, which can be expressed in terms of the dip depth and the slip as:

$$\vec{e}_r^r = \frac{L_m}{L_s} \hat{V}_{pre} (s(1-d)e^{j\omega_r t} - d(1-s)e^{-t/\tau_s} e^{-j\omega_m t}) \quad (2.116)$$

It is possible to see from eq.(2.116) that the induced *emf* is composed by two AC components, oscillating at different frequencies ( $\omega_r$  and  $-\omega_m$ ). This will cause the appearance of non-sinusoidal three phase voltages at the rotor terminals as shown in Figure 2.18. This figure presents the rotor induced *emf* in case of a 50% voltage dip, while the machine is working with a slip  $s = 0.25$ . It can also be seen that the *emf* reaches its maximum amplitude ( $\approx 3$ pu) during the first instants of the dip. According to eq.(2.116), the *emf* component induced by the natural flux contributes the most to this overvoltage, having at the beginning of the dip an amplitude  $k = 5$  times greater than the *emf* induced by the forced flux, where  $k$  is defined as:

$$k = \left( \frac{ds - d}{s - ds} \right) \quad (2.117)$$

Figure 2.16 - Stator flux space vector trajectory for a 50% voltage dip in time

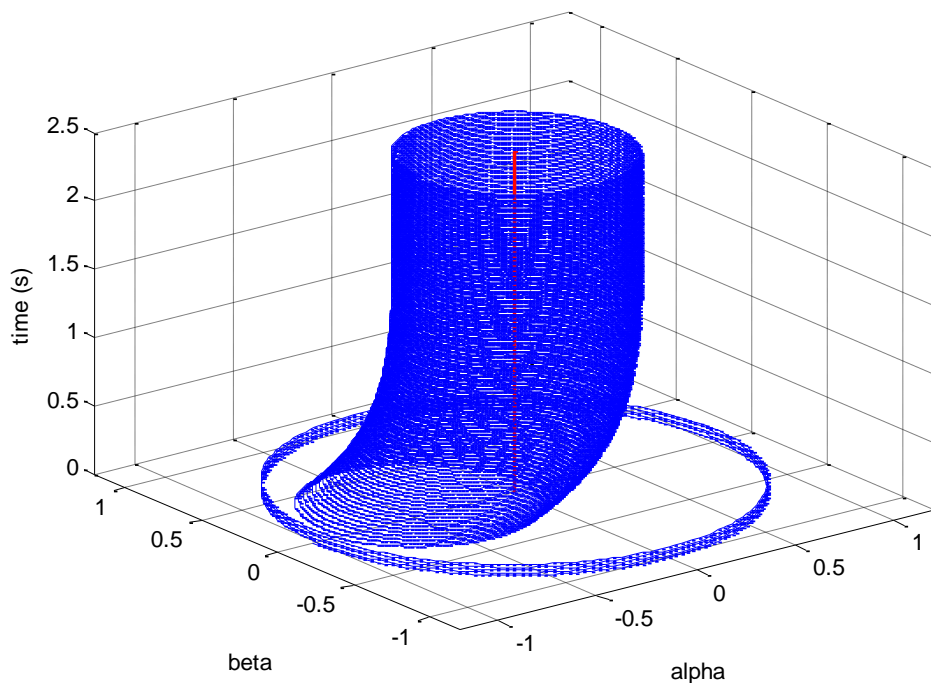


Figure 2.17 - Stator flux space vector trajectory for a 50% voltage dip

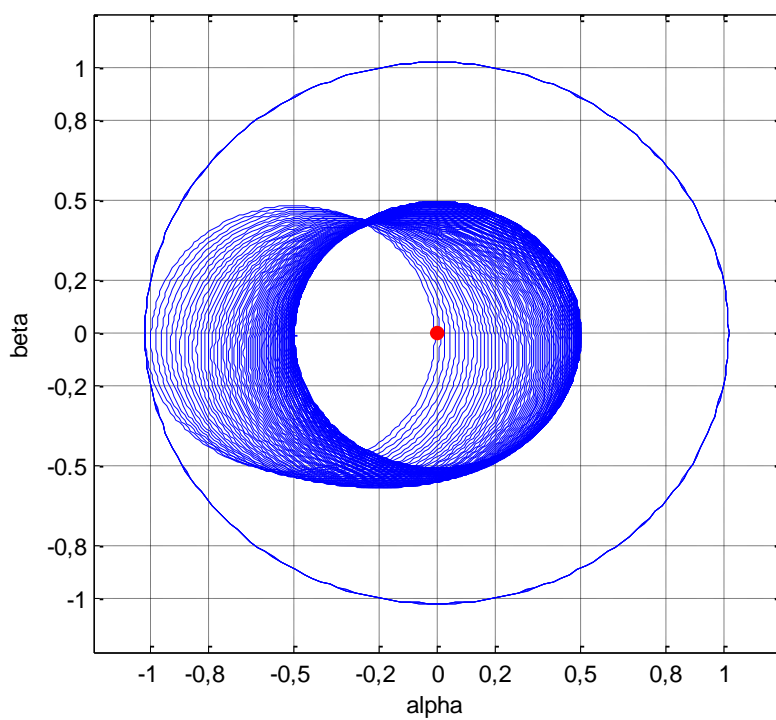
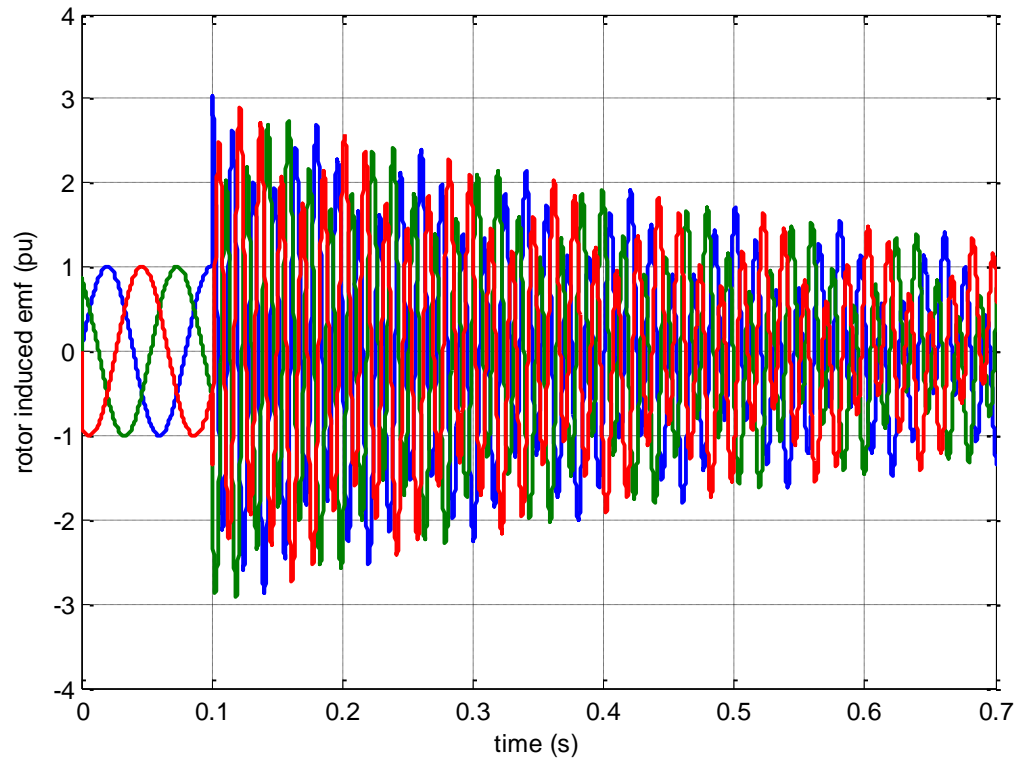
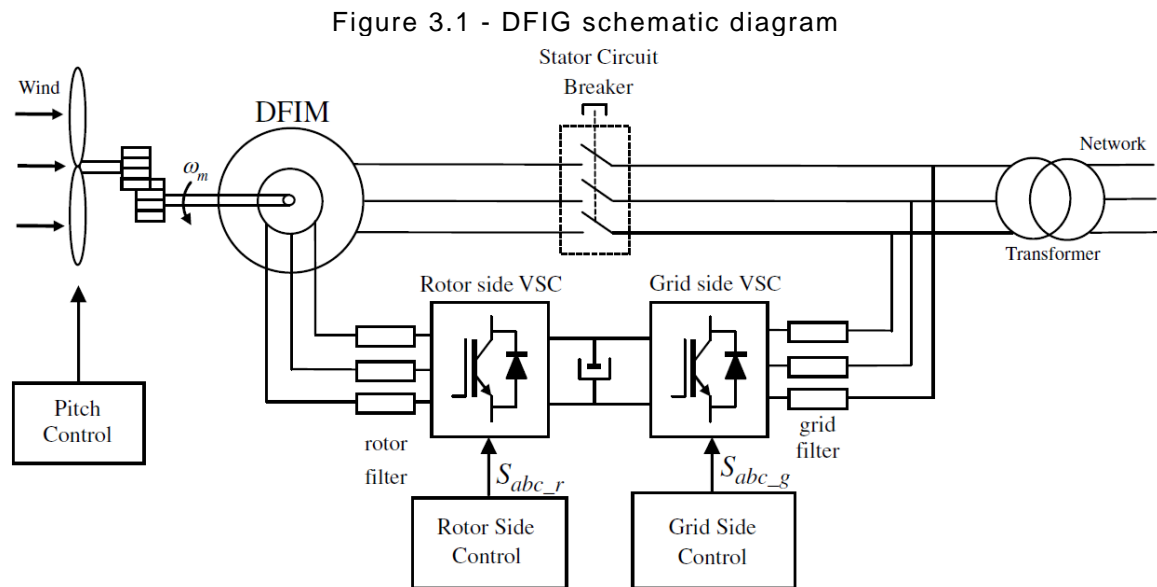


Figure 2.18 - *emf* induced in the rotor in case of a 50% voltage dip

### 3. BACK TO BACK POWER ELECTRONIC CONVERTER CONTROL

As was introduced in Section 2.1.3, the active and reactive power relations of the DFIM depend on the rotor current value. Thus, the control over the machine operation point is achieved through a strict control of the currents circulating in the rotor. In order to achieve this, it is common practice to use an arrangement known as a back to back power electronic converter, which is composed by two three-phase converters sharing a DC bus as shown in Figure 3.1. According to (ABAD et al., 2011), for wind turbines between 1.5 and 3MW manufacturers prefer the use of two-level IGBT based voltage source converters (VSC).



Source: (ABAD et al., 2011)

The function of the rotor side converter (RSC) is the generation of a three-phase voltage with variable amplitude and frequency, in order to control the current circulating in the rotor. As was seen in the last chapter, the frequency of the *emf* induced in the rotor in steady state is determined by the stator voltage frequency and the slip. Thus, this establishes the frequency that the voltage generated by the RSC must have in any operation point, in order to be compatible with the rotor circuit. As will be seen below, one of the requirements for the proper operation of the RSC, i.e., to generate the voltage indicated by the rotor side control system, is the access to an approximately constant voltage at its DC terminals. In order to achieve this, a capacitor (or combination of capacitors) is placed between the two

converters, using its energy storage capacity to avoid sudden voltage changes. This DC part of the back-to-back converter is typically known as DC-link. In order to maintain the DC-link voltage stable in the long term, it is necessary to ensure that the energy stored in the capacitor remains constant. Thus, the energy absorbed (or supplied) by the DFIM through its rotor, which flows across the DC-link, must be supplied (or absorbed) by an external circuit, in order to maintain the capacitor energy balance constant. This is the function of the grid side converter (GSC), which, under the command of the grid side control system, connects the grid and the DC-link, controlling the energy flux to maintain the capacitor voltage as constant as possible.

### 3.1. TWO LEVEL VOLTAGE SOURCE CONVERTER TOPOLOGY

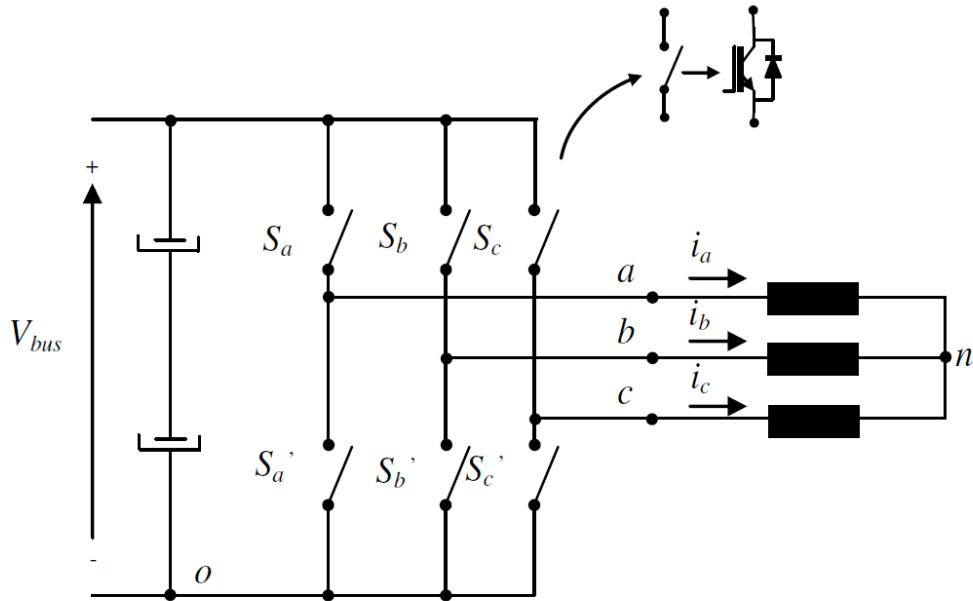
It was selected for the implementation of both the RSC and the GSC, the widely used two level voltage source converter (2L-VSC), which is composed by six bidirectional switches as shown in Figure 3.2. Even when in real applications each one of the switches is composed by a controlled semiconductor with a diode in anti-parallel, in this research all the switches were assumed to be ideal, considering that this would considerably simplify the modeling process of the complete system, without incurring in significant errors. As indicated in Figure 3.2, the three superior switches are controlled by the external signals  $S_a$ ,  $S_b$  and  $S_c$ , while the three inferior are controlled by the signals  $S'_a$ ,  $S'_b$  and  $S'_c$ . The relation between these control signals is:

$$S'_a = \overline{S_a} \quad (3.1)$$

$$S'_b = \overline{S_b} \quad (3.2)$$

$$S'_c = \overline{S_c} \quad (3.3)$$

Figure 3.2 - Two level voltage source converter



Source: (ABAD et al., 2011)

Thus, two switches belonging to the same converter leg will never be conducting simultaneously. Considering that the control signals are binary, the voltages between the points  $a$ ,  $b$  and  $c$  and the zero point of the DC bus can be expressed as:

$$v_{j0} = V_{bus}S_j \quad (3.4)$$

With  $S_j \in \{0,1\}$  and  $j = a, b, c$

Eq.(3.4) shows that there are two possible voltage levels for  $v_{j0}$ : zero and  $V_{bus}$ . For modeling purposes, it is useful to know the voltage between the converter output (points  $a$ ,  $b$  and  $c$ ) and the neutral point of the three-phase system ( $n$ ). This voltage, as shown in Figure 3.3 can be expressed as:

$$v_{jn} = v_{j0} - v_{n0} \text{ with } j = a, b, c \quad (3.5)$$

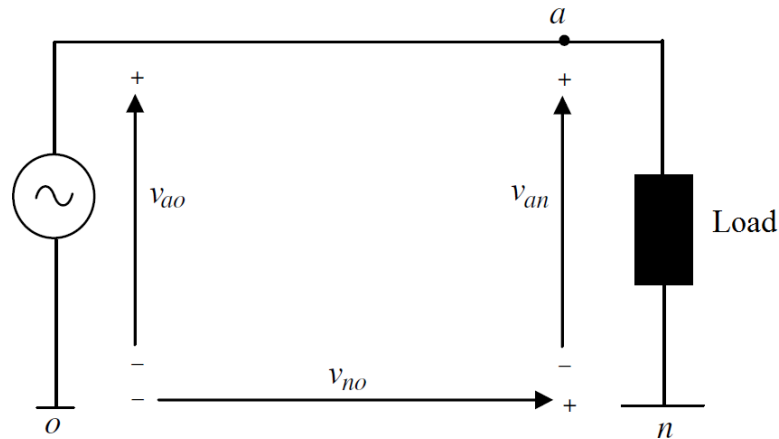
Assuming a balanced three phase behavior of these voltages, the next relation holds:

$$v_{an} + v_{bn} + v_{cn} = 0 \quad (3.6)$$

Substituting eq.(3.5) into eq.(3.6) we have:

$$v_{n0} = \frac{1}{3}(v_{a0} + v_{b0} + v_{c0}) \quad (3.7)$$

Figure 3.3 - Converter output circuit model



Substituting again into eq.(3.5) the desired output voltages are obtained:

$$v_{an} = \frac{2}{3}v_{ao} - \frac{1}{3}(v_{bo} + v_{co}) \quad (3.8)$$

$$v_{cn} = \frac{2}{3}v_{bo} - \frac{1}{3}(v_{ao} + v_{co}) \quad (3.9)$$

$$v_{cn} = \frac{2}{3}v_{co} - \frac{1}{3}(v_{bo} + v_{ao}) \quad (3.10)$$

These voltage can be expressed in terms of the control signals making use of eq.(3.4):

$$v_{an} = \frac{V_{bus}}{3}(2S_a - S_b - S_c) \quad (3.11)$$

$$v_{bn} = \frac{V_{bus}}{3}(2S_b - S_a - S_c) \quad (3.12)$$

$$v_{cn} = \frac{V_{bus}}{3}(2S_c - S_a - S_b) \quad (3.13)$$

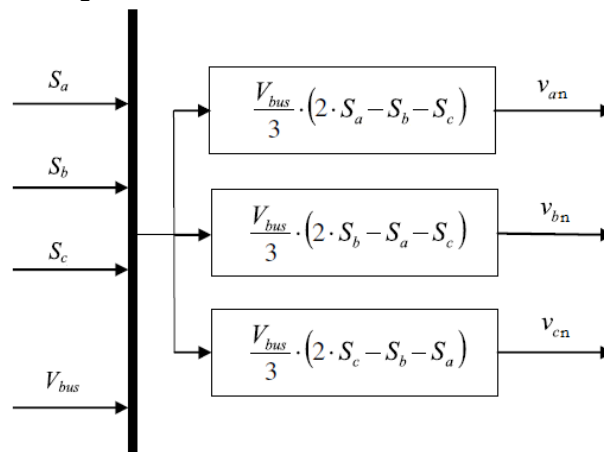
As shown in Table 3.1, due to the binary behavior of the control signals, eight different conduction states can be obtained. From this table, it is possible to see that the output voltages  $v_{an}$ ,  $v_{bn}$  and  $v_{cn}$  can reach five different voltage levels, which, as will be shown next, allow the recreation of three-phase sinusoidal voltages at the converter terminals with a moderate harmonic content.

Table 3.1 - 2L-VSC output voltage combinations

$S_a$	$S_b$	$S_c$	$v_{an}$	$v_{bn}$	$v_{cn}$
0	0	0	0	0	0
0	0	1	$-\frac{V_{bus}}{3}$	$-\frac{V_{bus}}{3}$	$2\frac{V_{bus}}{3}$
0	1	0	$-\frac{V_{bus}}{3}$	$2\frac{V_{bus}}{3}$	$-\frac{V_{bus}}{3}$
0	1	1	$-2\frac{V_{bus}}{3}$	$\frac{V_{bus}}{3}$	$\frac{V_{bus}}{3}$
1	0	0	$2\frac{V_{bus}}{3}$	$-\frac{V_{bus}}{3}$	$-\frac{V_{bus}}{3}$
1	0	1	$\frac{V_{bus}}{3}$	$-2\frac{V_{bus}}{3}$	$\frac{V_{bus}}{3}$
1	1	0	$\frac{V_{bus}}{3}$	$\frac{V_{bus}}{3}$	$-2\frac{V_{bus}}{3}$
1	1	1	0	0	0

The simulation model of the voltage source converter can be obtained from equations 3.11, 3.12 and 3.13. This, has as inputs the switching control signals ( $S_a$ ,  $S_b$  and  $S_c$ ) and the DC-link voltage ( $V_{bus}$ ), and as output the voltage at the converter terminals referred to the system neuter. In Figure 3.4 is presented a graphical representation of this model.

Figure 3.4 - 2L-VSC simulation model



Source: (ABAD et al., 2011)

### 3.2. 2L-VSC CONTROL SIGNALS GENERATION

In order to generate the desired three-phase sinusoidal voltages at the converter 2L-VSC terminals, several strategies for the generation of the switching control signals, known as modulation laws, can be used. For the development of this research, it was selected the Sinusoidal Pulse Width Modulation strategy (PWM), due to its simplicity and acceptable harmonic content generation (VASCA; IANNELLI, 2012).

#### 3.2.1. Sinusoidal Pulse Width Modulation (PWM)

This widely known modulation law compares the reference three-phase voltages generated by the converter control system, with a high frequency triangular signal, following the law presented in eq.(3.14) for the generation of the control signals:

$$S_j = 1 \text{ if } v_j^* = V_{tri} \text{ with } j = a, b, c \quad (3.14)$$

Where,

$v_a^*, v_b^*, v_c^*$  = reference phase voltages generated by the control system

$V_{tri}$  = triangular signal

The relation between the amplitude of the triangular signal and the reference signal, known as amplitude modulation index ( $m_a$ ), can be expressed as:

$$m_a = \frac{|v^*|}{|v_{tri}|} \quad (3.15)$$

As presented in (STOJAN; MILANOVIC, 2010), When  $m_a$  is smaller than 1, the output voltage fundamental component linearly depends on  $m_a$  as:

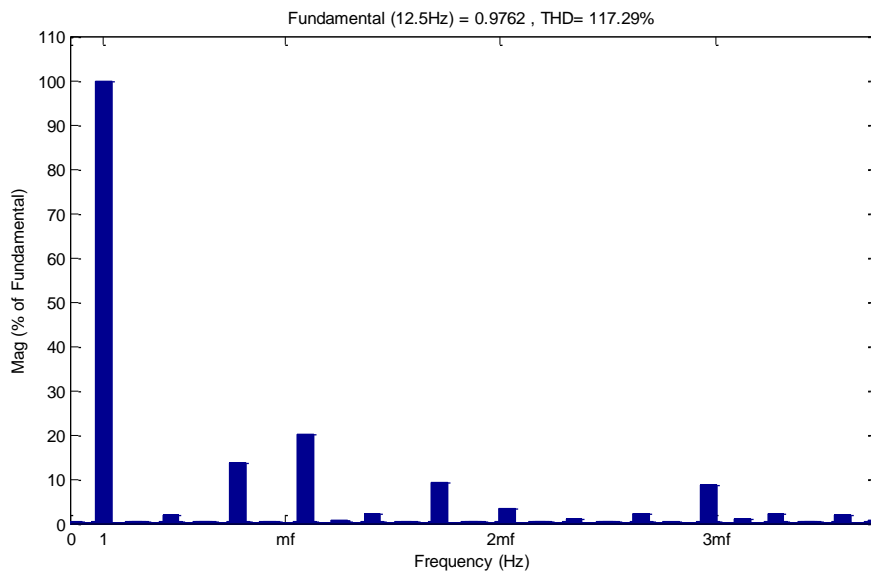
$$\langle v_{an} \rangle_1 = m_a \cdot \frac{V_{bus}}{2} \text{ for } m_a \leq 1 \quad (3.16)$$

From this last equation, it is possible to see that the maximum achievable output voltage without over-modulation ( $m_a \leq 1$ ) is  $\frac{V_{bus}}{2}$ . A greater maximum voltage could be achieved if over-modulation is allowed. However, this would cause a substantial increment of the output voltage total harmonic distortion (THD) together with a non-linear relation of this voltage with  $m_a$ . For this reasons over-modulation was avoided in the implementation of the modulation strategy.

The relation between the triangular signal and the reference signal frequencies ( $m_f$ ), defined in eq.(3.17), strongly influences the harmonic content of the output voltages. As can be seen in Figure 3.5, the frequency of the generated harmonics depends directly on  $m_f$  and its multiples, which indicates that the greater the frequency of the triangular signal (the greater the value of  $m_f$ ), the further the harmonic content will be from the fundamental frequency. Nevertheless, according to eq.(3.14), any increment of the triangular signal frequency has as a consequence an increment of switching frequency, which would lead to high switching losses in the semiconductors. Thus, it is necessary to establish a compromise between the power losses and the quality of the output voltage.

$$m_f = \frac{f_{tri}}{f_{ref}} \quad (3.17)$$

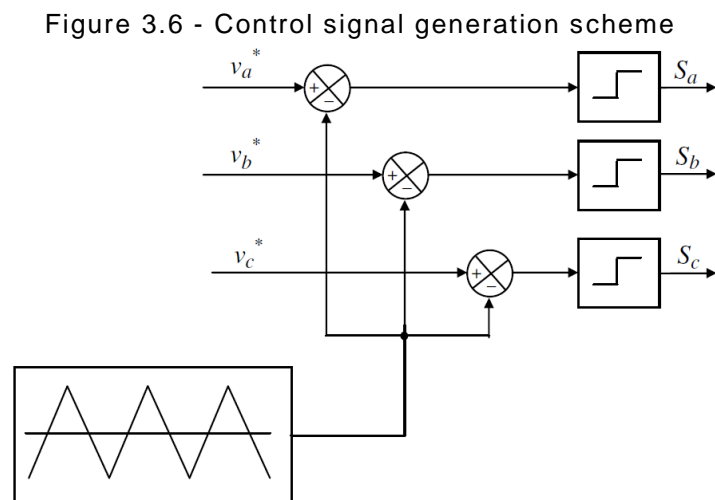
Figure 3.5 - Converter output voltage harmonic content



Finally, the block diagram representing the sinusoidal PWM modulation strategy is presented in Figure 3.6. This simplified modelling approach was used for both the RSC and GSC, requiring as input the reference signals produced by the respective control systems.

### 3.3. GRID AND ROTOR SIDE FILTERS

As presented in Figure 3.1, filters are normally installed at the two ends of the back to back converter, intended to improve its behavior and the quality of the produced voltage signals. A description of this devices and its implementation in the model is presented next.

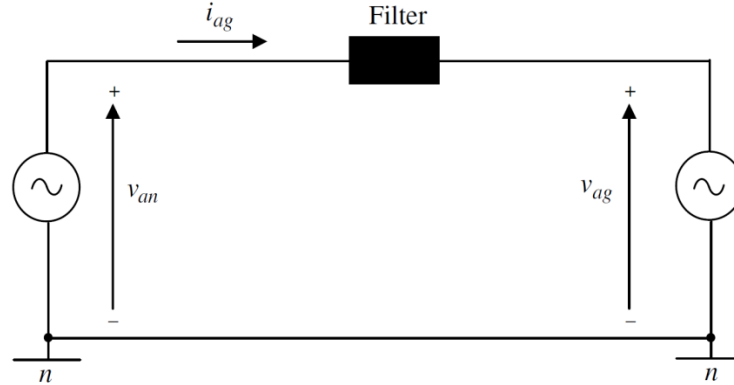


Source: (ABAD et al., 2011)

#### 3.3.1. Grid side inductive filter

This filter is intended to reduce the harmonic content of the GSC output voltage. It is normally composed by at least three series inductances, which connect the GSC output with the grid. In order to derive the equations necessary for the modeling process, a single-phase representation of the GSC can be used, under the assumption of a balanced grid voltage. In Figure 3.7 is presented the equivalent circuit for one of the phases, having that  $v_{an}$  represents the GSC output voltage referred to the system neuter point,  $v_{ag}$  is the phase grid voltage and  $i_{ag}$  is the current circulating in this circuit.

Figure 3.7 - Grid side converter equivalent circuit



Source: (ABAD et al., 2011)

The electric equations describing the behavior of each one of the phases can be expressed as:

$$v_{an} = R_f i_{ag} + L_f \frac{di_{ag}}{dt} + v_{ag} \quad (3.18)$$

$$v_{bn} = R_f i_{bg} + L_f \frac{di_{bg}}{dt} + v_{bg} \quad (3.19)$$

$$v_{cn} = R_f i_{cg} + L_f \frac{di_{cg}}{dt} + v_{cg} \quad (3.20)$$

Where,

$L_f$  = inductance of the grid side filter (H)

$R_f$  = Resistive part of the grid side filter ( $\Omega$ )

In order to facilitate the modeling process, it is convenient to isolate the derivative term of these equations, which results in:

$$\frac{di_{ag}}{dt} = \frac{1}{L_f} (v_{an} - R_f i_{ag} - v_{ag}) \quad (3.18)$$

$$\frac{di_{bg}}{dt} = \frac{1}{L_f} (v_{bn} - R_f i_{bg} - v_{bg}) \quad (3.19)$$

$$\frac{di_{cg}}{dt} = \frac{1}{L_f} (v_{cn} - R_f i_{cg} - v_{cg}) \quad (3.20)$$

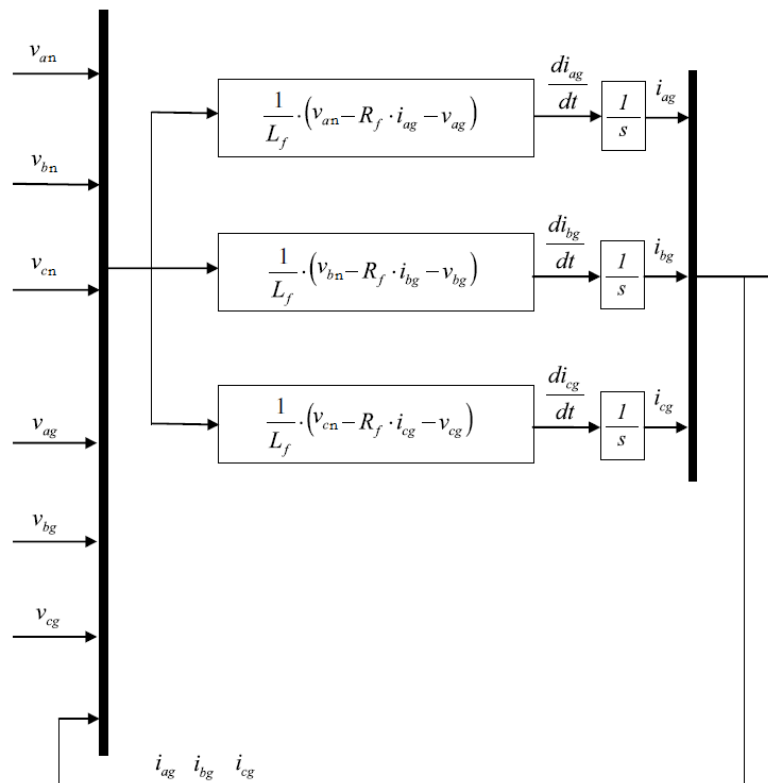
The graphical representation of equations (3.18), (3.19) and (3.20) is presented in Figure 3.8. Its output is the current injected (or extracted) to the grid, allowing a further calculation of the power exchange between the GSC and the power system.

### 3.3.2. Rotor side inductive $dv/dt$ filter

The objective of this filter is to mitigate the negative effects of the high  $dv/dt$  generated by the RSC in its operation (ANIRUDH; VINOD, 2010). This fast voltage variation causes among other things:

- Voltage reflections in the cable connecting the RSC and the DFIM rotor, which can cause overvoltages and over currents.
- Increased ground currents and bearing current.
- Electromagnetic emission from the device.

Figure 3.8 - Grid side converter and filter simulation models

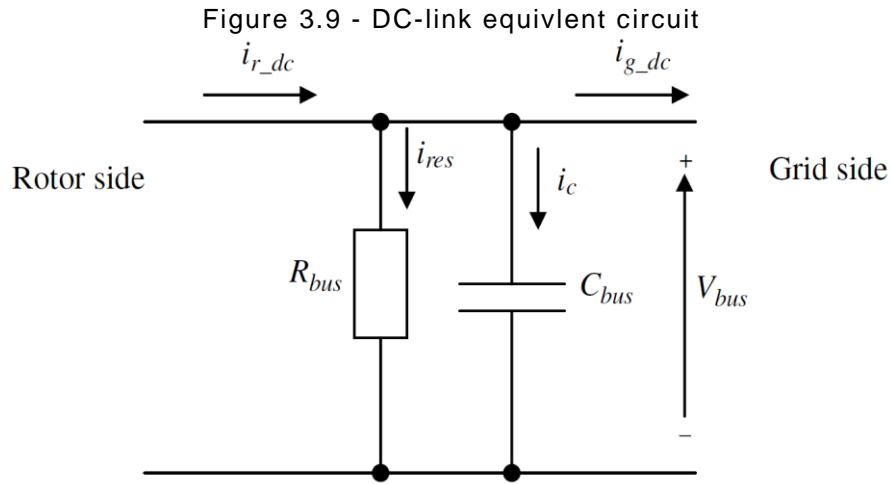


Source: (ABAD et al., 2011)

Since for this research the influence of the cable connecting the RSC and the rotor was assumed to be negligible, and the leakage capacitances of the machine were not considered in the model, the use of the  $dv/dt$  filter in the modeling process is not justified. Thus, it is assumed a direct connection of the RSC and the rotor of the DFIM.

### 3.4. DC-LINK

The last component of the back to back converter is the direct current interface between the RSC and GSC known as DC-Link. As was previously mentioned, the DC-link is composed by a capacitor (or group of capacitors) in parallel with a high value resistance, as shown in Figure 3.9.



The DC voltage can be expressed as a function of the current flowing through the capacitor as:

$$V_{bus} = \frac{1}{C_{bus}} \int i_c dt \quad (3.21)$$

According to the notation of Figure 3.7, the current circulating through the capacitor is:

$$i_c = i_{r\_dc} - i_{g\_dc} - i_{res} \quad (3.22)$$

Where,

$i_{r\_dc}$  = Current flowing from the RSC to the DC-link (A)

$i_{g\_dc}$  = Current flowing from the DC-link to the GSC (A)

$i_{res}$  = Current flowing through the resistance  $R_{bus}$  (A)

After a short analysis of Figure 3.9, it is possible to see that these currents can be defined as:

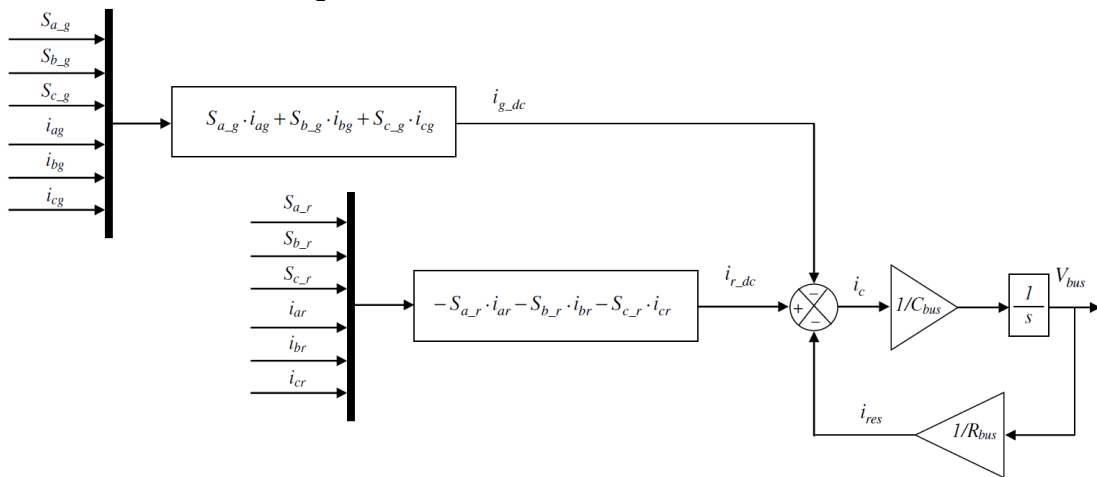
$$i_{r\_dc} = -S_{a\_r}i_{ar} - S_{b\_r}i_{br} - S_{c\_r}i_{cr} \quad (3.23)$$

$$i_{g\_dc} = -S_{a\_g}i_{ag} - S_{b\_g}i_{bg} - S_{c\_g}i_{cg} \quad (3.24)$$

$$i_{res} = \frac{V_{bus}}{R_{bus}} \quad (3.25)$$

Introducing equations (3.23), (3.24) and 3.25 into eq.(3.22) and applying the integration proposed by eq.(3.31), the model of the DC-link in terms of the control signals and converter output currents is obtained. In Figure 3.10 is presented its corresponding graphical representation.

Figure 3.10 - DC-link simulation model

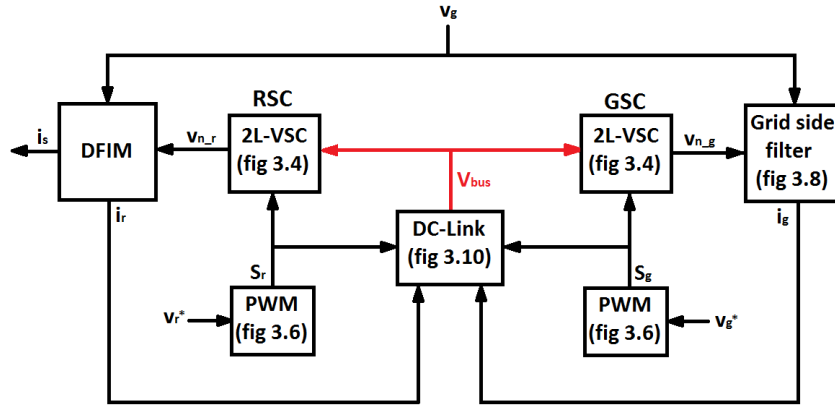


Source: (ABAD et al., 2011)

### 3.5. BACK TO BACK CONVERTER COMPLETE MODEL

It is possible now to assemble the complete model of the back to back converter, making use of the components presented in Figures 3.4, 3.6, 3.8 and 3.10. In Figure 3.11 is presented a block diagram of this assembly. It is worthy to notice that the red lines represent the transmission of a unique signal, e.g., the DC-link voltage, while the black lines represent the transmission of three signals, e.g., the three-phase rotor current or the control signals. It is also important to mention that the voltage references  $v_r^*$  and  $v_g^*$  are generated by the rotor side and grid side control systems respectively. These control systems are the object of study of the next chapter.

Figure 3.11 - Complete DFIG simulation model



### 3.6. GSC CONTROL SYSTEM

As mentioned in the introduction of this chapter, the main objective of the GSC control system is to establish the voltage references that the GSC must follow, in order to ensure a constant DC-link voltage. The magnitude of this voltage depends on the amount of energy stored in the DC-link capacitor. Thus, the strategy adopted for the voltage control is the regulation of the active power flux between the DC-link and the grid, in order to maintain the energy stored by the capacitor constant.

It is now necessary to define the power transference between the GSC and the grid. As mentioned in Section 2.2.1, the use of a reference frame rotating at synchronous speed simplifies the GSC control system since it allows an independent control of the active and reactive powers as shown next.

#### 3.6.1. Grid side system $dq$ model

The grid side system presented in Figure 3.7 is described in the stationary  $abc$  reference frame by equations (3.18), (3.19) and (3.20). Using equations (1.55) and (1.58), these equations are referred to a synchronous rotating reference frame, resulting in the  $dq$  model of the system:

$$v_{df} = R_f i_{dg} + L_f \frac{di_{dg}}{dt} + v_{dg} - \omega_s i_{qg} \quad (3.26)$$

$$v_{qf} = R_f i_{qg} + L_f \frac{di_{qg}}{dt} + v_{qg} + \omega_s L_f i_{dg} \quad (3.27)$$

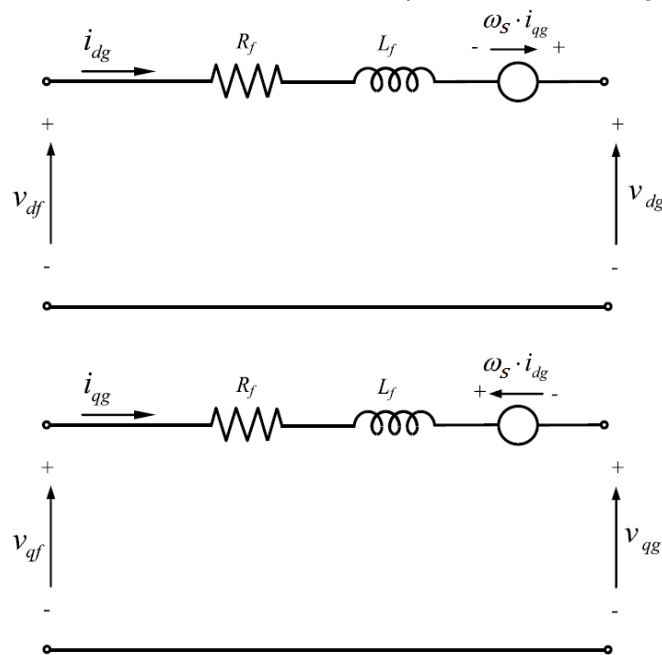
The circuitual representation of these equations is presented in Figure 3.12.

In order to achieve the decoupling of the active and reactive powers, it is necessary to align the direct axis of the rotating reference frame with the space vector representing the grid voltage  $\vec{v}_g$  as shown in Figure 3.13 (ABAD et al., 2011). This alignment yields in:

$$v_{dg} = |\vec{v}_g| \quad (3.28)$$

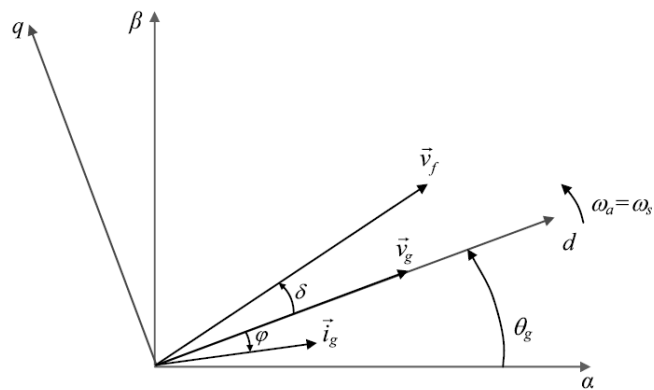
$$v_{qg} = 0 \quad (3.29)$$

Figure 3.12 -Grid side converter equivalent circuit  $dq$  model



Source: (LÓPEZ et al., 2008)

Figure 3.13 - Rotating space vectors diagram



Source: (ABAD et al., 2011)

Introducing these results into equations (3.26) and (3.27) we obtain a simplified version of the  $dq$  model:

$$v_{df} = R_f i_{dg} + L_f \frac{di_{dg}}{dt} + v_{dg} - \omega_s L_f i_{qg} \quad (3.30)$$

$$v_{qf} = R_f i_{qg} + L_f \frac{di_{qg}}{dt} + \omega_s L_f i_{dg} \quad (3.31)$$

The alignment with the grid voltage vector not only simplify the  $dq$  model, it also has an influence on the system power definitions. In the  $dq$  reference frame, the active and reactive power transferred to the grid can be addressed as:

$$P_g = \frac{3}{2} \text{Re}\{\vec{v}_g \cdot \vec{i}_g\} = \frac{3}{2} (v_{dg} i_{dg} + v_{qg} i_{qg}) \quad (3.32)$$

$$q_g = \frac{3}{2} \text{Im}\{\vec{v}_g \cdot \vec{i}_g\} = \frac{3}{2} (v_{qg} i_{dg} - v_{dg} i_{qg}) \quad (3.33)$$

Replacing equations (3.28) and (3.29) into these last two equations we obtained:

$$P_g = \frac{3}{2} v_{dg} i_{dg} = \frac{3}{2} |\vec{v}_g| i_{dg} \quad (3.34)$$

$$q_g = -\frac{3}{2} v_{dg} i_{qg} = -\frac{3}{2} |\vec{v}_g| i_{qg} \quad (3.35)$$

Since under ideal conditions the grid voltage amplitude  $|\vec{v}_g|$  remains constant, it is possible to evince in equations (3.34) and (3.35) that the active and reactive power are completely decoupled. Thus, the active power transferred to the grid depends only on the direct component of the current  $i_{dg}$  and the reactive power on the quadrature component of the current  $i_{qg}$ . This fact is used by the control system to indirectly control the DC-link voltage, by controlling the amount of energy stored in the DC-link capacitor.

### 3.6.2. Grid voltage orientated vector control

According to chapter 2, part of the power generated (or consumed) by the DFIM is delivered (or absorbed) through the rotor of the machine. This power inevitably flows through the RSC, increasing (or decreasing) the amount of energy stored in the DC-link capacitor if no countermeasure is adopted. Thus, it is the function of the GSC to provide a path for this energy to be evacuated (or supplied) from (or into) the DC-link, in such way that the total energy stored in the DC-link capacitor (and in consequence its voltage) remains constant.

The vector control technique has been widely used for the control of squirrel cage motors, using the fact that if the stator current vector is referred to a rotating reference frame aligned with the rotor flux, the electromagnetic torque and the rotor flux can be independently controlled by modifying the direct and quadrature components of the stator current.

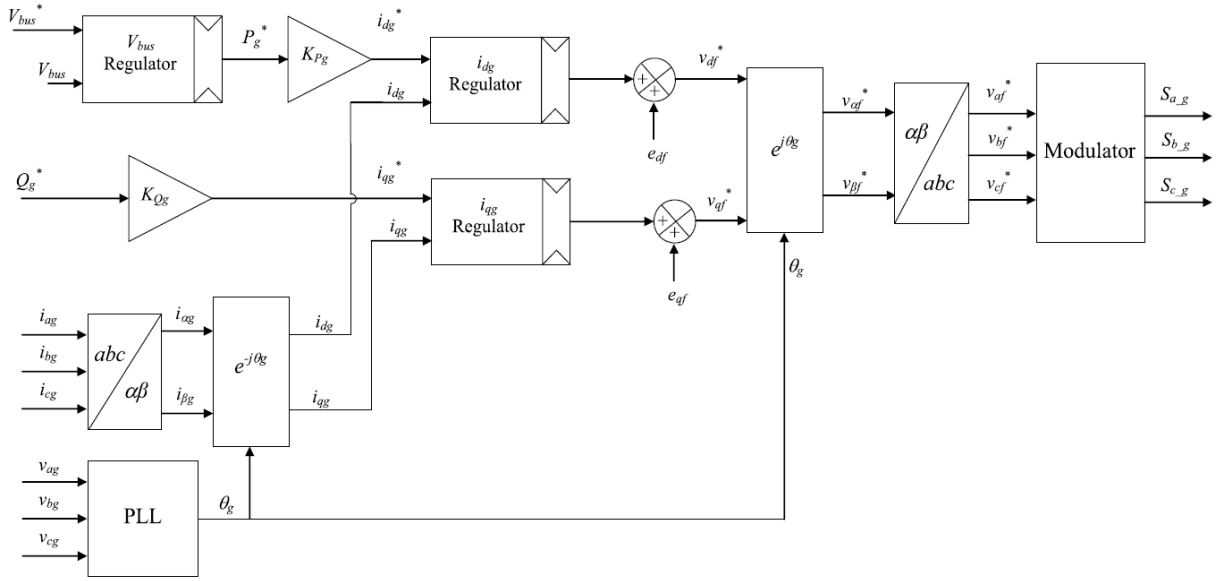
A similar approach can be used for the GSC control system. According to equations 3.34 and 3.35, if the direct axis of a rotating reference frame is aligned with the grid voltage vector, an independent control of the active and reactive powers transferred to the grid can be achieved by modifying the direct and quadrature components of the line current.

It is well known at this point that the GSC can be considered an ideal voltage source. Thus, the control over the current components must be indirectly performed using the relations presented in equations (3.30) and (3.31). These equations show that any variation of the voltage at the GSC forces the current circulating in the grid side circuit to vary in the same direction. These concepts were used to create the control system diagram presented by (QUANG; DITTRICH, 2008) and reproduced in Figure 3.14.

As expected, this control system has two clearly defined branches: one for the reactive power control and one for the DC-link voltage control. In the case of the former, due to the already mentioned relation between the DC link capacitor voltage and the power transference with the grid, the active power reference ( $P_g^*$ ) can be defined as the output of a PI controller having the DC-link voltage reference ( $V_{bus}^*$ ) and the measured DC-link voltage ( $V_{bus}$ ) as inputs. According to eq.(3.4), the direct axis grid current reference ( $i_{dg}^*$ ) is the product of the active power reference and a constant ( $K_{Pg}$ ) defined as:

$$K_{Pg} = \frac{1}{\frac{3}{2}v_{dg}} \quad (3.36)$$

Figure 3.14 - Grid side converter control system



Source: (ABAD et al., 2011)

The direct axis GSC voltage reference ( $V_{dn}^*$ ) can be obtained from  $i_{dg}^*$  as the output of a, including as a feed-forward input the coupling term  $e_{df}$ , in order to improve the dynamic response of the control system.

As introduced before, due to the relation between the GSC output voltage and the grid system current (eq.(3.30)), the direct axis GSC voltage reference ( $V_{dn}^*$ ) can be obtained as the output of a PI controller applied to  $i_{dg}^*$  and the measured grid system direct current ( $i_{dg}$ ). In order to improve the dynamic response of the control system, the coupling term  $e_{df}$  is included as a feed-forward input. This coupling term is defined as:

$$e_{df} = -\omega_s L_f i_{qg} \quad (3.37)$$

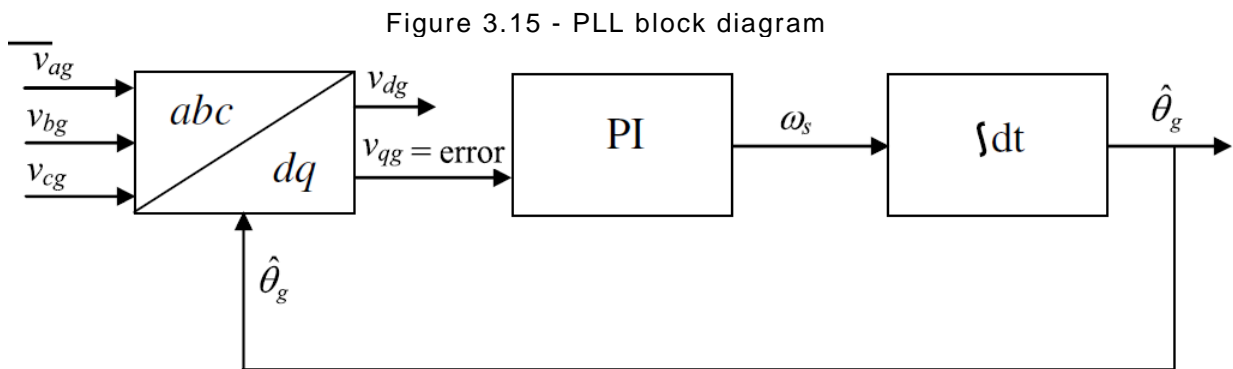
The control branch in charge of the reactive power transference has a very similar topology. As can be seen in Figure 3.14, the only difference between them is that the reactive power control branch uses one PI controller, since the variable to be controlled is directly the reactive power transferred to the grid ( $Q_g^*$ ). The constant relating the reactive power and the quadrature grid current ( $K_{Qg}$ ) and the corresponding coupling term ( $e_{df}$ ) are defined by equations (3.35) and (3.31) as:

$$K_{Qg} = \frac{1}{-\frac{3}{2} v_{dg}} \quad (3.38)$$

$$e_{df} = \omega_s L_f i_{dg} \quad (3.39)$$

It is worthy to mention that for this research the reactive power reference was selected to be zero, reducing in this way the currents flowing through the back to back converter to its minimum possible value.

Finally, the angular position of the grid voltage vector ( $\theta_g$ ), necessary for the alignment of the rotating reference frame, is calculated making use of a phase locked loop (PLL) (ABAD et al., 2011). The block diagram of this closed loop structure is presented in Figure 3.15. In this, the  $abc$  grid voltage is referred to a  $dq$  rotating reference frame, using the angular position calculated by itself. The quadrature component of this voltage is introduced in a PI controller, which modifies the estimated angular speed until this quadrature voltage becomes zero, which represents that the grid voltage space vector is aligned with the rotating reference frame direct axis.



Source: (ABAD et al., 2011)

### 3.7. RSC CONTROL SYSTEM

One of the main requirements for the proper operation of a DFIG is an effective control of the power flux through the stator. As in the case of the GSC, it is possible to achieve a decoupled control of the stator active and reactive power fluxes making use of the vector control theory. In order to explain this system, it is necessary to transform the  $\alpha\beta$  dynamic model of the machine present in Section 2.2.2 into a model referred to a synchronous rotating reference ( $dq$  model).

### 3.7.1. DFIM dynamic $dq$ model

As explained in Section 2.2.1, by multiplying the machine voltage equations eq.(2.62) and eq.(2.63) by  $e^{-j\theta_s}$  and  $e^{-j\theta_r}$  respectively, we obtain the machine voltage equations referred to a synchronous rotating reference frame:

$$\vec{v}_s^a = R_s \vec{i}_s^a + \frac{d\vec{\psi}_s^a}{dt} + j\omega_s \vec{\psi}_s^a \quad (3.40)$$

$$\vec{v}_r^a = R_r \vec{i}_r^a + \frac{d\vec{\psi}_r^a}{dt} + j\omega_r \vec{\psi}_r^a \quad (3.41)$$

The superscript  $a$  indicates that the space vectors are referred to a synchronous reference frame. Applying the same procedure to the flux expressions presented in eq.(2.64) and eq.(2.65) we obtain:

$$\vec{\psi}_s^a = L_s \vec{i}_s^a + L_m \vec{i}_r^a \quad (3.42)$$

$$\vec{\psi}_r^a = L_m \vec{i}_s^a + L_r \vec{i}_r^a \quad (3.43)$$

From these equations is possible to obtain the equivalent circuit model in the synchronous reference frame, which is presented in Figure 3.16. In addition, the power relations can be established in a similar way than for the  $\alpha\beta$  model.

$$P_s = \frac{3}{2} \text{Re}\{\vec{v}_s \cdot \vec{i}_s^*\} = \frac{3}{2} (v_{ds} i_{ds} + v_{qs} i_{qs}) \quad (3.44)$$

$$P_r = \frac{3}{2} \text{Re}\{\vec{v}_r \cdot \vec{i}_r^*\} = \frac{3}{2} (v_{dr} i_{dr} + v_{qr} i_{qr}) \quad (3.45)$$

$$Q_s = \frac{3}{2} \text{Im}\{\vec{v}_s \cdot \vec{i}_s^*\} = \frac{3}{2} (v_{qs} i_{ds} - v_{ds} i_{qs}) \quad (3.46)$$

$$Q_r = \frac{3}{2} \text{Im}\{\vec{v}_r \cdot \vec{i}_r^*\} = \frac{3}{2} (v_{qr} i_{dr} - v_{dr} i_{qr}) \quad (3.47)$$

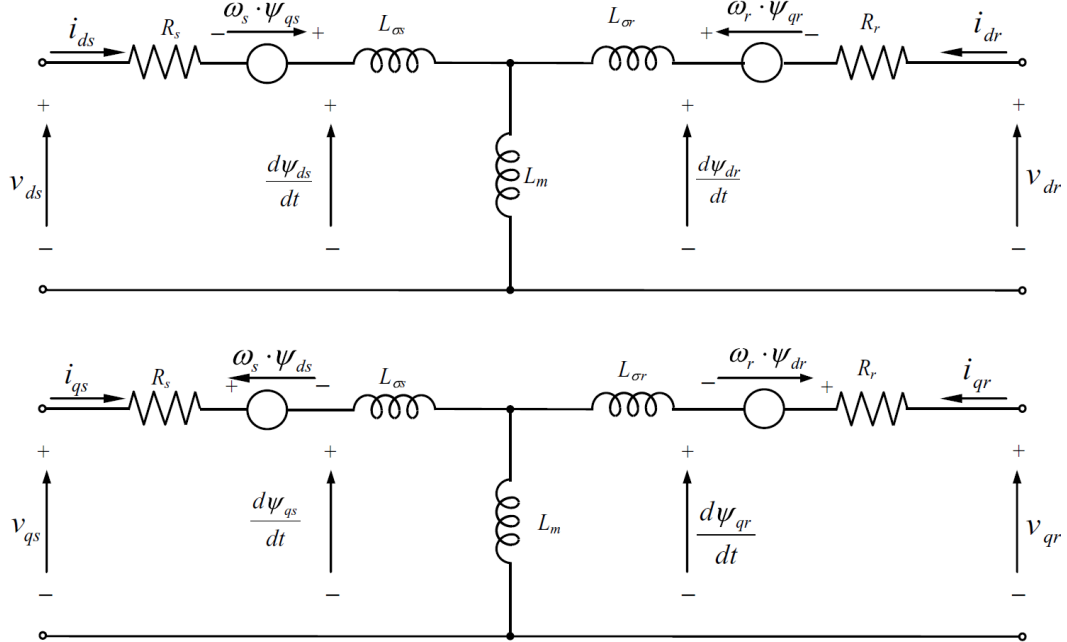
### 3.7.2. Alignment of the rotating reference frame

In order to achieve the desired decoupled control of the active and reactive power flows, it is necessary to align the direct axis of the rotating reference frame with the stator flux space vector. By doing so, the relations between the stator flux dq components and the stator and rotor currents can be written as:

$$\psi_s = L_s i_{ds} + L_m i_{dr} \quad (3.48)$$

$$0 = L_s i_{ds} + L_m i_{qr} \quad (3.49)$$

Figure 3.16 -DFIG equivalent circuit model in the synchronous reference frame



Source: (ABAD et al., 2011)

Rearranging these equations, the relation between the stator and rotor currents can be found:

$$i_{ds} = \frac{\psi_s}{L_s} - \frac{L_m}{L_s} i_{dr} \quad (3.50)$$

$$i_{qs} = -\frac{L_m}{L_s} i_{qr} \quad (3.51)$$

Considering that in steady state the stator voltage is sinusoidal and balanced, its direct and quadrature components in the synchronous rotating reference frame are constant in time. Thus, assuming the voltage drop in the stator resistance negligible, the expansion of eq.(3.40) can be written as:

$$V_{ds} = 0 \quad (3.52)$$

$$V_{qs} = \hat{V}_g \approx \omega_s \psi_s \quad (3.53)$$

It can be seen from the last equations that the alignment of the direct axis with the stator flux vector forces the stator voltage to align with the quadrature axis. Introducing this fact into equations (3.44) and (3.46) we have a simplification of the stator power relations:

$$P_s = \frac{3}{2} v_{qs} i_{qs} \quad (3.54)$$

$$Q_s = \frac{3}{2} v_{qs} i_{ds} \quad (3.55)$$

Combining these equations with equations (3.50) and (3.51) we obtain:

$$P_s = -\frac{3}{2} \hat{V}_g \frac{L_m}{L_s} i_{dr} \quad (3.56)$$

$$Q_s = \frac{3}{2} \hat{V}_g \frac{\psi_s}{L_s} - \frac{3}{2} \hat{V}_g \frac{L_m}{L_s} i_{dr} = \frac{3}{2} \frac{\hat{V}_g^2}{\omega_s L_s} - \frac{3}{2} \hat{V}_g \frac{L_m}{L_s} i_{dr} \quad (3.57)$$

Thus, when the rotating reference frame is aligned with the stator flux, the active and reactive stator powers are completely decoupled and can be controlled modifying the quadrature and direct rotor currents respectively. Using equations (3.56) and (3.57) we can obtain the rotor current references from the active and reactive power references as shown in Figure 3.17.

### 3.7.3. Stator flux orientated vector control

As in the case of the GSC control system, it is necessary to find the relation between the rotor current and voltage, in order establish the voltage references feeding the PWM system. Applying the stator flux orientation to the circuitual representation of Figure 3.16 and neglecting the effect of the stator resistance we obtain the equivalent circuit of Figure 3.18.

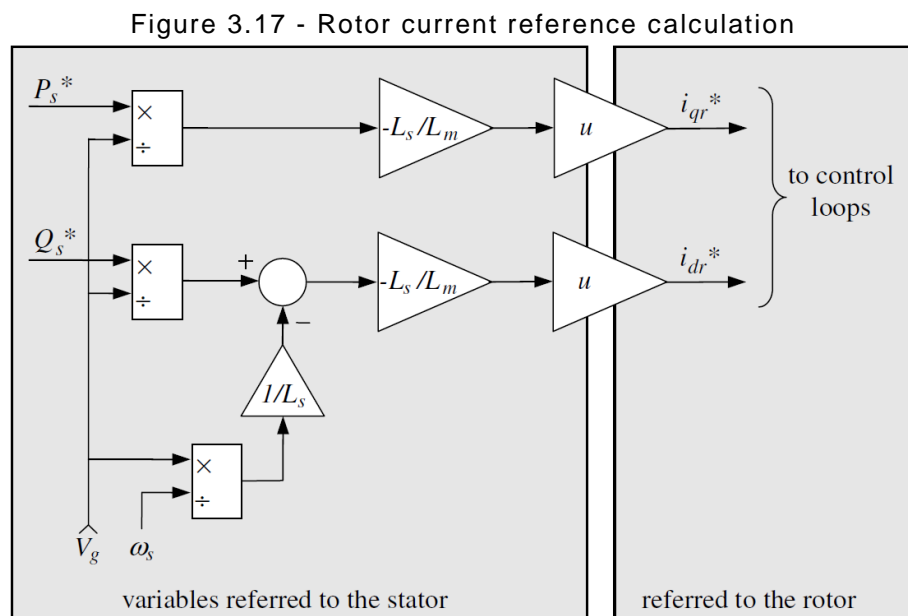
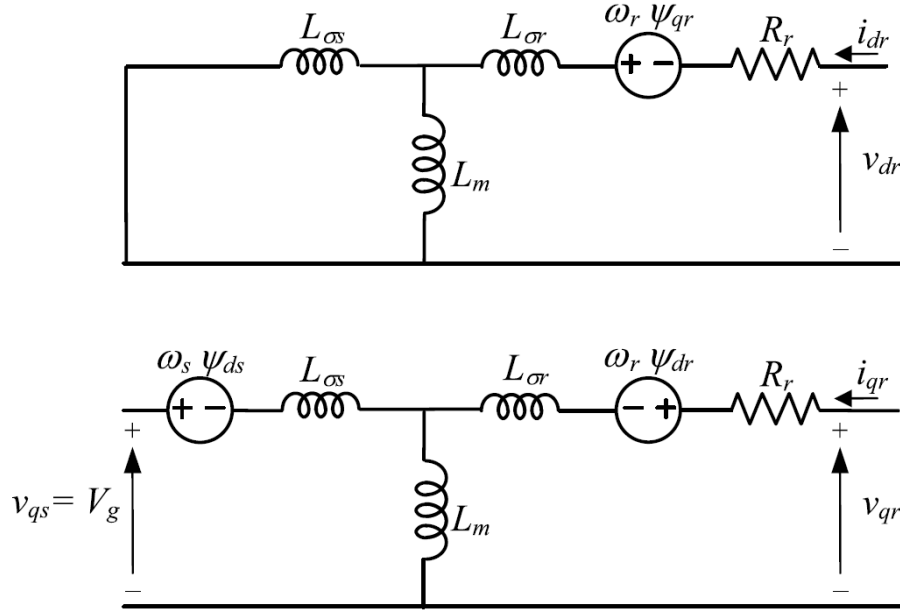


Figure 3.18 - DFIG  $dq$  equivalent circuit using the stator flux orientation

Source: (ABAD et al., 2011)

The voltage at the rotor terminals can be written as:

$$v_{dr} = R_r i_{dr} - \omega_r \psi_{qr} + \frac{d}{dt} \psi_{dr} \quad (3.56)$$

$$v_{qr} = R_r i_{qr} - \omega_r \psi_{dr} + \frac{d}{dt} \psi_{qr} \quad (3.57)$$

Accordingly, the relation between the flux and the rotor current can be expressed as:

$$\psi_{dr} = \sigma L_r i_{dr} + \frac{L_m}{L_s} \psi_{ds} \quad (3.58)$$

$$\psi_{qr} = \sigma L_r i_{qr} \quad (3.59)$$

Where,

$$\sigma L_r = L_r - \frac{L_m^2}{L_s}$$

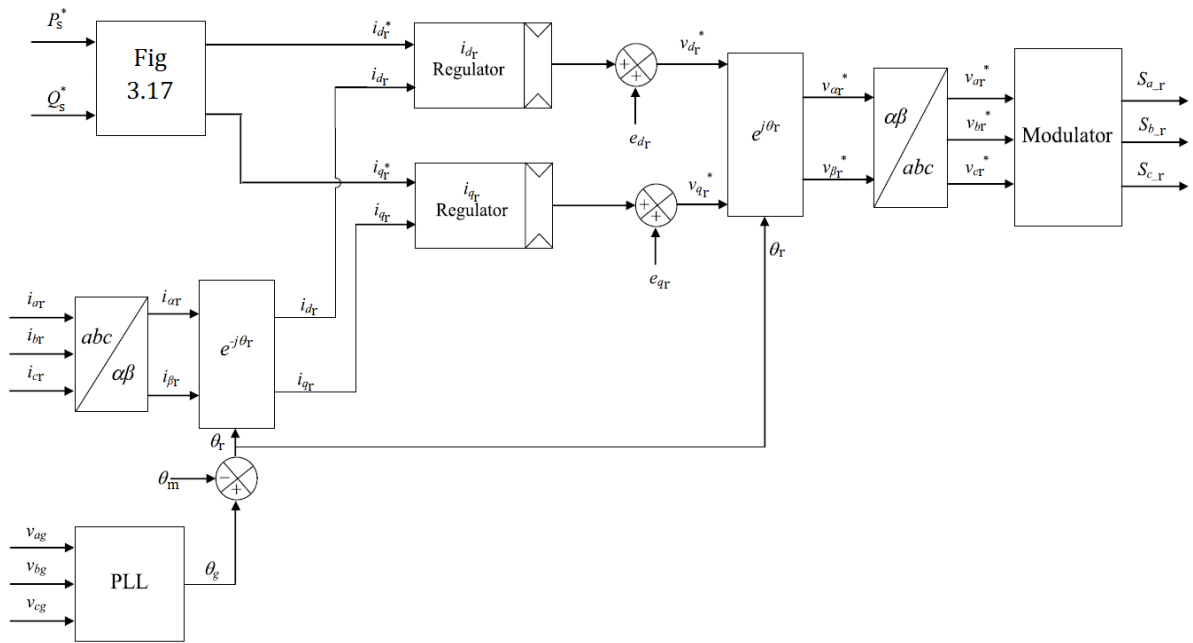
This last term  $\sigma L_r$  is known as the transitory inductance of the rotor. Finally, the voltage expressions in terms of the rotor currents are presented as the result of the combination of equations (3.56) and (3.57) with equations (3.58) and (3.59), resulting in:

$$v_{dr} = R_r i_{dr} - \omega_r \sigma L_r i_{qr} + \sigma L_r \frac{d}{dt} i_{dr} + \frac{L_m}{L_s} \frac{d}{dt} \psi_{ds} \quad (3.56)$$

$$v_{qr} = R_r i_{qr} - \omega_r \sigma L_r i_{dr} + \sigma L_r \frac{d}{dt} i_{qr} + \omega_r \frac{L_m}{L_s} \psi_{ds} \quad (3.57)$$

During steady state the direct component of the stator flux can be assumed to be constant. For this reason, the last term of eq.(3.56) is considered null for the control system implementation. In turn, the last term of eq.(3.57) is seen by the control system as an external constant perturbation, since it only depends on the stator flux. A simple PI controller is able to compensate such external input, making unnecessary its inclusion in the control loop. Finally, the terms  $\omega_r \sigma L_r i_{qr}$  and  $\omega_r \sigma L_r i_{dr}$ , commonly known as cross terms, should be considered and compensated by the control system since they can act as a significant perturbation during transients. All these considerations lead to the control structure depicted in Figure 3.19.

Figure 3.19 - Grid side converter control system



In this control system, the cross terms are introduced as feed forward terms, right at the output of the current regulators:

$$e_{dr} = -\omega_r \sigma L_r i_{qr} \quad (3.58)$$

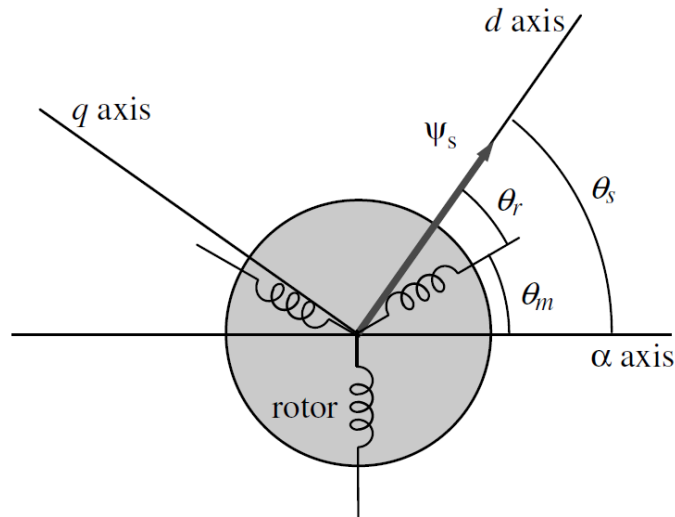
$$e_{qr} = -\omega_r \sigma L_r i_{dr} \quad (3.59)$$

The proper calculation of the angle used for the reference frame transformation is a crucial step for the effective operation of the control system. As explained in (ABAD et al., 2011), a reliable alternative is to determine the angle between the direct axis

and the rotor phases ( $\theta_r$ ) as the difference between the direct axis angular position ( $\theta_g$ ) and the angular position of the rotor ( $\theta_m$ ) (see Figure 3.20).

Bearing in mind that the stator flux vector must be aligned with the direct axis, and that the stator resistance effect was assumed to be negligible,  $\theta_g$  is calculated by a PLL system as shown in Figure 3.21. This system aligns the grid voltage vector with the quadrature axis, and then establishes the position of the stator flux as being  $90^\circ$  behind this voltage (aligned with the direct axis). This calculation methodology is known as grid voltage-orientation and is graphically presented in Figure 3.22.

Figure 3.20 - Stator flux calculation principle



Source: (ABAD et al., 2011)

Figure 3.21 - PLL configuration for the stator flux angle calculation

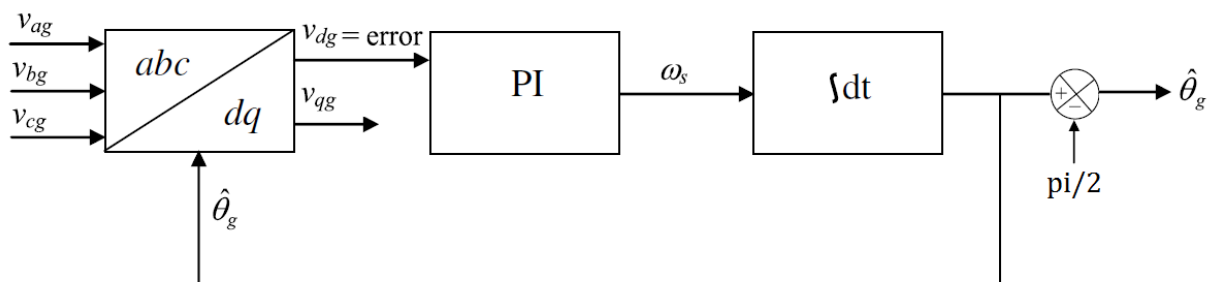
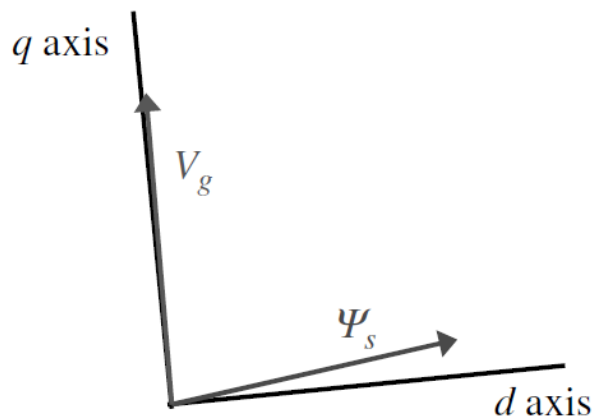
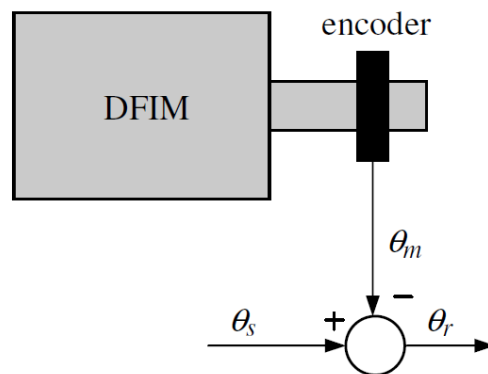


Figure 3.22 - Grid voltage-orientation principle



Even with the unavoidable error created by the assumption of no stator resistance influence, this approximation is satisfactory for the control of the machine in steady state and transient conditions, as will be shown ahead. With regard to the measurement of the rotor angular position, the most common solution is the use of an encoder coupled with the rotor as shown in Figure 3.23.

Figure 3.23 - rotor position measurement



Source: (ABAD et al., 2011)

After introducing the control schemes necessary for the proper operation of the DFIG, and the electronic components required for their implementation, it is possible to assemble the complete electromagnetic model of the generator. This is achieved by joining the sub-models developed in this chapter with the dynamic model of the generator introduced in chapter 2. In the next chapter the simulation tool selected for the implementation of the model will be introduced.

## 4. METHODOLOGY AND ASSUMPTIONS

After developing the DFIG model in the last two chapters, it is time to introduce the computational tool used for its implementation. Due to its proven effectiveness for the study of electromagnetic and electromechanical phenomena, its versatile libraries and its user-friendly interface, the power system simulation tool SimPowerSystems was selected for the simulations process. This program, developed by Mathworks in collaboration with Hydro-Québec of Montreal, is an extension of the dynamic systems simulation software MATLAB's Simulink. This allows a direct interaction with the programming interface of MATLAB, in order to perform parametric studies as the ones presented in this research. In the next sections, the solution procedure followed by the software will be shortly described, as well as the available solution methodologies. Finally, some simplifying assumptions regarding the electro-mechanic behavior of the generator will be introduced and justified.

### 4.1. SIMPOWERSYSTEMS SOLUTION METHODOLOGY

After constructing the system's block model in the graphic interface of Simulink, the specific simulation settings of each block are established and the electric and control parameters of the system are entered. After this pre-processing procedure, it is necessary to make the electric model compatible with the Simulink standard solving strategy. In order to achieve this, the next sequence is automatically followed:

- Sort the blocks, separating them into linear and nonlinear.
- Extract the block parameters and evaluate the network topology.
- Compute the state-space model of the linear part of the circuit.
- Perform the initial conditions computation.
- Build the Simulink's model equations system of and store it.

The system model is now ready to be solved. The solving procedure is composed by the next steps:

- Transient initialization: All the dynamic variables (variables with time derivatives in the equations) are fixed and the system is solved for the

algebraic variables (variables without time derivatives in the equations) and derivatives of the dynamic equations. The goal of this step is to generate a consistent set of initial conditions for the next phase.

- Transient solve: The continuous differential equations are integrated in time in order to compute all the variables as a function of time. This process continues until the instant when the solver encounters a discontinuity, time when it returns to the transient initialization in order to obtain an appropriate set of initial conditions, which allow a discontinuity-free solving process.

#### 4.2. SIMPOWERSYSTEMS SOLUTION METHODS

It was previously mentioned that there are alternatives to the continuous solving approach presented in the last section. Being more specific, there are three solution methods offered by the software:

- Continuous solution method using variable-step solvers.
- Discretization for solution at fixed time steps.
- Phasor solution method using variable step solvers.

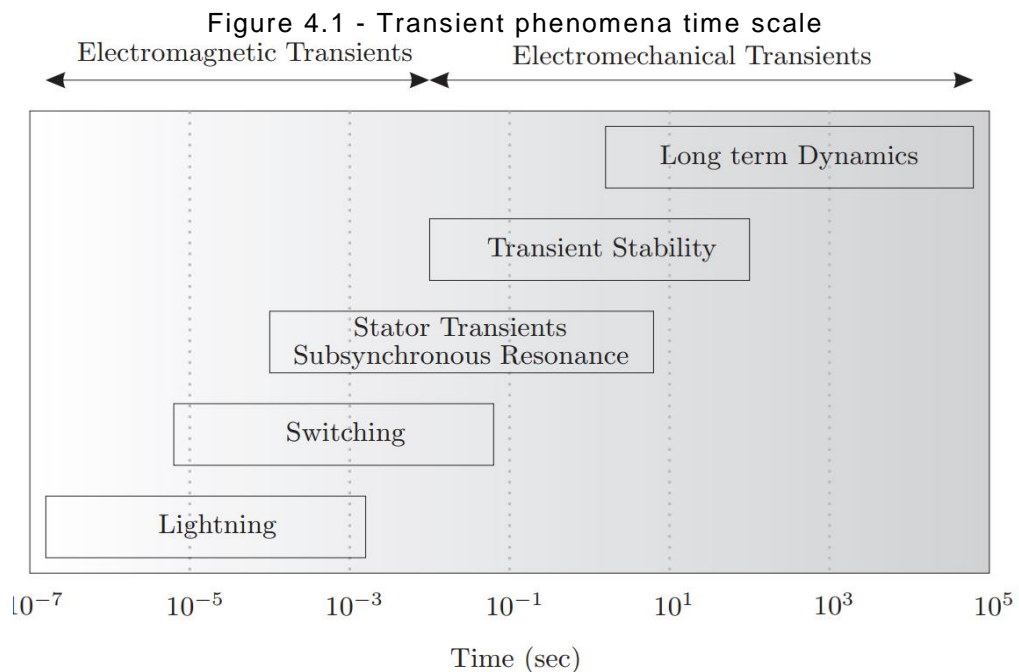
According to the information provided by the software developer, the use of the continuous solution method is recommended for small size systems, due to its higher accuracy and reduced solving time when compared with the discretization based solution method. This superior solving speed is justified by the reduced number of steps that the variable-step solver requires for achieving an accuracy level comparable to the one obtained using fixed-step methods. However, when the system contains more than 50 electrical states or more than 25 switching devices, the use of the continuous solution method represents long solution times due to its extreme accuracy. Thus, for large systems the developers recommend the use of fixed-step solvers. The use of the third solving alternative, known as phasor solution method, is highly recommended when it is desired to know only the behavior of the amplitude and phase of all the voltages and currents in the system. This method is especially useful for transient stability studies of networks involving large motor and generators.

Due to the small size of the implemented DFIG model, and the high accuracy required for the study of fast transient electromagnetic phenomena, it was decided

to use the continuous solution method for the simulations presented in this document.

### 4.3. ASSUMPTIONS

In order to facilitate the simulation process, some simplifying assumptions can be made without incurring in considerable errors. The first of them is that during the period of study (some milliseconds after the voltage dip beginning), the rotating speed of the rotor remains constant. Such assumption, shared by (QUANG; DITTRICH, 2008), is justified by the slower behavior of machine's electromechanical transients, when compared with the electromagnetic transient events of interest. This is illustrated in Figure 5.1. It can be seen there that the electromechanical transients range from 100ms to some hours, while the time scope of our research is, in the most critical scenario, slightly superior to 100ms. This time scope is defined by the grid codes as the limit for the reactive current injection to begin, after the dip start (SOURKOUNIS; TOUROU, 2013).



Source: (ONG, 1998)

The second assumption is related with the voltage dip time characteristics. It was assume for this research that the voltage drops abruptly at the beginning of the dip, going from the pre-fault voltage to the fault voltage instantaneously. It is clear for us

that such an abrupt voltage drop is not physically possible in real electric networks. However, the current grid codes require the voltage to drop in maximum 1ms, which can be considered to be instantaneous, since the difference in the induced rotor voltage for the two drop times is less than 1% (ABAD et al., 2011). Additionally, an instantaneous voltage drop is the worst possible case scenario since any other drop time would result in a smaller induced rotor voltage.

## 5. RSC PROTECTION STRATEGIES

In this chapter, the five selected protection strategies are introduced and described in detail. In order to facilitate the understanding of their operation, it is assumed that the RSC is able to supply any voltage magnitude demanded by the strategies during its activation period. This, as will be seen in chapter 6, is not a feasible alternative since one of the main characteristics of the DFIG is precisely the reduced size of its power converter.

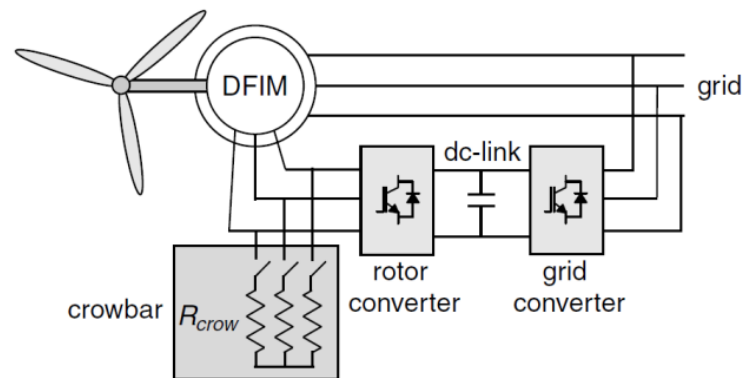
### 5.1. CROWBAR CIRCUIT (CB)

When a voltage dip takes place, a non-rotating natural component of the stator flux appears, decaying with the time constant of the stator. This static component induces in the rotor an emf that may force the circulation of large currents across the rotor circuit, putting on risk the rotor side converter integrity. The circulation of such currents is conditioned to the saturation of the RSC, which occurs when the emf is large enough to establish at the rotor terminals a voltage higher than the maximum output voltage of the RSC.

The crowbar circuit is a protection strategy widely used among the DFIG manufacturers, intended to keep the voltage at the rotor terminals under a predefined safe value while an emf, large enough to cause the saturation of the RSC, is induced in the rotor. In case of detecting an anomalous situation (overcurrent in the rotor, overvoltage on the DC-link or low stator voltage), the crowbar strategy proposes the connection of a group of resistances between the rotor terminals (see Figure 5.1) concurrently with the deactivation of the RSC. The introduction of the resistances establishes a voltage divider, calibrated to keep the voltage amplitude under the converter saturation point, until the induced emf has reached a value low enough to allow a safe reactivation of the RSC.

In Figure 5.2 is presented an equivalent circuit of the system when the crowbar is activated. It is evident from it that the resistances value not only influences the voltage value at the terminals, but also the amplitude of the current that circulates across the rotor.

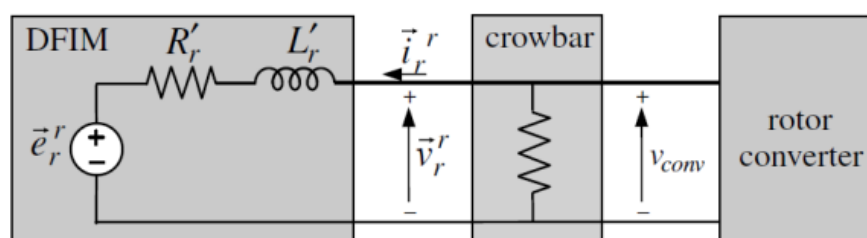
Figure 5.1 - DFIG equipped with crowbar



Source: (ABAD et al., 2011)

If the resistance value is low, the current will have a high value, requiring the selection of an oversized crowbar switch which could withstand such current. This high current will also accelerate considerably the decaying of the stator natural flux and, consequently, of the induced emf. In the case of a high resistance value, the rotor current will have a lower value, diminishing the stress that the electrical components will be exposed to. However, the voltage at the RSC terminals may rise up to a value higher than the pre-established maximum limit, leaving the converter unprotected. This low value current does not accelerate the decay of the induced emf, which would then decay with a time constant very close to that of the stator.

Figure 5.2 - Rotor equivalent circuit including the Crowbar system



Source: (ABAD et al., 2011)

The simulation of a 90% three phase voltage dip, for three values of crowbar resistance, is presented in Figure 5.3. In order to illustrate the phenomena in the clearest way, the crowbar system activation is executed simultaneously with the dip start, and remains activated during the whole simulation. The stator voltage is shown in Figure 5.3a, remaining at its nominal value until the introduction of the voltage dip at  $t=1$ s. In Figure 5.3b the voltage at the rotor terminals is presented.

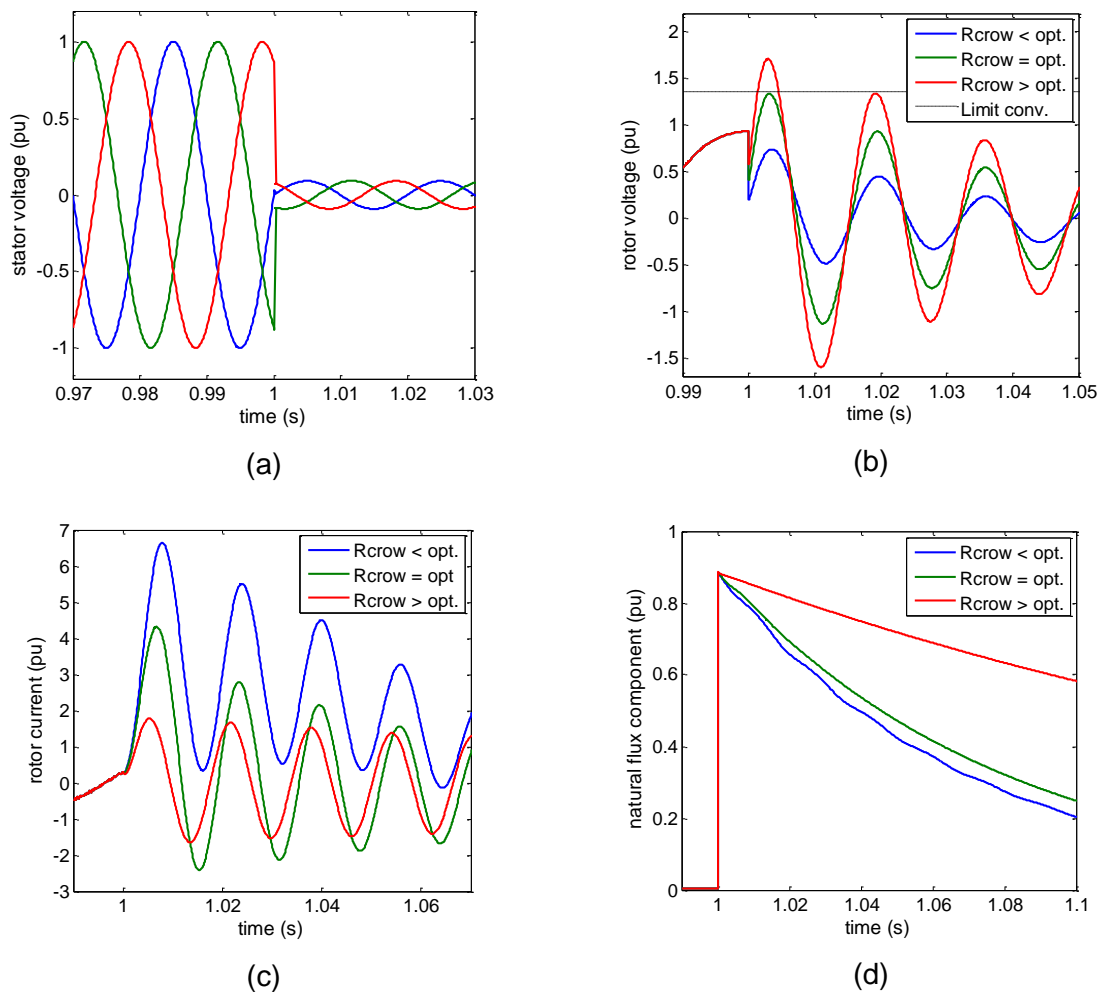
This figure confirms that a high value of resistance may leave the converter unprotected, allowing the voltage at its terminals to surpass the safe limit (represented in the figure by the dotted line) defined in (ABAD et al., 2011) as:

$$\hat{V}_r < \frac{V_{bus}}{\sqrt{3}} u \quad (5.1)$$

Where  $\hat{V}_r$  is the peak value of the rotor voltage,  $V_{bus}$  is the DC-link bus voltage, and  $u$  is the stator to rotor turn ratio.

In Figure 5.3c is presented the current circulating across the rotor circuit. It is evident that for the intermediate and low values of resistance, the current after the crowbar activation surpasses the nominal current value, rising up to approximately  $3pu$  at the beginning of the dip. As was mentioned before, this current raise is one of the consequences of protecting the converter through the use of this strategy, requiring the selection of oversized electrical components.

Figure 5.3 - 90% three phase voltage dip for three crowbar resistances: (a) stator voltages, (b) rotor voltage, (c) rotor current, (d) natural flux component.



The main drawback of using this protection strategy, is the loss of control over the power transference between the generator and the grid during its activation period. While the crowbar is active, the generator behaves as a squirrel cage machine with a slightly high rotor resistance, absorbing reactive power while generating or absorbing active power depending on its rotational speed (see Figure 2.5).

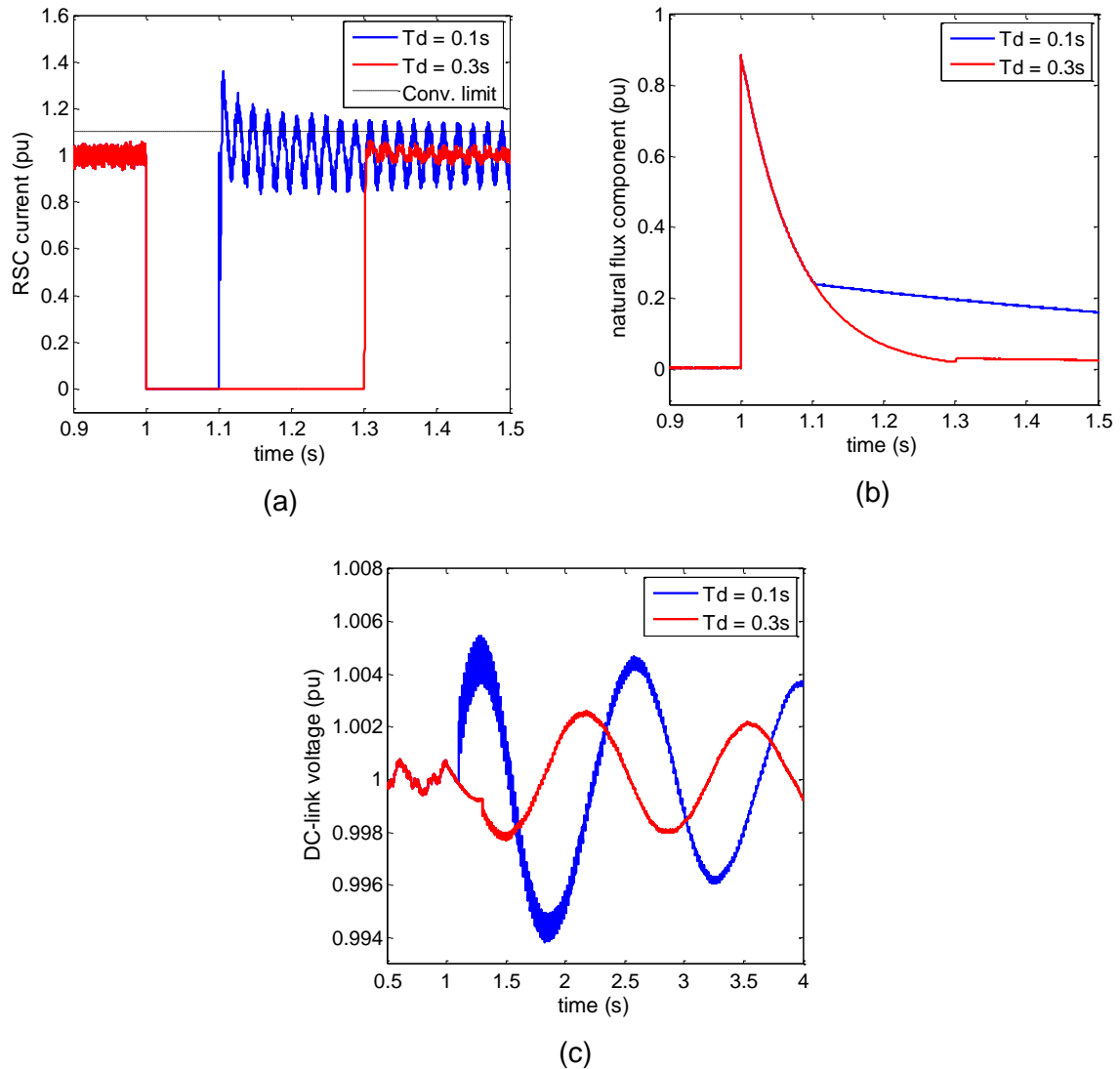
Since most of the gridcodes demand the generator to deliver reactive current some milliseconds after the fault beginning (SOURKOUNIS; TOUROU, 2013), a fast and safe reactivation of the RSC is mandatory. In order to achieve it, the natural flux must have reached a low adequate value, considering that a reconnection with a higher value of natural flux, could force the circulation of overcurrents across the converter. As mentioned before, the selection of a low crowbar resistance value accelerates the decay of the natural flux, reducing considerably the amount of time necessary to perform a safe reactivation of the converter. It is now convenient to study in detail the influence of the crowbar resistance value in the reactivation time of the RSC.

In Figure 5.4 a 90% three-phase voltage dip was once more simulated, using as crowbar resistance the intermediate resistance value presented in Figure 5.3, which was proven to keep the voltage at the rotor terminals under the pre-established maximum limit during the crowbar activation period. It is presented in Figure 5.4a the converter current space vector magnitude, before, during and after the activation of the crowbar system, for two activation times,  $T_d=0.1s$  and  $T_d=0.3s$ . When the activation time is greater than 0.3s, the current circulating across the converter does not surpass the maximum current limit, defined by the converter's manufacturer. This can be justified by the pronounced decay of the natural flux component (see Figure 5.4b), attaining a value of approximately 0.2T at the deactivation instant, which is small enough to keep the converter unsaturated. When the activation time is reduced to 0.1s, the value reached by the natural flux at the crowbar deactivation instant is considerably higher, inducing in the rotor an emf that effectively saturates the converter and, consequently, forces the appearance of currents in the rotor circuit that exceed the predefined maximum limit.

The activation time has also an influence on the DC-link voltage behavior. As can be seen in Figure 5.4c, the DC-link voltage oscillates around the reference value after the crowbar deactivation, reaching a maximum voltage of approximately 1.003pu for  $T_d=0.3s$  and 1.05pu for  $T_d=0.1s$ . It can be inferred from these results that a greater

reduction of the deactivation time could cause overvoltages in the DC-Link large enough to surpass its maximum value defined by the manufacturer.

Figure 5.4 - 90% three phase voltage dip for the optimum crowbar resistance value: (a) RSC current, (b) natural flux component, (c) DC-Link voltage.



It can be concluded from the previous results that the crowbar resistance value has to be selected not only to avoid the saturation of the converter while the crowbar system is activated, but also when the RSC is reactivated. Having as an objective the reconnection of the converter 100ms after the beginning of the fault, a time period that meets the criteria requested by most of the European current gridcodes (SOURKOUNIS; TOUROU, 2013) for a 90% three phase voltage dip, several simulations were performed looking for the identification of the adequate resistance value in order to warrant the converter protection.

In Figure 5.5 are presented the simulation results for two crowbar resistance values, the same resistance value used in Figure 5.4 and the maximum resistance value that achieved to avoid the saturation of the converter at its reconnection. It can be noticed in Figure 5.5a that the selection of a lower crowbar resistance value increases the decay rate of the stator natural flux component, reducing the emf induced in the rotor at the reconnection of the RSC, and avoiding the saturation of the converter as can be seen in Figure S5b. In Figure 5.5c is presented the effect on the DC-link voltage. The reduction of the resistance value diminishes the oscillation of the voltage, going from a maximum of  $1.01pu$  for the first case, to a maximum of  $1.02pu$  for the second case.

## 5.2. FEEDBACK OF THE STATOR CURRENTS AS RSC REFERENCES (SCI)

Having in mind the protection of the RSC, this strategy intends to keep the currents induced in the rotor, during a voltage dip, under the limit informed by the converter supplier, without the introduction of additional hardware or the deactivation of the RSC. This is achieved using the measured stator current (decomposed in its direct and quadrature components) as the current reference for the RSC, in order to induce in the stator a current with the same shape of that appears during the dip, but in counter phase (LIMA et al., 2010). This induced current will cause a reduction of the net stator current, and, consequently, of the currents circulating across the rotor.

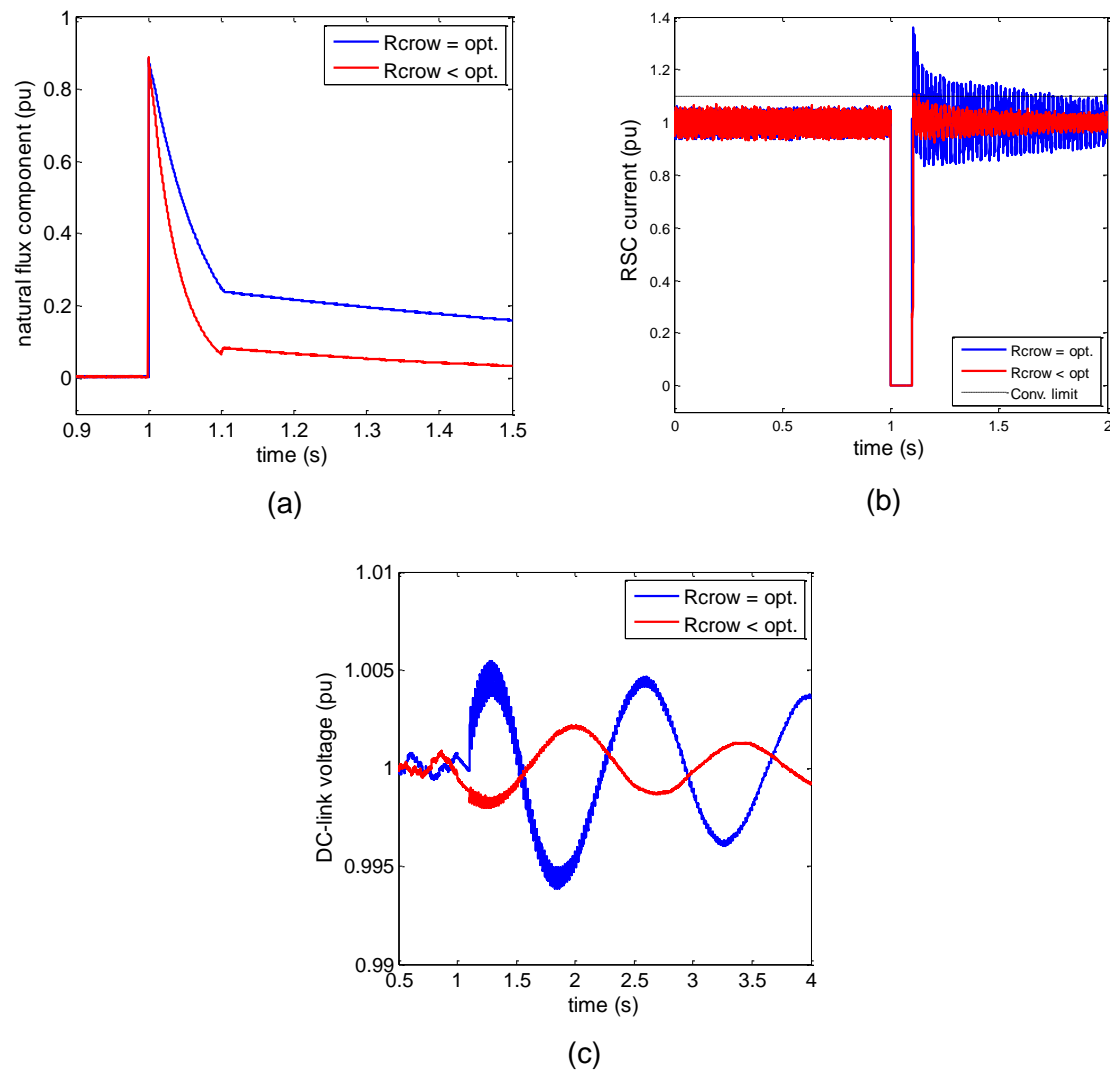
In Figure 5.6 is presented a layout of the proposed control strategy. While the stator voltage is in steady state, the references followed by the direct and quadrature axis control loops are the reactive and active power references respectively, as indicated by the initial position of the switch in the figure. When a significative reduction of the stator voltage is measured, the references are switched to the following values:

$$i_{dr}^* = i_{ds} \quad (5.2)$$

$$i_{qr}^* = i_{qs} \quad (5.3)$$

The introduction of these new references effectively reduces the net rotor current during the strategy activation period, as will be shown in the subsequent simulations. Nevertheless, the decay of the stator natural flux component is very slow, delaying considerably the injection of reactive current demanded by the grid codes (SOURKOUNIS; TOUROU, 2013).

Figure 5.5 - 90% three phase voltage dip for two crowbar resistances: (a) natural flux component, (b) RSC current, (c) DC-Link voltage.



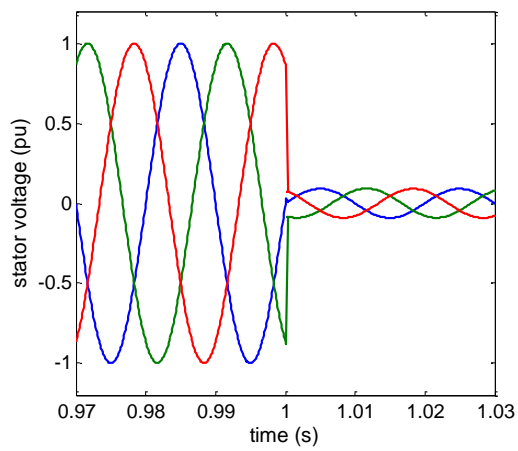
In order to prove the effectiveness of this strategy, a 90% three phase voltage dip was simulated (see Figure 5.7a), keeping the strategy activated for 100ms after the beginning of the fault. In Figure 5.7b is presented the rotor current vector amplitude. It is possible to notice in this figure that the converter's maximum limit is not surpassed during the duty period of the strategy.

However, when the strategy is deactivated, the current reaches a value 20% higher than the limit, and keeps surpassing it periodically while oscillating around the rated current value.

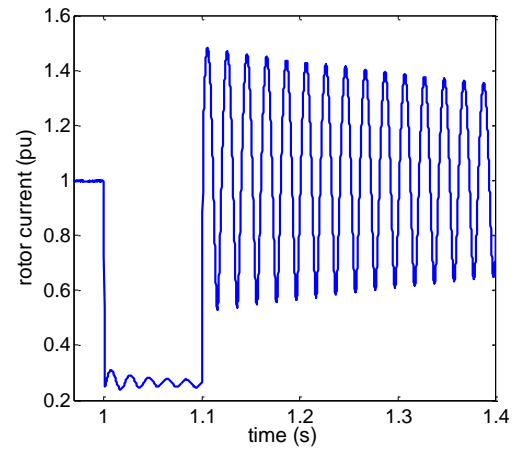
This undesired behavior is justified by the slow decay of the stator natural flux component during the duty period (see Figure 5.7c), which leaves the RSC facing an induced emf high enough to saturate it after the strategy deactivation.



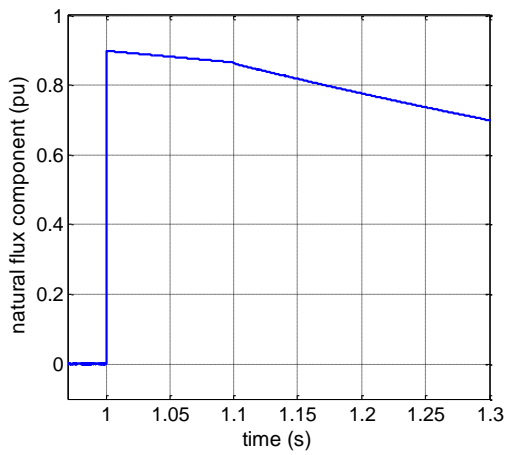
Figure 5.7 - 90% three phase voltage dip with the strategy activated during 100ms: (a) stator voltage, (b) rotor current, (c) natural flux component, (d) RSC voltage, (e) active current contribution, (f) reactive current contribution.



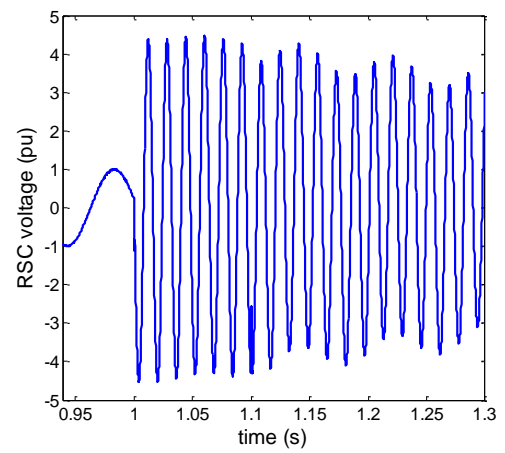
(a)



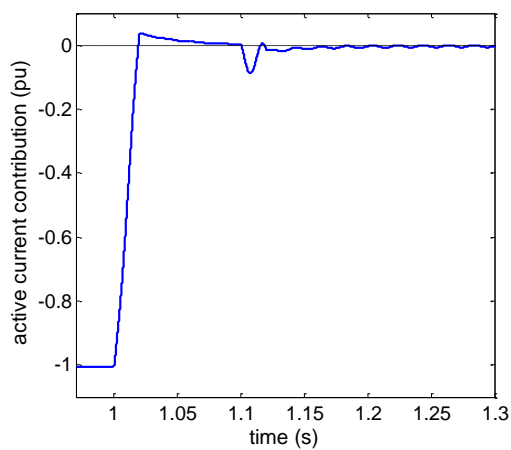
(b)



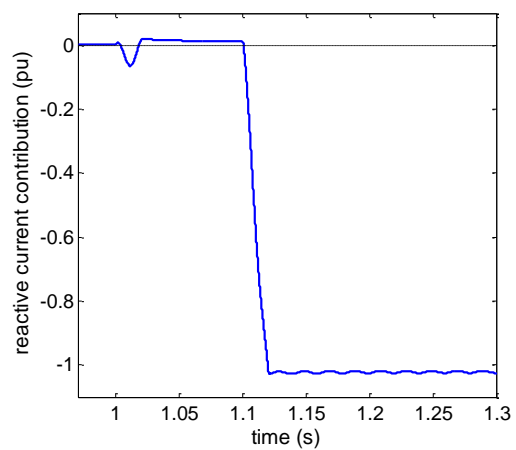
(c)



(d)



(e)



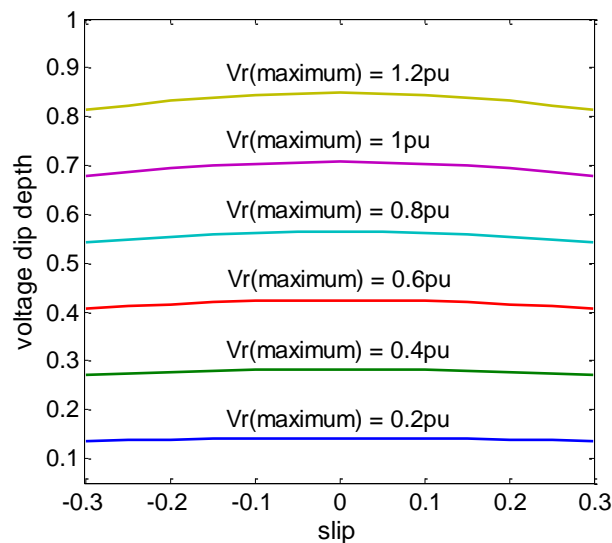
(f)

Through the addition of these two voltage components, the maximum amplitude of the rotor voltage vector is obtained:

$$V_{r(\text{maximum})} \cong \sqrt{2}\sqrt{1+s^2}D \quad (5.6)$$

In Figure 5.8, a graph of  $D$  in function of  $s$  for several values of  $V_{r(\text{maximum})}$  is presented.

Figure 5.8 - Rotor voltage maximum value



From this figure it can be inferred that, in order to effectively protect the RSC, its voltage rate must be of the same order of magnitude than that of the stator. Particularly, it can be seen that for the sake of protecting the converter against dips with a magnitude greater than 70%, the RSC must generate a voltage greater than the nominal stator voltage, which would require an oversized back to back converter.

Six different scenarios were simulated to validate the maximum rotor voltage predictions obtained from eq.(5.6). The results are presented in Table 5.1. When the machine is in hypersynchronism ( $s < 0$ ), the difference between the measured and the calculated voltage decreases with the increment of the dip depth, resulting in a difference of less than 12% for depths greater than 90%. In the case of subsynchronism ( $s > 0$ ), the differences are significantly greater than the ones obtained in hypersynchronism for the same dip depths, reaching a value greater than 32% for a 90% dip. This marked discrepancy can be justified by the fact that in case of sub-synchronism, the stator flux natural component reaches a peak value lower than in the case of hypersynchronism, inducing in the rotor a smaller emf, which

results in a lower rotor voltage peak value. This is not taken into account in the analytical development of eq.(6), which suggests no difference between working in sub or hyper synchronism.

It can be concluded that eq.(5.6) provides a coarse valid approximation in case of hypersynchronism, which can be helpful to perform a fast evaluation of the feasibility of this solution. If the target is the dimension of the converter, a detailed simulation is necessary since the divergence between the calculated and simulated values, resulted to be considerable. In case of subsynchronism, the use of eq.(5.6) returns values significantly distant from those obtained through the simulation. For that reason, the use of this equation under such conditions is not recommended.

Table 5.1 - Peak rotor voltage obtained from simulation

s	Dip depth (%)	Vrotor max computed (V)	Vrotor max Measured (V)	Difference (%)	R fault
-0.25	50	288	368	21.7	1e-3
-0.25	65	385	460	16.4	0.5e-3
-0.25	90	525	600	12.5	1e-4
0.25	50	288	212	26.3	1e-3
0.25	65	385	268	30.2	0.5e-3
0.25	90	525	354	32.5	1e-4

### 5.3. DEMAGNETIZING CURRENT INJECTION (DC)

The demagnetizing current technique proposes the injection of a rotor current, proportional and in anti-phase to the stator natural flux component, during the voltage dip (LÓPEZ et al., 2008). This is done in order to accelerate the natural flux damping, which reduces the *emf* induced in the rotor, and, as a consequence, avoids the saturation of the converter. A similar technique is commonly applied to brushless electrical drives(CHALMERS; MUSABA; GOSDEN, 1996), with the difference that in this case only the natural flux (in the case of a symmetric voltage dip) is reduced, since the positive flux does not induce in the rotor an *emf* capable of saturate the converter.

Assuming that neither the materials nor the converter saturate, the DFIG system can be considered linear. Thereby, from eq.(2.62) and eq.(2.64), a non-homogeneous linear differential equation that describes the stator flux behavior can be obtained:

$$\frac{d}{dt} \vec{\psi}_s^s = \vec{V}_s^s - \frac{R_s}{L_s} \vec{\psi}_s^s + \frac{R_s L_m}{L_s} \vec{I}_r^s \quad (5.7)$$

The solution to eq.(5.7), in the case of a three phase partial voltage dip, can be written as the sum of a homogenous and a particular solution. The particular solution represents the steady state flux, also known as the forced flux, which depends on the steady state stator voltage and rotor current as shown in eq.(5.8):

$$\vec{\psi}_{sf}^s = \sqrt{2} \frac{1}{j\omega_s + L_s/R_s} \left( V_{s1} + \frac{L_m}{j\omega_s L_s} I_{r1} \right) e^{j\omega_s t} \quad (5.8)$$

The homogeneous solution, which represents the natural flux that appears after the beginning of the voltage dip, solves eq.(5.9), if the forced stator voltage is assumed to be null during the dip:

$$\frac{d}{dt} \vec{\psi}_{sn}^s = -\frac{R_s}{L_s} \vec{\psi}_{sn}^s + \frac{R_s L_m}{L_s} \vec{I}_r^s \quad (5.9)$$

If the demagnetizing current criterion is applied ( $\vec{I}_{rn} = -K_d \cdot \vec{\psi}_{sn}^s$ ), eq.(5.10) becomes:

$$\frac{d}{dt} \vec{\psi}_{sn}^s = -\vec{\psi}_{sn}^s \frac{R_s}{L_s} (1 + K_d \cdot L_m) \quad (5.10)$$

The solution to eq.(5.11) can be expressed as an exponential function:

$$\vec{\psi}_{sn}^s = \psi_{n0} \cdot e^{-t/\tau_d} \quad (5.11)$$

With a time constant equal to:

$$\tau_d = \frac{L_s}{R_s(1 + K_d \cdot L_m)} \quad (5.12)$$

It can be seen from eq.(5.12) that, through the selection of an adequate value of  $K_d$ , the desired natural flux decay rate can be obtained. If a high value is selected, the decay acceleration can be high enough to allow an almost immediate nominal reactive current injection to the grid. However, this would represent an unbearable increment in the current that has to be supplied by the converter.

Due to the already mentioned linearity of the system, the superposition principle can be also applied to the rotor current reference calculation. Since the selection of the constant  $K_d$  is oriented to the reduction of the natural flux decay time, the converter would be working at its full capacity only for a very small amount of time, if, after the

beginning of the dip, it were exclusively following the demagnetizing current reference. Thus, after a very short period, an increasing steady state current reference can be added to the decreasing demagnetizing current reference, allowing a progressive raise of the reactive current injection, until reaching the amount demanded by the gridcodes. Having in mind that under no circumstances the converter current limit can be surpassed, a reference priority system was developed. The objective of this system is to limit the steady state current reference, ensuring that its magnitude never surpasses the difference between the converter limit and the demagnetizing current reference magnitude. In this way, it is ensured that the demagnetizing current reference will be always supplied. The steady state reference can be decomposed in its  $dq$  components. The direct axis component is in charge of controlling the reactive power transference trough the stator with the grid, and the quadrature component controls the active power transference. Given that, during a voltage dip, the injection of reactive current is highly desired in order to aid in the recovery of the voltage, the direct axis component is prioritized over the quadrature one by the reference priority system. In Figure 5.9 is presented a block diagram of the complete control system.

Assuming again the linearity of the system, the natural flux can be obtained subtracting the forced stator flux from the total stator flux. This last can be obtained from the rotor and stator currents, provided by the implemented machine model. The forced flux presented in eq.(5.8) can be substantially simplified, taking into account that the relation  $L_s/R_s$  is markedly smaller than  $\omega_s$ , what makes the former negligible. In addition, the value that multiplies the rotor current is approximately 3% of the value that multiplies the stator voltage (for a 2MW DFIG), reducing the effect of the rotor current considerably.

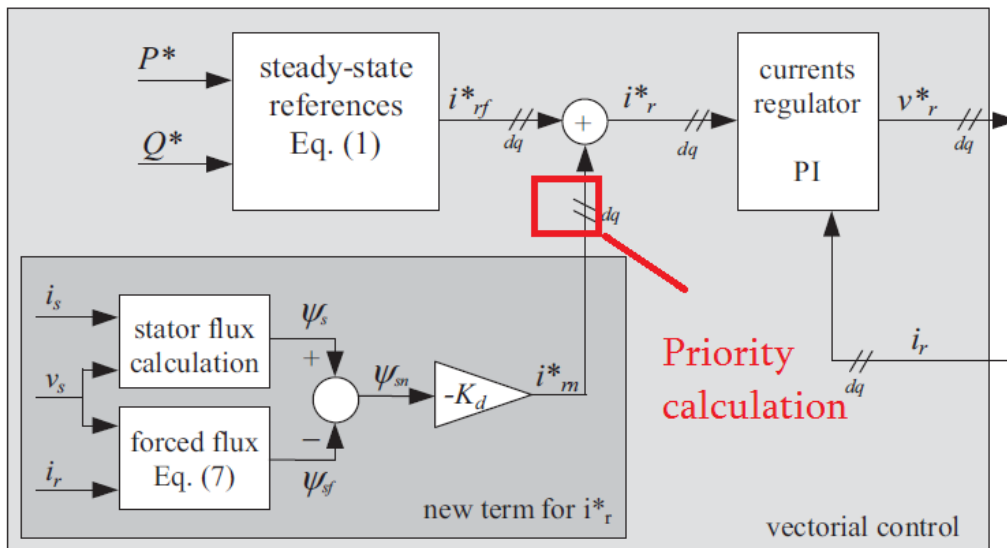
The final equation used for the calculation of the natural flux is:

$$\vec{\psi}_{sn}^s = \vec{\psi}_s^s - \vec{\psi}_{sf}^s = \vec{\psi}_s^s - \frac{V_{s1}}{j\omega_s} \quad (5.13)$$

The injection of a rotor current in counter-phase to the natural flux has a collateral effect on the rotor voltage natural component. If the proper value is selected for  $K_d$ , this voltage can even be cancelled as shown next.

The natural component of the rotor voltage, obtained in Section 2.3.1, is present in eq.(5.14). As can be seen, this voltage is highly dependent on the rotor current value.

Figure 5.9 - Rotor current references using DC strategy



Source: (LÓPEZ et al., 2008)

$$\vec{v}_{rn}^r = \frac{L_m}{L_s} (-j\omega_m \vec{\Psi}_{sn}^r) + \left[ R_r + \left( \frac{L_m}{L_s} \right)^2 R_s \right] \vec{i}_{rn}^r + \sigma L_r \frac{d}{dt} \vec{i}_{rn}^r \quad (5.14)$$

Since the natural component of the rotor current is steady with the stator, an observer standing in the rotor perceives it as rotating backwards with a speed equals to the rotor's one. Using this fact, and assuming that the decay rate of the natural flux is considerably low, eq.(5.14) can be written as follows:

$$\vec{v}_{rn}^r = \frac{L_m}{L_s} (-j\omega_m \vec{\Psi}_{sn}^r) + \left[ R_r + \left( \frac{L_m}{L_s} \right)^2 R_s \right] \vec{i}_{rn}^r - j\omega_m \sigma L_r \vec{i}_{rn}^r \quad (5.15)$$

Applying the demagnetizing current criteria to eq.(5.15) it is obtained:

$$\vec{v}_{rn}^r = \vec{\Psi}_{sn}^r \left[ \left( -j\omega_m \frac{L_m}{L_s} \right) - \left( R_r + \left( \frac{L_m}{L_s} \right)^2 R_s - j\omega_m \sigma L_r \right) K_d \right] \quad (5.16)$$

In order to null the rotor voltage natural component,  $K_d$  must be:

$$K_d = \frac{-j\omega_m \frac{L_m}{L_s}}{R_r + \left( \frac{L_m}{L_s} \right)^2 R_s - j\omega_m \sigma L_r} \quad (5.17)$$

Due to the small value that the rotor and stator resistances have, it is possible to simplify eq.(5.17) considerable, getting to the value of  $K_d$  suggested in (LÓPEZ et al., 2009).

$$K_d = \frac{L_m}{\sigma L_r L_s} \quad (5.18)$$

In order to assess the effect of using the criterion presented in eq.(5.18), a 90% three phase dip was simulated for three different values of  $K_d$ : The value obtained from eq.(12), half that value and 1,5 times that value. The results are presented in Figure 5.10. From Figure 5.10a is evident that the greater the value of  $K_d$ , the faster the natural flux decays. In Figure 5.10b is presented the rotor current vector magnitude for each one of these cases. As expected, there is a direct relation between the maximum current value and  $K_d$ , requiring the injection of six times the nominal rotor current for case 3 ( $K_d = 7500$ ). For the optimum value of  $K_d$  (case 2), the current required is equal to four times the nominal current. However, this current value can be controlled by limiting the rotor current reference value to the converter's limit. This will have a repercussion on the maximum rotor voltage that the converter has to supply to avoid saturation, as will be shown ahead. In Fig 5.10c is presented the rotor voltage in one of its phases. It can be seen in that figure that the optimum value of  $K_d$  has a superior performance, requiring a smaller value of voltage (just 1.5 times the rated value) and stabilizing faster than the other two cases. This certainly proves the importance of applying the criterion in order to avoid over sizing the converter when using this protection strategy.

#### 5.4. DEMAGNETIZING CURRENT VARIANTS

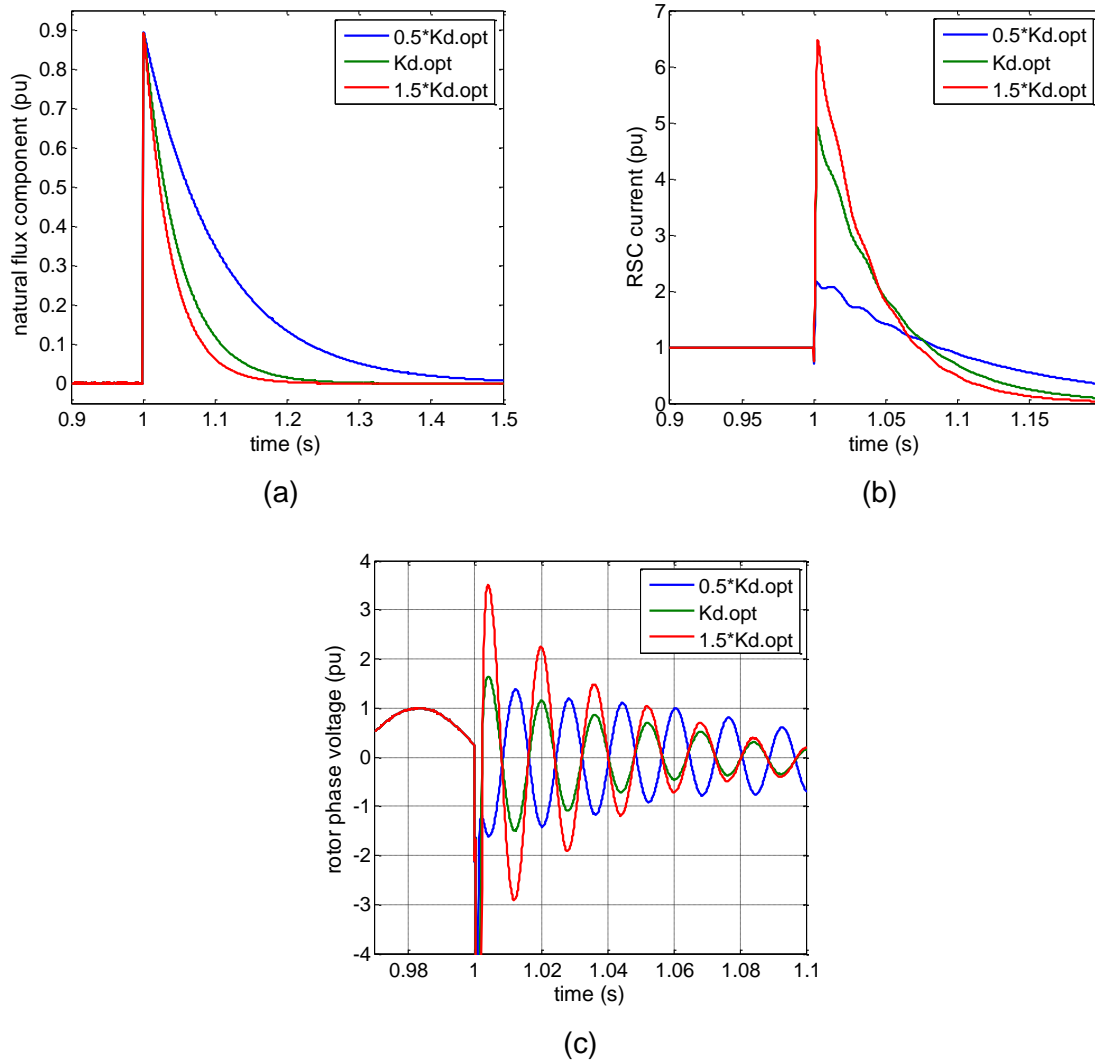
As seen in the last section, the use of the demagnetizing current strategy requires the injection of considerably high rotor currents, in order to reduce the effect of the natural flux on the rotor circuit. If the rotor current necessary to ensure the injection of reactive current is also taken into account, the total amount of rotor current would require the RSC to be significantly oversized. Since this is not such an attractive panorama, researchers have studied alternatives to enable the use of demagnetizing current strategy, even in case of very deep voltage dips.

##### 5.4.1. Crowbar & demagnetizing current injection (DC+CB)

In (LÓPEZ et al., 2009) is proposed the use of the demagnetizing current strategy together with the crowbar circuit system, in order to make viable a fast injection of reactive current using a standard RSC. The main drawback of the demagnetizing current strategy is that, during the first instants of the voltage dip, an

unbearably high rotor current is required to be injected. Therefore, this paper proposes the crowbar system activation during this first stage of the dip, protecting the converter from saturation while accelerating the decay of the stator natural flux component.

Figure 5.10 - 90% three-phase voltage dip for three values of  $K_d$ : (a) natural flux component, (b) RSC current, (c) rotor phase voltage.



When the natural flux reaches a value low enough to warrant that the required demagnetizing current is under the current limit of the converter, the RSC is reactivated and continues the demagnetization process while injecting reactive current.

A more detailed procedure is presented next:

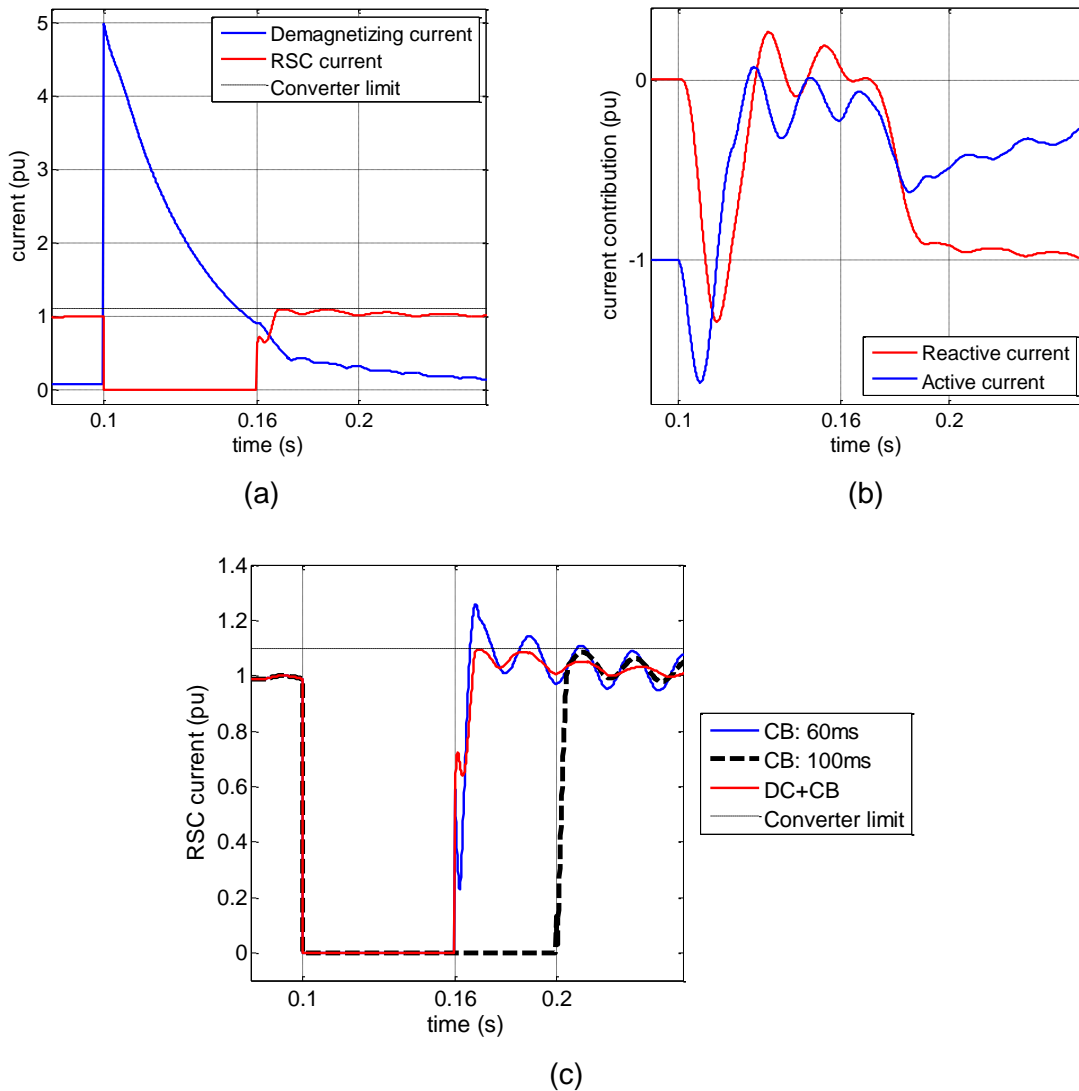
1. Immediately after the detection of the voltage dip, the crowbar system is activated. This accelerates considerably the decay of the stator natural flux component.
2. All along the crowbar activation period, the required demagnetizing current is calculated.
3. When the current calculated in point 2 reaches a value lower than the converter current limit, the crowbar is disconnected and the RSC is reactivated, acting according to the demagnetizing current strategy.
4. With the decrease of the stator natural flux component, the RSC is able to progressively inject reactive current, achieving the amount required by the gridcodes faster than any of the two basic strategies working isolated.

This procedure was applied to the 90% three phase voltage dip previously simulated and the results are presented in Figure 5.11. As can be seen in Figure 5.11a, after the beginning of the dip at  $t=0.1s$ , the crowbar system was activated and, as expected, the current circulating across the RSC is kept very close to zero. When the calculated demagnetizing current decays until the converter's current limit ( $t=0.18s$ ), the demagnetizing current strategy is activated, injecting through the rotor the sum of three currents:

- The current necessary to support the decay of the natural flux.
- An incremental amount of current that ensures the injection of reactive current through the stator.
- A detrimental amount of current that ensures the active current injection also through the stator.

This is possible due to the linearity of system that allows the superposition of these currents. In Figure 5.11b is presented the behavior of the stator's active and reactive currents, making evident the lack of control over these currents while the crowbar system is activated, and the considerable contribution of the demagnetizing current strategy during its activation period.

Figure 5.11 - DC+CB activation procedure in case of a 90% three-phase voltage dip: (a) currents of interest, (b) active and reactive current contributions, (c) RSC currents



Due to the gridcodes requirements for a voltage dip with this characteristics, 100ms after the beginning of the fault ( $t=0.2s$ ), the reactive current injected to the system through the stator must reach the nominal current capacity of the machine. Thus, after that time any protection strategy must be deactivated, allowing the RSC to recover control over the power transference between the machine and the system, without being on risk of saturation.

In Figure 5.11c can be seen that the combined use of the crowbar system and the demagnetizing current strategy effectively allows the diminution of the crowbar connection time, keeping the converter unsaturated while enjoying the already mentioned benefits of a fast crowbar deactivation. Even faster deactivations are

possible in systems with a higher natural flux decay constant, in which the criteria for the activation of the demagnetizing system are reached in a shorter time.

#### **5.4.2. Increase of the stator resistance & demagnetizing current injection (DC+I<sub>sr</sub>)**

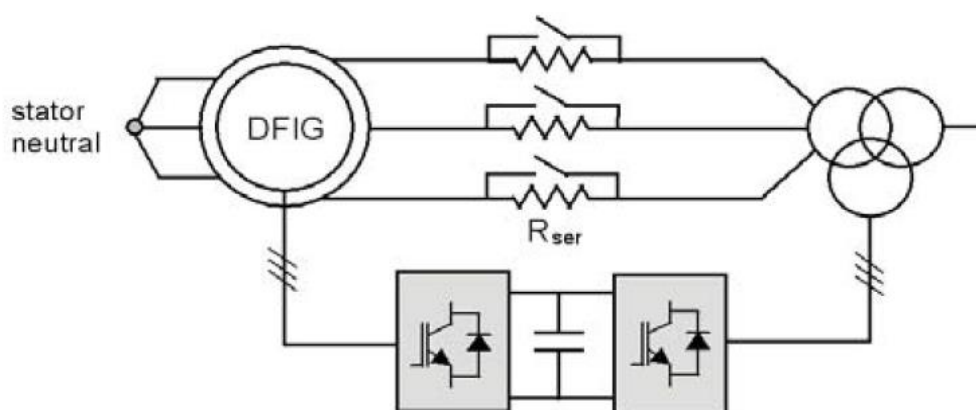
As can be seen in eq.(5.12), there is an inverse relationship between the stator resistance  $R_s$  and the time constant  $\tau_d$ . This means that an increase in the stator resistance value causes a reduction of the stator natural flux decay time. In (ESANDI et al., 2009) is proposed a procedure to use this fact in order to protect the RSC in the case of severe voltage dips. In order to increase the stator resistance value, it is suggested the introduction of resistances in series with each one of the stator phases, which, due to the power losses that a permanent connection would cause, are only connected for a short period of time after the detection of the voltage dip. In Figure 5.12 is presented a scheme of the system with the additional resistances and the bidirectional switches necessary for its connection and disconnection.

The protection strategy suggests the connection of the additional stator resistances, simultaneously with the injection of demagnetizing currents calculated in the same way that in the last section. The formal proposed procedure consists of the next steps:

1. Detection of the voltage dip.
2. Connection of the additional resistances for a short period of time (10ms approximately), while injecting the calculated demagnetizing currents.
3. Disconnection of the additional resistances and progressive diminution of the demagnetizing currents.

Applying this procedure to the same 90% voltage dip simulated previously, it is possible to confirm its effectiveness for the protection against deeper dips. The time that the additional resistances remained connected was arbitrarily chosen to be 10ms, in order to obtain results similar to those presented in (ESANDI et al., 2009).

Figure 5.12 - DC+Isr strategy layout



Source: (ESANDI et al., 2009)

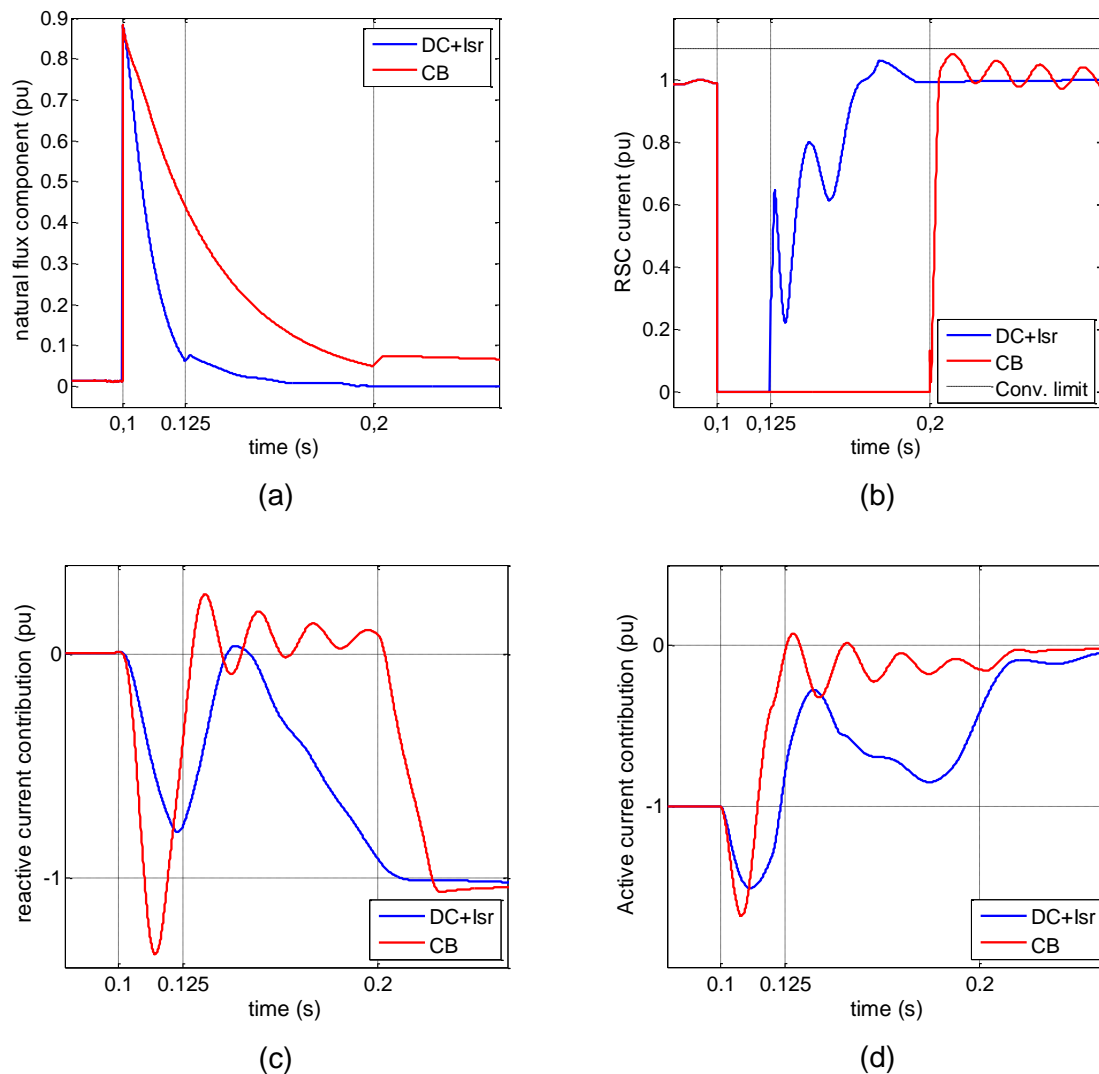
In Figure 5.13a is compared the behavior of the stator natural flux when using the crowbar circuit strategy and the increased stator resistance strategy treated in this section. It is evident the superior behavior of the last, considering that in only 10ms the natural flux was reduced 66%, something achieved by the crowbar strategy after 60ms.

In Figure 5.13b is presented the rotor current vector magnitude. The RSC current limit is never exceeded in the case of the increased stator resistance strategy, matching in this way the excellent behavior of the crowbar strategy with regards to the protection of the converter. This proves that the main safety requirement is fulfilled without requiring an oversized converter.

Additionally, as can be seen in Figure 5.13c, after the disconnection of the additional resistances, the increased stator resistance strategy achieves an increasing injection of reactive current through the stator, something far from possible when using the crowbar strategy.

Finally, in Figure 5.13d is presented the active stator current, evincing that the increased stator resistance strategy also allows the injection of a considerable amount of active current through the stator until the time that a full injection of reactive current is required by the grid codes ( $t=0.2s$ ).

Figure 5.13 - Behavior of the DC+Isr and CB strategies in case of a 90% three-phase voltage dip: (a) natural flux component, (b) RSC current, (c) reactive current contribution, (d) active current contribution.



Five protection strategies for the RSC were introduced along this chapter, explaining its operation, requirements and limitations in case of three-phase voltage dips. These strategies are:

- Crowbar circuit (CB)
- Feedback of the stator currents as the reference for the RSC (SCI)
- Demagnetizing current injection (DC)
- Crowbar & demagnetizing current injection (DC+CB)
- Increase of the stator resistance & demagnetizing current injection (DC+Isr)

In the next chapter, a more rigorous evaluation of their performance against voltage dips of different depth will be developed, assessing additionally the fulfillment of the European grid codes requirements related with the injection of reactive current during voltage dips.

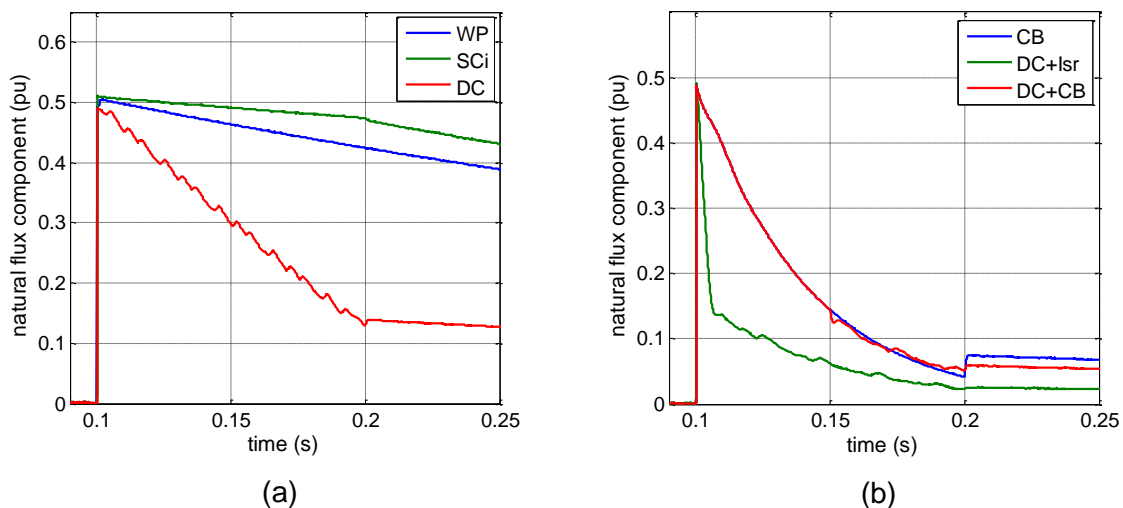
## 6. STRATEGIES COMPARISON

After introducing the protection strategies, it is now compared their response in case of balanced long duration voltage dips. For the simulation process, a 2MW machine with stator to rotor turn ratio  $u=0.24$  was selected, exposing it to an intermediate and a deep balanced voltage dips (50% and 90% respectively) at the stator terminals during 1.5s. The activation period of all the strategies was limited to 0.1s, in order to achieve the grid codes requirements summarized in (SOURKOUNIS; TOUROU, 2013). Looking for simplifying the analysis, the strategies were divided into two groups. The first group contains the strategies that do not require the introduction of additional hardware as well as the simulation of the system without any protection. The second group contains the strategies that require the introduction of additional hardware as the crowbar circuit and the additional stator resistances.

### 6.1. INTERMEDIATE BALANCED VOLTAGE DIP

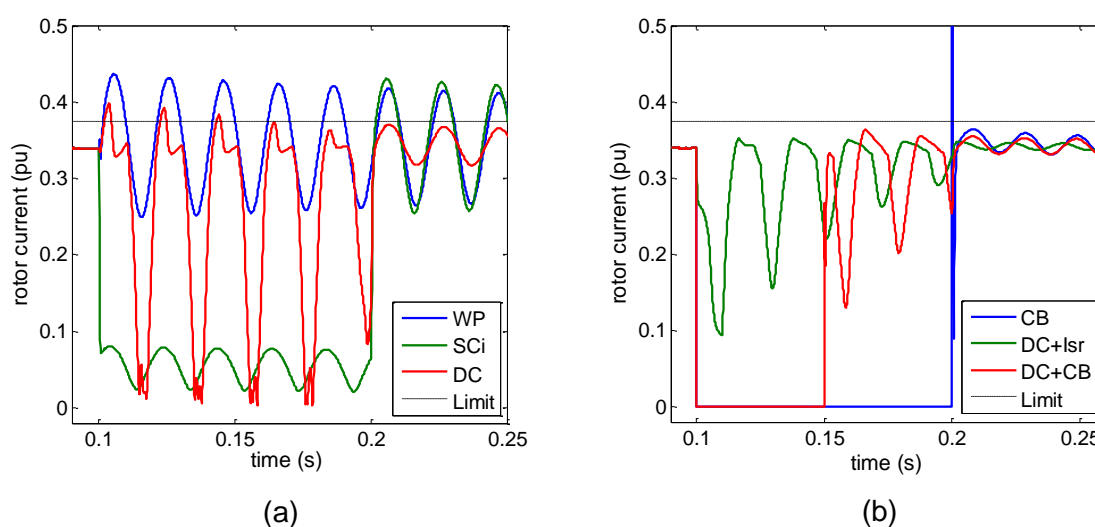
As was mentioned before, a 50% balanced voltage dip was first simulated at the stator terminals. In Figure 6.1 is presented the natural flux behavior for the six protection strategies.

Figure 6.1 - Stator natural flux behavior in case of a 50% three-phase voltage dip: (a) group 1 strategies (WP=No protection strategy; SCi =Feedback of the stator currents as a reference for the RSC; DC=Demagnetizing current injection), (b) group 2 strategies (CB=Crowbar circuit; DC+Isr=Increase of the stator resistance & demagnetizing current injection; DC+CB=Crowbar & demagnetizing current injection)



It is remarkable from Figure 6.1a that the stator current injection strategy (SCi) considerably reduces the natural flux decay rate during its activation, maintaining the natural flux practically unmodified until the strategy deactivation (only a 7% amplitude reduction by 0.2s). Consequently, an emf high enough to saturate the converter is induced in the rotor after  $t=0.2s$ , which takes the rotor current above the converter current limit as shown in Figure 6.2a. This demonstrates the inherent risk associated with using SCi for such a short period of time, even when in the same figures can be seen that between  $t=0.1s$  and  $t=0.2s$  the rotor current is kept far from the rotor maximum limit.

Figure 6.2 - Rotor current behavior in case of a 50% three-phase voltage dip:  
 (a) group 1 strategies (WP=No protection strategy; SCi =Feedback of the stator currents as a reference for the RSC; DC=Demagnetizing current injection), (b) group 2 strategies (CB=Crowbar circuit; DC+Isr=Increase of the stator resistance & demagnetizing current injection; DC+CB=Crowbar & demagnetizing current injection)



When no protection strategy is used (WP), again due to the high natural flux value (Figure 6.1a), the converter is continuously saturated and the maximum current limit is exceeded periodically as seen in Figure 6.2a. This confirms the necessity of using protection strategies in case of voltage dips, even for the swallow ones as the one simulated in this section.

In the case of the demagnetizing current strategy (DC), by the time that the strategy is deactivated ( $t=0.2s$ ), the natural flux amplitude has been reduced to 25% of its initial value. This reflects on the rotor current amplitude after the deactivation, which

exceeds the current limit for a very reduced amount of time at the beginning of the dip as seen in Figure 6.2a.

The behavior of the strategies that belong to the second group will be analyzed next. The vastly recognized crowbar circuit strategy (CB) makes part of this group. From Figure 6.1b can be seen that a very fast decay of the stator natural flux is achieved using this strategy, reaching a flux magnitude 90% smaller than the peak value, by the end of the activation period. This certainly has an influence on the rotor current magnitude, that, once more, is kept under the established converter limit all the time (see Figure 6.2b).

As presented in the last chapter, one of the variations of the demagnetizing current strategy includes the crowbar system in its operation. This strategy, presented in the figures as (DC+CB), requires the connection of the crowbar circuit at the beginning of the dip, keeping it active until the time when the desired demagnetizing current (that depends on the natural flux) has reached a value lower than the converter current limit. For this particular simulation, it was found that the crowbar circuit must be connected for 50ms. In Figure 6.1b and Figure 6.2b can be evinced this agreement, which also confirms the protection of the converter until that point. After the disconnection of the crowbar circuit ( $t=0.15s$ ), the demagnetizing current strategy is activated. Due to the reduced value of the natural flux at this point, the strategy maintains the rotor current under the limit, allowing also the injection of some reactive current through the stator during this period, as will be shown ahead. The last of the strategies studied is the introduction of additional stator resistances simultaneously with the demagnetizing current strategy. As in the case of DC+CB, the time that the resistances have to be connected is conditioned to the reduction of the desired demagnetizing current until a value under the maximum limit of the converter.

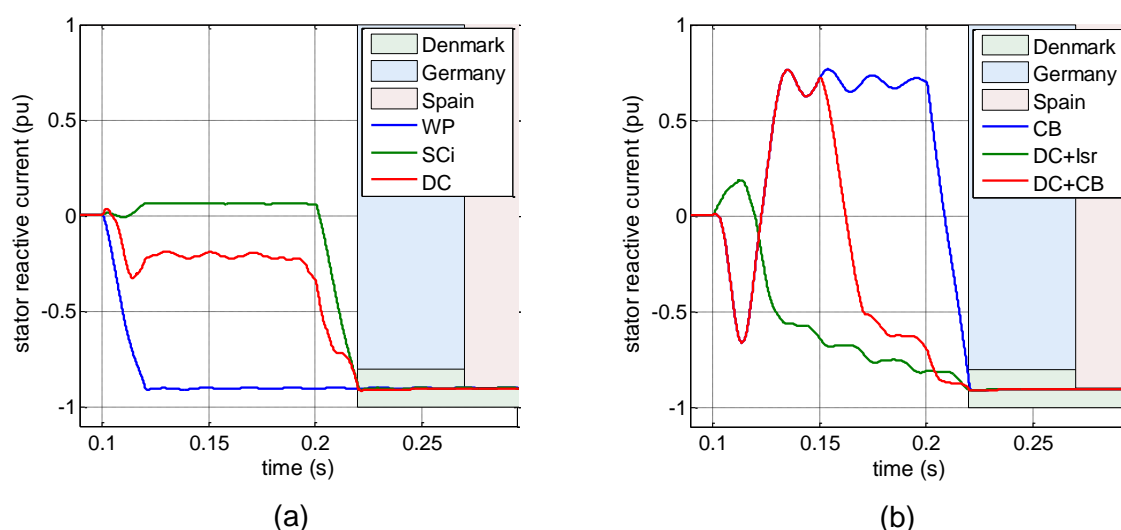
For this particular case that time was found to be 10ms, after which only the demagnetizing current strategy remains activated. In Figure 6.1b can be seen the extremely fast reduction of the natural flux component, caused by the connection of the stator resistances, reaching 27% of its maximum amplitude by the end of the 10ms ( $t=0.11s$ ). This same effect was attained by DC+CB only after 50ms of the connection, which demonstrates the great advantage in terms of speed that the introduction of the external resistors represents. With regards to the rotor current, is easy to notice in Figure 6.1b that this strategy always maintains its amplitude under

the converter limit, having as an additional advantage the fast activation of the magnetizing current strategy that, as will be shown below, allows the early injection of reactive current through the stator.

### 6.1.1. Grid-codes compliance

It is now time to assess the compliance of the simulated strategies with the grid codes. The requirements related with the injection of reactive current, for three different grid codes, are graphically presented in Figure 6.3a and Figure 6.3b. An easy to apply criterion for assessing if a strategy satisfies the requirements of a specific grid code, is that the line that represents the amount of reactive current injected to the grid cannot cross the filled area that represent the grid code.

Figure 6.3 - Stator reactive current contribution in case of a 50% three-phase voltage dip: (a) group 1 strategies (WP=No protection strategy; SCi =Feedback of the stator currents as a reference for the RSC; DC=Demagnetizing current injection), (b) group 2 strategies (CB=Crowbar circuit; DC+Isr=Increase of the stator resistance & demagnetizing current injection; DC+CB=Crowbar & demagnetizing current injection)



From Figure 6.3a is possible to see that all the strategies belonging to the first group (the ones that do not require the use of additional hardware) meet the requirements of the German and Spanish gridcodes, assuming that the rotor overcurrent associated with its use is beard by the converter. However, the more strict requirements of the Danish gridcode are not complied by any of the strategies. This can be justified by the negative correlation between the stator reactive current and the stator flux, which occurs when the rotor reference frame and the stator flux are

aligned, as demanded by the vector control theory. In order to clarify this, eq.(6.1) and eq.(6.2) present the stator current  $dq$  components in terms of the rotor current  $dq$  components, considering an alignment between the reference frame and the stator flux:

$$i_{qs} = -\frac{L_m}{L_s} i_{qr} \quad (6.1)$$

$$i_{ds} = \frac{\psi_s}{L_s} - \frac{L_m}{L_s} i_{dr} \quad (6.2)$$

Remembering that in steady state the stator flux  $\psi_s$  is proportional to the grid voltage  $V_s$ , and neglecting the small voltage drop in the stator resistance we have:

$$V_s \approx \omega_s \psi_s \quad (6.3)$$

Replacing eq.(6.3) into eq.(6.2) it is obtained:

$$i_{ds} = \frac{V_s}{\omega_s L_s} - \frac{L_m}{L_s} i_{dr} \quad (6.4)$$

When comparing eq.(6.4) and eq.(6.1), it is possible to notice that, in the case of a partial voltage dip ( $V_s > 0$ ), the amount of direct rotor current  $i_{dr}$  necessary to inject 1pu of reactive stator current  $i_{ds}$  is greater than the amount of quadrature rotor current  $i_{qr}$  necessary to inject 1pu of active stator current  $i_{qs}$ . Thus, the current that must circulate across the rotor, in order to meet the requirements of the Danish gridcode, exceeds the converter's nominal current value. This, added to the effect of the emf induced by the stator natural flux, would inevitably increment the rotor current, taking it to a value unbearable for most of the strategies. For this reason, the compliance with this demanding grid code would require the increment of the converter current capacity and the modification of the RSC control loop in order to take this phenomenon into account.

It is also remarkable from Figure 6.3a, the injection of reactive current caused by the action of the demagnetizing current strategy (DC) during its duty period. This represents 22% of the maximum reactive current that the generator is able to inject. On the other hand, the stator current injection strategy (SCi) not only did not contribute to the recovery of the system through the injection of reactive current, but it also extracted reactive current from the grid. This is a highly undesirable condition; however, it is a common behavior for several strategies, as will be seen ahead.

The behavior of the stator reactive current for the strategies that require the introduction of external hardware is presented in Figure 6.3b. Again, all of them comply with the requirements of the English and Spanish grid codes, and, for the

same reasons that the strategies belonging to the first group, none of them comply with the requirements of the Danish grid code.

During its activation period, the crowbar circuit strategy (CB) makes the generator behave as a squirrel cage induction motor with a high rotor resistance. This causes the circulation of a very high inductive current across the stator, reaching approximately 70% of the nominal stator current for this particular case. As mentioned before, this behavior is highly injurious for a power system attempting to recover its nominal voltage.

Since the DC+CB strategy is based on the connection of the crowbar system for a short period of time, during that period of time there is a high circulation of inductive current across the stator (see Figure 6.3b). Simultaneously with the crowbar disconnection, the demagnetizing current strategy is activated at  $t=150\text{ms}$ . This allows a fast variation of the stator current direction, which goes from inductive to capacitive in only 10ms. In this way, after only 60ms of the dip start, the machine gets to contribute to the recovery of the system voltage. After a short period of moderate inductive current circulation, the DC+Isr strategy forces the circulation of a high value capacitive current, during 90% of its activation period. This confirms the outstanding performance of this strategy protecting the machine while excelling in the contribution to the system recovery.

### **6.1.2. Active power behavior**

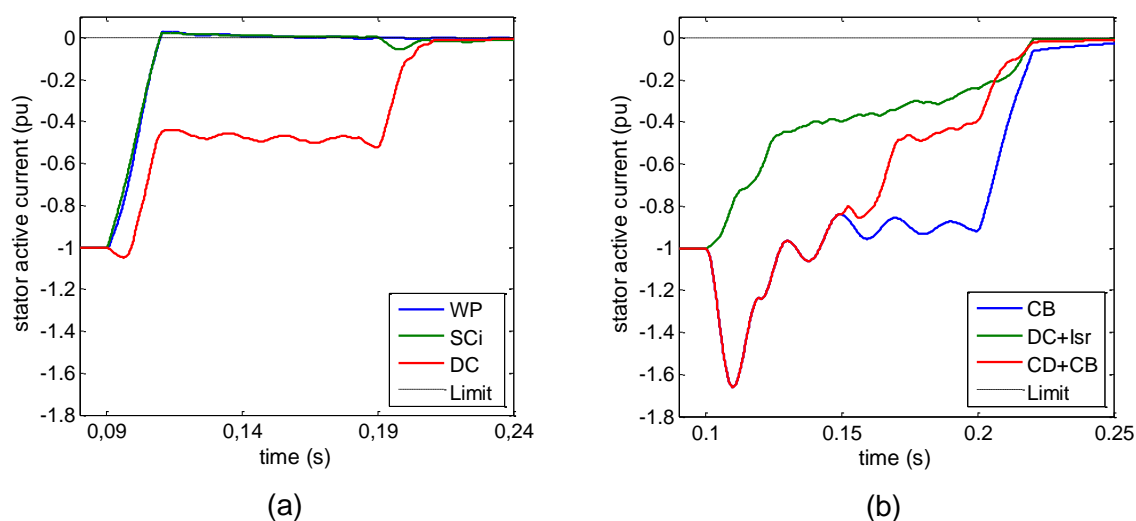
During a voltage dip, the studied European grid codes are only concerned about the stator reactive current behavior. Thus, the behavior of the stator active current is not commonly addressed by the technical literature. In Figure 6.4a is presented the behavior of this variable for the first group of strategies. It is possible to see that neither WP nor SCi strategies inject active current to the grid during the voltage dip, because of to the rigid definition of their rotor references.

On the other hand, due to the action of the already described references priority system, the DC strategy allows to choose the proportion between active and reactive current to be injected, having as a maximum limit the difference between the rotor maximum current and the demagnetizing current. For this simulation, it was decided to inject more active current than reactive current in order to prove the

flexibility that this strategy allows. The behavior of the active current for the second group of strategies is presented in Figure 6.4b.

Considering that during the crowbar activation period it is not possible to control the currents circulating across the rotor, the stator active current in this period will be determined exclusively by the electro mechanical interactions of the machine. It can be seen in Figure 6.4b that, after a short transitory, the two strategies that involve the connection of the crowbar circuit (CB and DC+CB) inject approximately 1pu of active current while the crowbar is activated. After the disconnection the crowbar, the CD+CB strategy slowly takes the active current to zero at the same time that the reactive current raises to the maximum value as was seen in Figure 6.3b.

Figure 6.4 - Stator active current contribution in case of a 50% three-phase voltage dip: (a) group 1 strategies (WP=No protection strategy; SCi =Feedback of the stator currents as a reference for the RSC; DC=Demagnetizing current injection), (b) group 2 strategies (CB=Crowbar circuit; DC+Isr=Increase of the stator resistance & demagnetizing current injection; DC+CB=Crowbar & demagnetizing current injection)

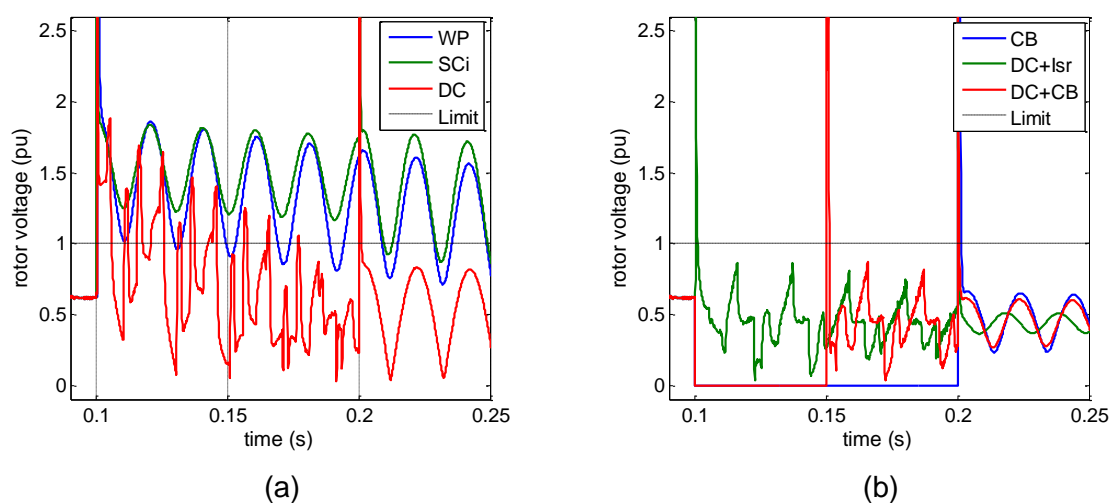


When the strategy DC+Isr is applied, the stator active current has a behavior very similar to the one obtained due to the application of DC strategy. This was expected to happen considering that the only difference between these two strategies is the short introduction of the additional stator resistances at the beginning of the dip. Since the connection of these resistances considerably accelerate the natural flux decay, the amount of demagnetizing current that has to circulate across the rotor for DS+Isr strategy is less than for DC strategy, allowing a greater injection of active or reactive current through the stator when using the former one.

### 6.1.3. Rotor voltage behavior

One thing to be noticed about the discussion is that, up to this point, no mention has been made about the rotor voltage required for the implementation of the strategies. In order to let the strategies show their potential, no limit was imposed to the rotor voltage for the simulations presented until now. This was achieved by implementing an over dimensioned converter, with a maximum output voltage of 6 times the rated stator voltage (base voltage). However, since this last is not an economically attractive solution, it is necessary to evaluate the behavior of the converter output voltage for the six strategies. In Figure 6.5 is presented the voltage imposed by the converter for each one of them.

Figure 6.5 - Rotor voltage behavior in case of a 50% three-phase voltage dip:  
 (a) group 1 strategies (WP=No protection strategy; SCi =Feedback of the stator currents as a reference for the RSC; DC=Demagnetizing current injection), (b) group 2 strategies (CB=Crowbar circuit; DC+Isr=Increase of the stator resistance & demagnetizing current injection; DC+CB=Crowbar & demagnetizing current injection)



When no protection is used (see WP in Figure 6.5a), the converter has to be able to generate a maximum voltage of 1.8 times the rated stator voltage. This is unachievable for most of the converters available in the market (ABB, 2013)(VACON, 2014), usually dimensioned to generate a maximum voltage equal to the rated stator voltage (1pu). Strategies SCi and DC also demand a value of rotor voltage close to 1.8pu, as can be seen in Figure 6.5a.

Ignoring the high voltage peaks caused by the fast variation of the references values, it can be seen in Figure 6.5b that none of the strategies belonging to the second group demand a voltage higher than the rated stator value. Due to this fact, these strategies can be implemented making use of commercial power converters,

without exceeding the predefined current limit of the RSC. This last will be evinced next.

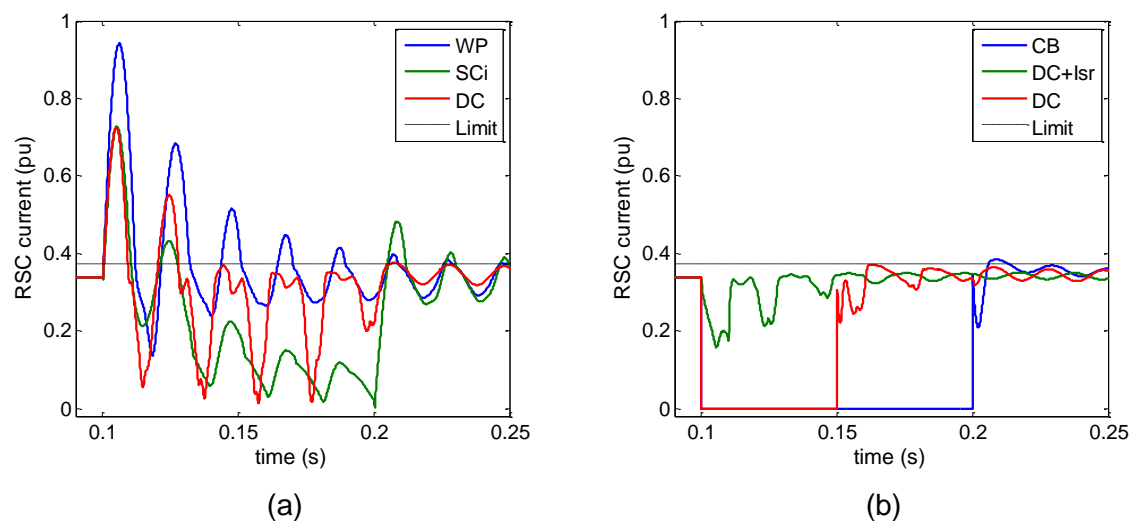
#### **6.1.4. Influence of using standard ratings for the converter**

To assess the consequences of applying the studied strategies, when using a converter with standard ratings, the converter Vacon 8000 Wind (VACON, 2014) was selected as a reference, adopting its maximum voltage and current values (1pu and 0.34pu respectively) as the converter limits for the subsequent simulations. So as to make a fair comparison, the previously studied 50% 3 phase voltage dip was simulated for the six strategies. In Figure 6.6 and Figure 6.7 are presented the rotor current and the reactive stator current respectively, both necessary to evaluate the accomplishment of the two protection strategies goals: to maintain the rotor current under the converter maximum limit and to fulfill the gridcodes requirements.

It can be seen in Figure 6.6a that all the strategies belonging to group 1 significantly exceed the current limit defined as 110% of the nominal current. This behavior was easy to predict after analyzing Figure 6.2a and Figure 6.5a, which show that not even for an almost unlimited converter voltage these strategies get to maintain the rotor current under the limit, let alone for a considerably smaller converter rated voltage. As was shown in Figure 6.5b, none of the strategies belonging to group 2 demand a converter voltage superior to the Vacon 8000's limit (1pu). Thus, it is possible for all of them to maintain the rotor current under the limit, during and after the operation of the strategies (see Figure 6.6b).

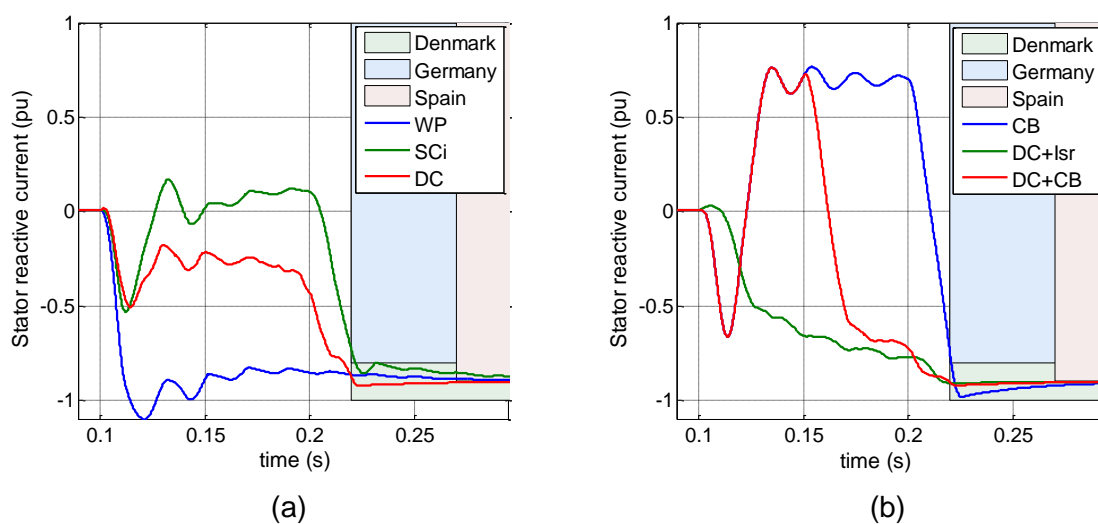
The fulfillment of the gridcodes requirements, with regards to the reactive current injection, can be evaluated in Figure 6.7. As can be seen in Figure 6.7a, strategies belonging to group 1 get to supply the current demanded by the English grid code, assuming of course that the converter bears the high current represented in Figure 6.6a. However, they are not able to satisfy the requirements of the Spanish and Danish grid codes. In turn, strategies belonging to group 2 satisfy the requirements of both the German and Spanish gridcodes, as shown in Figure 6.7b. This was expected to happen since the restriction on the maximum converter voltage do not affect significantly the performance of these strategies (see Figure 6.5b).

Figure 6.6 - RSC current behavior in case of a 50% three-phase voltage dip using a standard rated converter: (a) group 1 strategies (WP=No protection strategy; SCi =Feedback of the stator currents as a reference for the RSC; DC=Demagnetizing current injection), (b) group 2 strategies (CB=Crowbar circuit; DC+Isr=Increase of the stator resistance & demagnetizing current injection; DC+CB=Crowbar & demagnetizing current injection)



According with the results obtained until this point, it is possible to conclude that for a balanced voltage dip of an intermediate depth, as the one simulated before, the strategies belonging to group 2 excel in their duties of protection of the RSC and contribution to the voltage grid recovery.

Figure 6.7 - Stator reactive current contribution in case of a 50% three-phase voltage dip, using a standard rated converter: (a) group 1 strategies (WP=No protection strategy; SCi =Feedback of the stator currents as a reference for the RSC; DC=Demagnetizing current injection), (b) group 2 strategies (CB=Crowbar circuit; DC+Isr=Increase of the stator resistance & demagnetizing current injection; DC+CB=Crowbar & demagnetizing current injection)



## 6.2. DEEP BALANCED VOLTAGE DIP

It is well known at this stage the dependence between the stator natural flux amplitude and the voltage dip depth. Since the magnitude of the emf induced in the rotor is directly related to the natural flux amplitude, it is necessary to evaluate the performance of the strategies that proved its effectiveness for the 50% voltage dip, which are the ones that belong to the group 2. In order to do this, a 90% 3 phase voltage dip was simulated. In Figure 6.8 is presented the behavior of the stator natural flux for the strategies of group 2. It can be noted that the three strategies achieve a fast reduction of the natural flux magnitude (90% in 100ms), even when in this case it reaches 0.9pu, almost 2 times the magnitude evinced for the 50% voltage dip (see Figure 6.3). It is worth to remember that this reduction of the natural flux is indispensable to avoid the saturation of the converter, after the deactivation of the protection strategies.

In Figure 6.9 is presented the current circulating across the RSC. It is evident that the three strategies maintain the current value under the converter limit. This confirms that, with disregard of the dip's depth, the strategies belonging to group 2 protect the converter during its activation period and, by the time of their disconnection, provide the conditions for a safe alignment of the converter's behavior with the demands made by the gridcodes.

Figure 6.8 - - Stator natural flux behavior in case of a 90% three-phase voltage dip, using a standard rated converter (CB=Crowbar circuit; DC+Isr=Increase of the stator resistance & demagnetizing current injection; DC+CB=Crowbar & demagnetizing current injection)

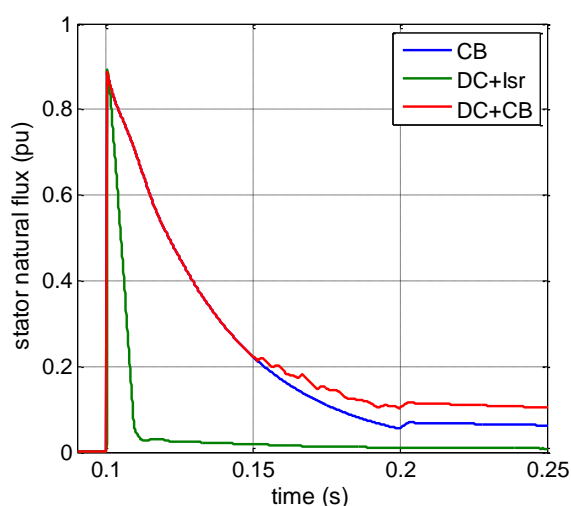
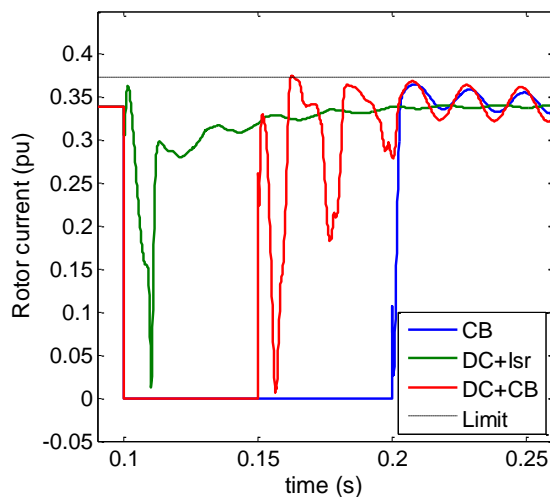
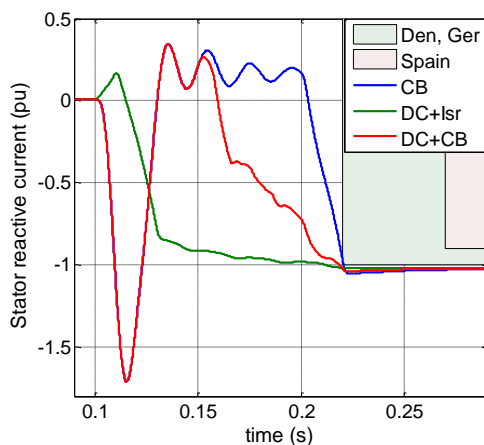


Figure 6.9 - Rotor current behavior in case of a 90% three-phase voltage dip, using a standard rated converter (CB=Crowbar circuit; DC+Isr=Increase of the stator resistance & demagnetizing current injection; DC+CB=Crowbar & demagnetizing current injection)



With regard to these demands, It is possible to see in Figure 6.10 that all three strategies meet the requirements of the evaluated grid codes. Contrary to what could be though, the most commonly used strategy (CB) is the one that encounters the greatest difficulties to comply the 1pu reactive current injection demand. On the other hand, strategy DC+Isr allows a soft transition of the injected reactive current by the time of its deactivation. This is justified by the action of the reference priority system which, as mentioned before, controls the progressive injection of reactive current almost from the beginning of the dip.

Figure 6.10 - Stator reactive current contribution in case of a 90% three-phase voltage dip, using a standard rated converter (CB=Crowbar circuit; DC+Isr=Increase of the stator resistance & demagnetizing current injection; DC+CB=Crowbar & demagnetizing current injection)



The simulation results presented along this chapter allow us to draw some important conclusions about the performance of the protections strategies. First of all, it is evident the necessity of introducing external hardware in order to fully protect the machine in case of three-phase voltage dips, when using standard sized converters. The performance of these external devices can be significantly improved if the demagnetizing current strategy is jointly used, as was done in the case of the DC+CB and DC+Isr strategies. With regard to the grid codes requirements compliance, it can be seen that the three techniques involving the addition of external hardware fulfill the requirements of the Spanish and English grid codes for any voltage dip depth. However, the Danish grid code requirements are not fully satisfied by any protection strategy, requiring the use of an oversized converter in order to counteract the effects of partial voltage dips.

## 7. CONCLUSIONS AND FURTHER WORK

The performance comparison of the five studied protection strategies delivered a clear panorama of the restrictions for the use of each one of them, while aiming to comply with the grid-codes requirements. It is important to highlight that the division made in the last chapter between the strategies that require additional hardware (*CB*, *DC+Isr* and *DC+CB*), named group 2, and the ones that are based only in the control of the RSC (DC and SCI), named group 1, also drafted a marked division in effectiveness and costs. For both the simulated dip depths (50% and 90%), the strategies belonging to group 2 excelled in the protection of the converter, maintaining the current circulating trough it under the predefined limit all the time.

By contrast, the strategies belonging to group 1 were not even able to control the RSC current that appears in case of a 50% dip, requiring the introduction of an oversized converter capable of generating a voltage several times greater than the stator nominal voltage, a non-attractive alternative in terms of costs and size of the generator.

These facts lead us to conclude that it is not possible to completely warrant the safety of the RSC only trough the control of the converter, being imperative the introduction of external support hardware as the crowbar circuit or the additional stator resistances.

With regards to the compliance of the grid-codes requirements, all the strategies belonging to group 2 achieved the demanded current injection for the 90% voltage dip. However, when the voltage dip is swallower than that, the demanding requirements of the Danish grid-code force the converter to inject a current slightly greater than the nominal current, in order to overcome the effects of the remaining stator flux as explained in chapter 6.

Since all the group 2 strategies effectively protect the converter and comply with the requirements of the grid-codes, the selection of one of them is influenced by aspects like the time required for the reconnection of the converter and the simplicity of its implementation. In order to contribute to this affair, from the results of this research project is possible to indicate the advantages that each strategy offers in terms of the required activation time and injection of active and reactive current before the time limit established by the grid-codes.

The solely use of the traditional Crowbar circuit strategy requires the longest activation period among the group 2 strategies, needing in the most demanding scenario to be activated during the maximum time allowed by the grid-codes. Regarding the injection of active and reactive current, it is impossible to control these two variables during its activation period, what opens the way to scenarios of active and reactive power consumption during the first instants of the voltage dip.

The joint work of the Crowbar circuit and the demagnetizing current strategy (DC+CB) allows a considerable reduction of the Crowbar activation time, returning the control over the rotor currents to the RSC control system in approximately half the maximum time allowed by the grid-codes. Been able to control the rotor currents, the injection of reactive current is progressively increased while the natural flux decreases due to the injection of demagnetizing current.

Finally, the short connection of an external set of stator resistances while injecting the calculated demagnetizing current (DC+I<sub>sr</sub>) allows the fastest injection of reactive current after the dip start (up to 1/10 of the crowbar connection time). Thus, the contribution to the recovery of the system voltage far surpasses the grid-codes requirements, presenting this system as a high performance alternative when the voltage stability is a matter of concern.

As a last consideration, it is important highlight the excellent performance of the implemented DFIG model, allowing fast precise simulations of transient electromagnetic phenomena in the grid. Due to its open structure, this model allows further improvements as well as its connection with complex electrical systems.

## 7.1 FURTHER WORK

Based on the generator electromagnetic model presented in this document, a complete electromechanic model of the wind turbine can be developed by adding the turbine and incidental wind mechanic models. This complete model would allow us to study not only the behavior of the machine during the first instants of the dip, but also the electromechanic interactions caused by the reduced active power transference during the whole dip.

Additionally, due to the already mentioned flexibility of the developed model, its connection with large electric systems would allow the development of stability

studies considering the real behavior of the DFIG during disturbances in the grid, without requiring excessive computation time.

Finally, it is important to highlight the potential that the developed model has as a teaching aid for electric machines undergraduate courses, allowing a friendly approach to the structure and operation modes of the generator, theoretically introduced in these courses.

## BIBLIOGRAPHY

ABAD, G. et al. **Doubly Fed Induction Machine: Modeling and Control for Wind Energy Generation**. [s.l.] John Wiley & Sons, 2011. p. 704

ABB. ABB low voltage wind turbine converters Brochure. p. 6–9, 2013.

ANIRUDH, A. .; VINOD, J. Design of output dv/dt filter for motor drives. **2010 5th International Conference on Industrial and Information Systems**, p. 562–567, jul. 2010.

BLAABJERG, F.; CHEN, Z. **Power Electronics for Modern Wind Turbines**. [s.l.] Morgan&Claypool, 2006.

BOLDEA, I. **Variable Speed Generators**. [s.l.] Taylor & Francis Group, 2005. p. 552

CHALMERS, B. J.; MUSABA, L.; GOSDEN, D. F. Variable-frequency Synchronous Motor Drives for Electric Vehicles. 1996.

CHAPMAN, S. **Electric Machinery Fundamentals**. 4th. ed. [s.l.] McGraw-Hill, 2005.

CHEN, H. L. Z. Overview of different wind generator systems and their comparisons. n. August 2007, p. 123–138, 2008.

ESANDI, I. et al. Alternative Protection System for Wind Turbines with Doubly Fed Induction Generator. p. 501–506, 2009.

FRAILE MORA, J. **Máquinas Eléctricas**. [s.l.] McGraw-Hill, 2006.

GAUTAM, D. et al. Impact of Increased Penetration of DFIG-Based Wind Turbine Generators on Transient and Small Signal Stability of Power Systems. v. 24, n. 3, p. 1426–1434, 2009.

GLOBALDATA. **Global Cumulative Wind Power Capacity to More than Double by 2020, Led by China**. Disponível em: <<http://energy.globaldata.com/media-center/press-releases/power-and-resources/global-cumulative-wind-power-capacity-to-more-than-double-by-2020-led-by-china-says-globaldata>>. Acesso em: 16 jun. 2014.

LIMA, F. K. A. et al. Rotor Voltage Dynamics in the Doubly Fed Induction Generator During Grid Faults. v. 25, n. 1, p. 118–130, 2010.

LÓPEZ, J. et al. Control of Doubly Fed Induction Generator under Symmetrical Voltage dips. n. 1, p. 2456–2462, 2008.

LÓPEZ, J. et al. Ride Through of Wind Turbines With Doubly Fed Induction Generator Under Symmetrical Voltage Dips. v. 56, n. 10, p. 4246–4254, 2009.

MINISTÉRIO DE MINAS E ENERGIA; EMPRESA DE PESQUISA ENERGÉTICA. Plano Decenal de Expansão de Energia 2020. 2011.

NASAR, S. A.; BOLDEA, I. **Electric machines: dynamics and control**. [s.l: s.n.].

ONG, C.-M. **Dynamic Simulation of Electric Machinery: Using Matlab/Simulink**. [s.l.] Prentice Hall PTR, 1998. p. 626

QUANG, N.; DITTRICH, J. **Vector control of three-phase AC machines**. [s.l: s.n.].

SCHULZ, M. A. X. W.; CLARKE, E. Determination of Instantaneous Currents and Voltages by Means of Alpha , Beta , and Zero Components. 1951.

SOURKOUNIS, C.; TOUROU, P. Grid Code Requirements for Wind Power Integration in Europe. v. 2013, 2013.

STOJAN, D.; MILANOVIC, M. Over-modulation phenomena and its influence on the pulse width modulated single-phase inverter output voltage. v. 51, n. 2, p. 174–180, 2010.

VACON. **Vacon AC Drives and Power Converters Brochure**, 2014.

VASCA, F.; IANNELLI, L. **Dynamics and Control of Switched Electronic Systems**. London: Springer London, 2012.

XIANG, D. et al. Control of a Doubly Fed Induction Generator in a Wind Turbine During Grid Fault Ride-Through. v. 21, n. 3, p. 652–662, 2006.

## APENDIX A - 2MW DFIG technical data

Table A.1 - Generator Characteristics

Characteristic	Value	Features
Synchronism	1500 rev/min	Synchronous speed at 50Hz
Rated power	2 MW	Nominal stator three-phase active power
Rated stator voltage	690 $V_{rms}$	Line-to-line nominal stator voltage
Rated stator current	1760 $A_{rms}$	Nominal stator current
Rated torque	12.7 kNm	Nominal torque
Stator connection	Star	
$p$	2	Pair of poles
Rated rotor voltage	2070 $V_{rms}$	Line-to-line nominal rotor voltage
Rotor connection	Star	
$u$	0.34	Stator to rotor turn ratio
$R_s$	2.6 $m\Omega$	Stator resistance
$L_{\sigma s}$	87 $\mu H$	Stator leakage inductance
$L_m$	2.5 $mH$	Magnetizing inductance
$R_r$	2.9 $m\Omega$	Rotor resistance referred to the stator
$L_{\sigma r}$	87 $\mu H$	Rotor leakage inductance referred to the stator
$L_s$	2.587 $mH$	Stator inductance $L_s = L_m + L_{\sigma s}$
$L_r$	2.587 $mH$	Rotor inductance $L_r = L_m + L_{\sigma r}$

## APENDIX B - Publications

CORTES, D. J. F. ; NARANJO, R. R. A. ; SALLES, M. B. C. . Voltage sags and short circuit analysis in power systems with high wind power penetration based on doubly fed induction generator. In: 2013 IEEE PES Conference on Innovative Smart Grid Technologies (ISGT Latin America), 2013, São Paulo. 2013 IEEE PES Conference on Innovative Smart Grid Technologies (ISGT Latin America), 2013.

CORTES, D. J. F. ; NARANJO, R. R. A. ; SALLES, M. B. C. . Analysis of Transmission Systems with High Penetration of Wind Power using DFIG based Wind Farms during Voltage Sags. In: International Conference on. CLEAN ELECTRICAL POWER Renewable Energy Resources Impact (ICCEP 2013), 2013, Alghero. anais, 2013.